Early stages of clustered star formation -massive dark clouds throughout the Galaxy-

Frieswijk, Willem Freerk

RIJKSUNIVERSITEIT GRONINGEN

Early stages of clustered star formation

– massive dark clouds throughout the Galaxy –

Proefschrift

ter verkrijging van het doctoraat in de
Wiskunde en Natuurwetenschappen
aan de Rijksuniversiteit Groningen
op gezag van de
Rector Magnificus, dr. F. Zwarts,
in het openbaar te verdedigen op
vrijdag 28 maart 2008
om 14.45 uur

door

Willem Freerk Frieswijk

geboren op 3 april 1976
te Weststellingwerf

Promotor:	Prof. dr. M. C. Spaans
Copromotor:	Dr. R.F. Shipman

Beoordelingscommissie:	Prof. dr. W. Wild
	Prof. dr. J. M. van der Hulst
	Prof. dr. C. Dominik

ISBN: 978-90-9022875-4

I have great faith in fools;
Self-confidence my friends call it

Edgar Allen Poe

Ik heb een steen verlegd in een rivier op aarde
Nu weet ik dat ik nooit zal zijn vergeten
Ik leverde bewijs van mijn bestaan
Omdat door het verleggen van die ene steen
De stroom nooit meer dezelfde weg zal gaan

Bram Vermeulen

Front cover – *Acrylic painting on canvas of the Carbon monoxide emission toward Outer Galaxy Dark Cloud G111.80+0.58*, by Sanne Frieswijk-van Eeden.

Back cover – *Spitzer near-infrared view of the Outer Galaxy Dark Cloud G111.80+0.58 in the shape of the the Big Island of Hawai'i*

I ka nānā no a 'ike (Hawaiian saying) — *By observing, one learns*

The studies presented in this thesis were performed at the Kapteyn Astronomical Institute, department of the Faculty of Mathematics and Natural Sciences, University of Groningen, the Netherlands.

Financial support by the Netherlands Institute for Space Research (SRON), and travel support by the Leids Kerkhoven-Bosscha Fonds are gratefully acknowledged. This work has benefited from research funding from the European Community's Sixth Framework Programme.

Printed by PrintPartners Ipskamp B.V., Enschede, the Netherlands.

Contents

Chapter 1

Introduction

AT NIGHT, away from the nocturnal glow of urbanised areas, a diffuse band of light emerging from a myriad of stars can be discerned, reaching from horizon to horizon. These stars constitute the stellar disk of our Galaxy, the Milky Way. The space between these stars is vast, but it is far from empty. Everything in between the stars is called the Interstellar Medium (ISM). A tenuous gas, filling most of interstellar space, is structured in distinct phases. Three main phases exist in approximate pressure (P) equilibrium with each other, i.e., the product of the density (n) and temperature (T) in each phase is constant ($P \sim nT \approx 10^4\,\mathrm{cm}^{-3}\,\mathrm{K}$). These are the hot coronal and intercloud gas ($n < 10^{-2}\,\mathrm{cm}^{-3}$, $T \sim 10^6\,\mathrm{K}$); the warm, neutral and ionised gas ($n \sim 0.1$–$10\,\mathrm{cm}^{-3}$, $T \sim 10^3$–$10^4\,\mathrm{K}$); and the cool atomic gas ($n \sim 100\,\mathrm{cm}^{-3}$, $T \sim 100\,\mathrm{K}$). An additional hot, ionised gas phase ($n \sim 1$–$10^5\,\mathrm{cm}^{-3}$, $T \sim 10^4\,\mathrm{K}$) is present in the form of discrete nebulae called HII regions. In both mass and volume, they occupy a negligible fraction ($\leq$1%) of the ISM, but they are very prominently visible throughout the Galaxy. In contrast to the previous phases, HII regions are not in equilibrium but continuously fed by stellar activity.

The final phase comprises the cold molecular gas ($n \geq 200\,\mathrm{cm}^{-3}$, $T \sim 10\,\mathrm{K}$) that is confined to giant molecular clouds. The clouds are held together by self-gravity rather than being in equilibrium with the other phases. Molecular clouds represent the locations in the Galaxy where the star-formation process is initiated.

Even to the naked eye, some nearby molecular clouds are visible in silhouette against the bright background of the Milky Way. These regions were first described as being 'holes in the sky' by Sir William Herschel (1785). This perspective did not change until Edward E. Barnard recognised in a photographic survey (1919) that the dark regions were actually discrete nebular objects blocking out the light from more distant stars. Halfway through the 20$^{\text{th}}$ century the association of dark nebulae with star formation became apparent. Bart J. Bok (1948) claimed that the dark nebulae, now called 'Bok globules', are objects where new stars are formed[†].

[†]Remarkably, Emanuel Swedenborg proposed the nebular hypothesis much earlier (1734), based on philosophical arguments. The philosopher Immanuel Kant developed this idea further in 1755 and reasoned that the Solar System originated from a slowly rotating, collapsing nebula.

Present-day technology in infrared and (sub-) millimetre observations allow the direct detection of embedded, low-mass star formation in nearby dark clouds. The term 'low-mass' refers to stars with a mass similar to, or less than, about one solar mass ($1\,M_\odot \approx 2\times10^{33}$ g). 'Nearby' in this respect means within a few hundred parsec ($1\,\mathrm{pc} \approx 3.26\,\mathrm{lightyear} \approx 3\times10^{16}$m). Stars more massive than $8\,M_\odot$ are referred to as high-mass, or massive stars. The recent discovery of distant ($\gtrsim 1$ kpc) and hence more massive dark cloud complexes, the so-called Infrared Dark Clouds, provides the opportunity to study the origin of massive stars and stellar clusters.

This thesis presents a study of the physical characteristics and star-forming properties of dark and massive molecular clouds throughout the Galaxy, with a strong emphasis on the existence of these clouds in the Outer Galaxy. The first chapter introduces various aspects related to the process of star formation. After that, several strategies for observing the early stages of star formation are alluded to. In the final section, an outline of the remaining chapters is given.

1.1 From clouds to stars: A general overview

The cold molecular phase of the ISM consists of a hierarchical structure of molecular clouds, from the giant cloud complexes to the small, gravitationally unstable cores. These different appearances are primarily described by their diversity in size, mass and density. A spontaneous or triggered collapse of the densest parts of molecular clouds initiates the process of star formation.

The first part of this section gives a qualitative description of the observed properties of different manifestations of molecular *'clouds'* in the Galaxy. The use of a consistent nomenclature is somewhat ambiguous, not in the least because of the wide variety in properties. Moreover, in the astronomical literature there is no clear consensus so far on a uniform terminology. Nonetheless, throughout this thesis I will use the descriptions given in Section 1.1.1 whenever possible.

The second part of this section gives an introduction to the relevant time-scales during star formation and summarises our current understanding of the different stages of both isolated low-mass star formation as well as the formation of stellar clusters. The typical shape of the stellar mass-spectrum, referred to as the initial mass function (IMF), is briefly mentioned at the end of the section. Extensive sources of information on both observational and theoretical issues in star formation are, e.g., Stahler & Palla (2005) and McKee & Ostriker (2007). Most of the information in this chapter is adapted from these references and additionally from Bergin & Tafalla (2007) and Tielens (2005), unless specifically stated otherwise.

1.1.1 The hierarchical structure of molecular clouds

Clouds

Molecular Clouds (MCs) constitute most of the cold molecular gas in the Galaxy. They span a wide range of sizes, from small molecular clouds with sizes ~ 20 pc and masses $\sim 10^4\,M_\odot$ (e.g., Taurus MC) to the giant molecular clouds (GMCs) and complexes of sizes $\sim$100 pc and masses $\sim 10^5$–$10^6\,M_\odot$ (e.g., the Orion MC). A typical gas

	Clouds		Clumps	Cores		Globules
	MC[a]	IRDC		stellar	cluster[b]	
size (pc)	20–100	1–10	0.5–10	0.1	1 [0.02]	$\lesssim 1$
density (cm^{-3})	> 200	$>10^4$	10^3–10^4	10^4–10^5	10^6–10^7	10^3–10^4
mass ($M_\odot$)	10^4–10^6	100-10^4	50–1000	0.5–5	10–1000	10–100
temperature (K)	10–30	<25	10–20	<15	<25	< 15

Table 1.1: Overview of the global properties of molecular clouds.

[a] Ranging from small dark clouds to Giant Molecular Clouds
[b] The size in brackets, as well as the density represent values for individual pre-stellar cores in a cluster.

temperature is $\sim 10-30$ K and the mean number density is in excess of $\sim 200\,cm^{-3}$, but, because of the hierarchical build-up these properties may vary significantly between and throughout the clouds.

Dark clouds are nearby molecular clouds that are observed in extinction at optical wavelengths (e.g., Ophiuchus). Dark clouds belong to the group of small molecular clouds described above. They are generally associated with sites of low- and intermediate-mass star formation, whereas the GMCs are often referred to as their massive, cluster-forming counterparts.

Infrared Dark Clouds (IRDCs) were discovered in the mid-90s independently by the Midcourse Space Experiment (MSX; Egan et al. 1998) and the Infrared Space Observatory Camera (ISOCAM; Pérault et al. 1996). They appear as dark, often filamentary structures against a bright mid-infrared background. IRDCs are presumably the direct precursors of clustered, massive star formation and they play an important role in this thesis. Their properties are more extensively discussed in Chapter 2.

Clumps

On scales of ~ 0.5–10 pc molecular clouds often contain filamentary, over-dense substructures referred to as *clumps*. Their masses range from ~ 50 to $1000\,M_\odot$, the gas temperatures are ~ 10–20 K and the number densities range from $\sim 10^3$ to $\sim 10^4$ cm^{-3}.

Cores

Pre-stellar cores are small, gravitationally unstable clouds where eventually a single star or stellar system is formed. Core masses range between 0.5 and $5\,M_\odot$. Their size is of the order of 0.1 pc with a mean number density of $\sim 10^4$–$10^5\,cm^{-3}$. The temperature in the cores can be as low as about 8 –12 K.

Pre-cluster cores are the massive counterparts of pre-stellar cores. With masses ranging from ~ 10 to $1000\,M_\odot$ (or more) they represent the precursors of small, loosely bound stellar clusters as well as massive OB-associations. Pre-cluster cores typically show a lot of substructure and the individual fragments appear to be precursors of single stars or stellar systems. The pre-stellar cores in cluster-forming regions

are more compact (~ 0.02 pc) and denser ($\sim 10^6$–10^7 cm^{-3}) compared to isolated pre-stellar cores (Ward-Thompson et al. 2007, and references therein). Pre-cluster cores are sometimes also called star-forming clumps.

Dark Globules

Dark globules, also referred to as Bok globules, are isolated, gravitationally bound molecular clouds that may have been removed from their parent molecular cloud by external events. Because of their isolation, the distance and consequently distance-related properties of many globules are often uncertain. Estimates of their mean size do not exceed ~ 1 pc (Evans 1999, and references therein). Their mass is of the order of 10 –100 $M_\odot$. The densest parts of globules resemble the pre-stellar cores described above. Low-mass star formation is frequently observed inside.

1.1.2 Relevant time-scales

The equations presented in this section give an idea of the time-scales involved in the evolution from molecular clouds to stars, though they are not meant to give the complete picture. They are expressed in units that are conveniently scalable to values appropriate for various objects. It is important to realise that mass (and density) play a crucial role in the time span of pre-stellar as well as stellar evolution.

Density perturbations can move through molecular clouds at a velocity limited by the speed of sound. The isothermal sound speed is, for typical conditions in the ISM, approximately given by (e.g., Spitzer 1998)

$$c_\mathrm{s} = \left(\frac{kT}{\mu m_\mathrm{H}}\right)^{\frac{1}{2}} \ \mathrm{km\,s^{-1}}\,, \tag{1.1}$$

where k is the Boltzman constant, T is the temperature of the gas, m_H is the mass of a hydrogen atom and μ=2.33 is the mean molecular weight of a particle, consistent with a 25% mass fraction of helium. Typical values in molecular clouds range from about 0.1 to 10 km s^{-1}. The time required for a cloud to approach a dynamical equilibrium state is of the order of the sound crossing-time. This is the time required to traverse the extent of a cloud at the sound speed, i.e.,

$$t_\mathrm{cross} \simeq 10^7 \left(\frac{D}{10\,\mathrm{pc}}\right)\left(\frac{c_s}{1\,\mathrm{km\,s^{-1}}}\right)^{-1} \ \mathrm{years}\,, \tag{1.2}$$

where D is the diameter of a cloud.

In the presence of a magnetic field, additional hydro-magnetic perturbations will move transverse and along the direction of the field lines at the Alvén velocity, given by

$$V_\mathrm{A} = 1.3\left(\frac{B}{1\,\mu\mathrm{G}}\right)\left(\frac{1\,\mathrm{cm^{-3}}}{n}\right)^{\frac{1}{2}} \ \mathrm{km\,s^{-1}}, \tag{1.3}$$

where n is the number density. The field strength B ranges from about 0.001 μG in the diffuse ISM to $\gtrsim 10\,\mu$G in dense cores. Observations show that B scales approximately with the density squared in molecular clouds. Therefore, a typical Alvén

velocity is of the order of $1\,\mathrm{km\,s^{-1}}$. In dense and cold cores, the Alvén speed can exceed the sound speed and become the limiting velocity for perturbations to traverse the medium.

The physical state of molecular clouds is heavily debated amongst experts in the field. It is beyond the boundaries of this thesis to go into the details. I will briefly review the two main directions here.

– quasi-static view –
The first is, that molecular clouds are quasi-static objects formed from the atomic gas phase due to gravitational instabilities. The quasi-equilibrium state of a cloud is maintained by the magnetic field through a magnetic force counteracting gravity and through support by hydro-magnetic waves. A cloud still evolves due to gravity because only charged particles feel the presence of the magnetic field. The majority of the gas is neutral (ionisation fraction $\chi_i \sim 10^{-7}$) and will diffuse inward, slowed down by collisions with the charged particles. This process is known as ambipolar diffusion and occurs on a time-scale given by

$$t_{AD} = \frac{3}{4\pi G \rho \tau_{ni}} \simeq 7.3 \times 10^6 \left(\frac{\chi_i}{10^{-7}}\right) \text{ years} , \tag{1.4}$$

where τ_{ni} is the ion-neutral collision time, ρ the mass density and G the gravitational constant.

– dynamic view –
The opposite view is that molecular clouds are transient objects. They form from convergent flows driven by supersonic turbulence and evolve due to an interplay between gravity and turbulent motions. Hence this process is often referred to as gravo-turbulence. Turbulence dissipates on short time-scales. For supersonic turbulence this is approximately given by (Mac Low & Klessen 2004)

$$t_{\mathrm{turb}} \simeq \frac{L_{\mathrm{d}}}{v_{\mathrm{rms}}} = 10^6 \left(\frac{L_{\mathrm{d}}}{10\,\mathrm{pc}}\right) \left(\frac{v_{\mathrm{rms}}}{10\,\mathrm{km\,s^{-1}}}\right)^{-1} \text{ years} , \tag{1.5}$$

where v_{rms} is the root-mean-square velocity and L_{d} the driving scale of the perturbations. The turbulent dissipation-time is short compared to the crossing-time and suggests that molecular clouds never reach a dynamical equilibrium. In the gravo-turbulent view, clouds are dynamic, transient objects.

For more information on the physical state of molecular clouds I suggest the interested reader to look through McKee & Ostriker (2007) and Bergin & Tafalla (2007) for a concise review and, moreover, follow up on the numerous references they give to original papers on the subject.

The onset of star formation
Initially, a combination of rotation and thermal, magnetic and turbulent pressure in a dense core withstands the inward gravitational force. Once the magnetic and turbulent support dissipate (on times-cales given by Eq. 1.4 and Eq. 1.5) gravity overtakes the thermal pressure. A runaway process starts and a spherical cloud will

gravitationally collapse on a time-scale characterised by the free-fall time given by (Shu et al. 1987)

$$t_{ff} = \left(\frac{3\pi}{32\mathrm{G}\rho}\right)^{\frac{1}{2}} \simeq 2.4 \times 10^6 \left(\frac{n}{200\,\mathrm{cm}^{-3}}\right)^{-\frac{1}{2}} \text{ years} . \tag{1.6}$$

An exact derivation of the collapse criterion, considering only thermal imbalance, can be derived using the virial theorem, defined as $2 \times E_{\mathrm{kinetic}} + E_{\mathrm{gravitational}} = 0$. Collapse occurs when the gravitational energy exceeds twice the kinetic energy, with

$$E_{\mathrm{kinetic}} = \frac{3}{2} nkT \quad \text{and} \quad E_{\mathrm{gravitational}} = \frac{-3GM_{\mathrm{cloud}}^2}{5R_{\mathrm{cloud}}} , \tag{1.7}$$

where M_{cloud} is the cloud mass and R_{cloud} is the cloud radius. This condition can be approximated using the simple argument that the free-fall time should be less than the sound-crossing time. The critical value is usually expressed in terms of mass, referred to as the (thermal) Jeans mass (Jeans 1928). The collapse starts when the mass of a cloud exceeds the Jeans mass, i.e., $M_{\mathrm{cloud}} > M_{\mathrm{J}}$, where the critical mass is approximately given by;

$$M_{\mathrm{J}} = \left(\frac{\pi c_{\mathrm{s}}^2}{G}\right)^{\frac{3}{2}} \rho^{-\frac{1}{2}} \simeq 7.5 \left(\frac{T}{10\,\mathrm{K}}\right)^{\frac{3}{2}} \left(\frac{n_{\mathrm{H_2}}}{10^4\,\mathrm{cm}^{-3}}\right)^{-\frac{1}{2}} \mathrm{M}_\odot . \tag{1.8}$$

The definition of the Jeans mass can be extended (see e.g., Larson 1998; Elmegreen 1999) by including turbulent support,

$$M_{\mathrm{J}} \propto v_{\mathrm{rms}}^4 P^{-1/2} , \tag{1.9}$$

where P is the pressure; or magnetic support,

$$M_{\mathrm{J}} \propto B^3 \rho^{-1} . \tag{1.10}$$

While the gas accumulates at the centre of a cloud, the core continues to contract. Gravitational potential energy is converted to heat, increasing the core temperature until hydrogen fusion can begin. The time-scale in which the pre-hydrogen-burning evolution occurs is given by the Kelvin-Helmholtz time, i.e.,

$$t_{\mathrm{KH}} = \frac{\mathrm{G}M_\star^2}{R_\star L_\star} \simeq 3 \times 10^7 \left(\frac{M_\star}{1\mathrm{M}_\odot}\right)^2 \left(\frac{R_\star}{1\mathrm{R}_\odot}\right)^{-1} \left(\frac{L_\star}{1\mathrm{L}_\odot}\right)^{-1} \text{years} , \tag{1.11}$$

where $M_\star$ is the stellar mass, $R_\star$ the stellar radius and $L_\star$ the stellar luminosity. For a solar type star this stage of the evolution is relatively long, about a few times 10^7 years. For more massive stars however ($> 8\,\mathrm{M}_\odot$), the free-fall time on which the collapse occurs is longer than the Kelvin-Helmholtz time and accretion may continue while the star has already reached the main sequence phase.

1.1.3 The formation of isolated, low-mass stars

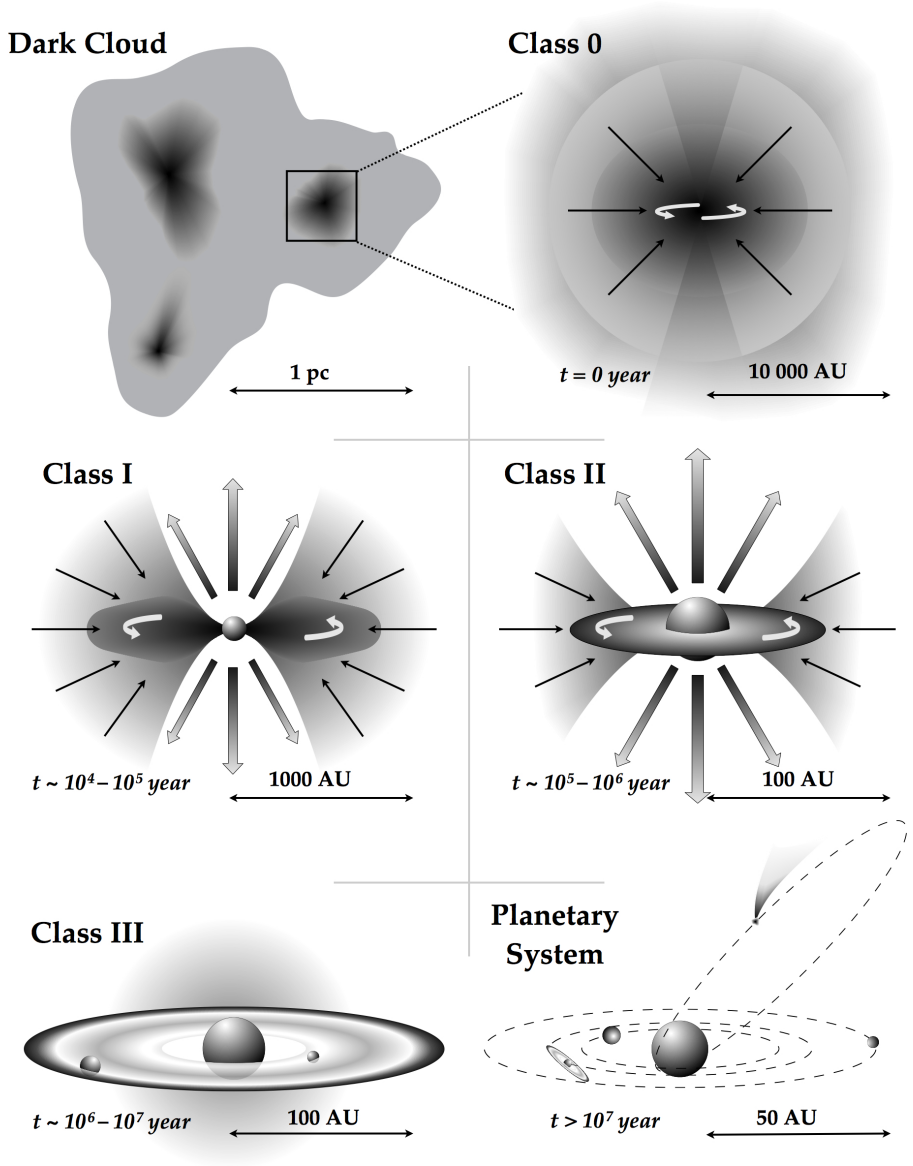

Figure 1.1: This figure illustrates the different evolutionary stages during the formation of an isolated, low-mass star, as described in the text. It is adapted from van Dishoeck & Blake (1998).

Theoretically, the formation-process of low-mass isolated stars ($\sim 1\,M_\odot$) is well understood (Shu et al. 1987). To a certain extent the scenario is observationally confirmed by numerous studies in nearby low-mass star-forming regions. Starting initially as a dense and cold pre-stellar core, the evolutionary sequence is subsequently described by four main stages (Lada 1987). The shape of the near- to far-infrared spectral energy distribution (SED), dominated by the dust emission, is used to classify the stages as class 0, I, II or III objects (e.g., Lada & Wilking 1984; Andre & Montmerle 1994). Figure 1.1 illustrates the stages which are briefly described hereafter. The characteristic shapes of the SEDs are schematically drawn in Figure 1.2.

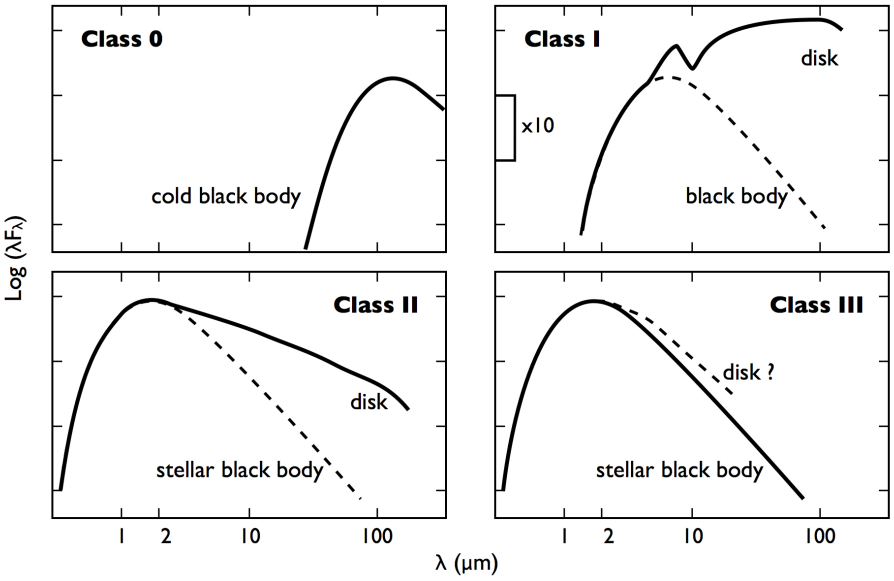

Figure 1.2: Illustration of the evolution of the SED during pre- and proto-stellar stages. Adapted from (Lada & Wilking 1984; Andre & Montmerle 1994).
– *Class 0* – The SED resembles a blackbody spectrum at a temperature below 30 K, peaking at sub-mm wavelengths ($\gtrsim 100\,\mu$m).
– *Class I* – The peak of the SED shifts to far-IR wavelengths ($\lesssim 100\,\mu$m) as the temperature of the dust rises. Emission from both the accreting envelope (~ 100 K) and the thick disk (a few 100 K) are observed. The 10 μm silicate absorption feature is often identified toward Class I objects, indicating that the envelope is optically thick.
– *Class II* –The SED at near-IR wavelengths is dominated by the emission of the central proto-star and typically peaks around 2 μm, corresponding to temperatures around 1000 to 2000 K. At longer wavelengths an infrared excess is observed, originating from the dusty disk.
– *Class III* – The SED resembles a stellar blackbody, peaking at optical or infrared wavelengths. Minor infrared excess is often still observed. Possibly, this is due to the remaining thin disk, but it is also consistent with interstellar extinction due to foreground material.

Dark cloud – In a typical dark cloud, several pre-stellar cores with enhanced densities are present. In the scenario of isolated star formation, these sub-structures are spatially well separated so that they do not interact with each other. Initially, rotation and internal pressure prevent a pre-stellar core from collapse under its own gravity. The core evolves slowly because of ambipolar diffusion (Eq. 1.4) and dissipation of turbulent motions (Eq. 1.5) due to collisions between particles (viscous effects). On time-scales of a few million years the core develops a strong increase in density toward the centre.

Class 0 – Defined at time t=0, the central density of the core becomes so high that gravity overcomes any internal pressure and the core starts to collapse. Due to the collapsing gas, a shock wave propagates outward at the speed of sound and the surrounding material starts falling in as well. This is known as an *inside-out collapse* (Shu et al. 1987). The slow rotational motion of the core that is present from the start is enhanced as accretion proceeds. Observational evidence of bipolar outflows at these stages (e.g., Lada 1999) suggests a non-spherical collapse. This might indicate that the formation of a disk starts early in the formation-process.

Class I – After about 10^4 to 10^5 years, the collapsing core becomes so dense that cooling radiation is trapped and heats the environment. The temperature of the central object increases gradually to a few hundred degrees and a proto-star is formed. Due to rotation, the angular momentum forces the collapsing envelope to accrete onto a thick circumstellar disk. The material in the disk continues to spiral in and onto the proto-star, allowing it to grow in size and mass. Excess angular momentum is expelled into the surrounding medium in the form of collimated jets and outflows along the rotation axis.

Class II – About a million years after the initial collapse, most of the envelope has been removed and the embedded object becomes visible at optical and infrared wavelengths. At this stage, the bulk of the material has accreted onto the central object. A flattened circumstellar disk is present in which material moves inward at a decreasing rate. The disk contributes only about 1% of the total mass of the system. Planet formation may have started. Material from a remaining envelope may still accrete onto the outer parts of the disk. The object is referred to as a classical T-Tauri star, after the prototype T-Tauri. The luminosity of the star is driven by compression due to its own gravity. This stage initiates the pre-main sequence stage of a star.

Class III – At some point, between 1 to 10 million years, accretion has come to a stop completely. Most of the primordial material in the disk is lost. What remains is a debris disk. The temperature and density of the pre-main sequence star keep increasing as the object slowly contracts to its final size. Class III objects are sometimes called weak T-Tauri stars.

Main sequence star – When the temperature in the centre of the star reaches about 10 million degrees, hydrogen fusion begins. The star settles onto the main sequence evolutionary track and will continue burning hydrogen for several billion years.

1.1.4 The formation of massive stars and stellar clusters

The formation of massive stars is poorly understood compared to their low-mass equivalents. From the observational point of view, massive star formation is more difficult to study in detail for a number of reasons. First of all, massive stars are rare (see also Section 1.1.5). Therefore, their formation sites are located at large distances ($\gtrsim$1 kpc) making it difficult to spatially resolve them. Second, the lifetime of massive stars, including the formation-process, is shorter by orders of magnitude ($\sim 10^5$ years, see Section 1.1.2). To make things even more complicated, the formation-process occurs deeply embedded in the densest parts of molecular clumps, hidden almost completely from view.

Theoretically, the difficulty is that massive stars form almost exclusively in stellar clusters (Blaauw 1964; de Wit et al. 2005). Complications in the clustered star formation process are among other things the role of feedback from massive stars on their environment and the strong interaction between different star-forming events due to their proximity.

Young massive star clusters in our Galaxy have a stellar mass-content of the order of 1000 $M_\odot$ (e.g., Orion OB1) to 10 000 $M_\odot$ (e.g., Arches cluster). Clearly, such massive clusters must originate from molecular clouds that have sufficient material available to transform large amounts of mass into stars, the Giant Molecular Clouds. Inside these massive clouds, dense filaments fragment and collapse to form dense pre-cluster cores. On spatial scales of the order of the size of pre-cluster cores ($\lesssim$ 0.1 pc), a number of subsequent stages in the formation-process of clusters have been identified, i.e., cold dense clumps, hot cores, hyper- and ultra-compact HII regions and OB-associations.

On even smaller spatial scales, the individual, dense, collapsing cores produce stars of all masses that will give rise to the stellar cluster. The exact formation-process of individual stars in a cluster, specifically the massive ones, is strongly debated. Various scenarios have been suggested. I will review three popular theories that have been proposed recently:

- *Competitive Bondi-Hoyle accretion* (Bonnell et al. 1997, 2001)
  In dense clusters, accreting objects are competing for the same material that is available. Simulations show that two different regimes are recognised in the accretion process. One is, when the gravitational potential is dominated by cold gas. In this regime, low-mass stars accrete the majority of their mass. The other is when the stars that have formed dominate the gravitational potential. At this stage, high-mass stars accrete most of their mass. The latter occurs first at the centre of a cluster, which explains why the most massive stars are usually found in cluster cores (Bonnell & Davies 1998). This model accounts for the observed mass distribution of stars more massive than 0.5 $M_\odot$. However, for stars more massive than 10 $M_\odot$, the radiation pressure of the central object suppresses further accretion.

- *Stellar mergers* (Bonnell et al. 1998)
  The merging mechanism is proposed to avoid the problem of direct accretion of material onto proto-stars more massive than about $10\,M_{\odot}$, where radiation-pressure becomes too large. Instead, in the central parts of a cluster, intermediate-mass stars form through accretion onto lower mass objects as the cluster itself decreases in radius due to global collapse. At some point, the central density becomes so large that the intermediate-mass objects merge and form massive stars. This process can occur only at very high stellar densities ($\gtrsim 10^8\,pc^{-3}$), which have not been observed so far. The model also predicts a large number of binary stars due to tidal captures. Note here, that massive stars indeed have a high degree of multiplicity compared to low-mass stars, i.e., an average massive stars has 1.5 companions against 0.5 for a solar-type star.

- *Turbulent core model* (McKee & Tan 2003)
  This model extends the low-mass formation picture that stars form through accretion onto a central object. This model suggests that massive molecular cores are supersonically turbulent even on the small scales where individual stars form. This implies an accretion rate that is high enough to overcome any radiation pressure of the central object. Furthermore, the accretion rate increases with time and can account for the short formation time-scale ($\sim 10^5$ years) of massive stars.

Up to now, the issue of how massive stars are formed remains unresolved. Apparently, different evolutionary stages of individual stars are present at the same instant in a cluster environment. The proposed evolutionary scenario of massive, clustered star formation is schematically given in Figure 1.3. The description of the different stages presented below is based on observational knowledge and is far from complete. It is meant to be merely descriptive.

GMC – Largely due to turbulent compression, driven by supernova shock waves, molecular clouds show a substructure that is highly filamentary. The gradual collapse under gravity and further compression due to shocks results in the formation of massive, dense clumps on scales of a few parsecs. These clumps are considered the pre-cursors of stellar clusters. Manifestations of cold clumps are presumably represented by the cold, centrally peaked sub-millimetre clumps observed in many IRDCs (see also Chapter 2).

Collapse – Defined at time t=0, gravitationally unstable pre-cluster cores of sizes less than $\sim$1 pc and masses ranging from 100 to $1000\,M_{\odot}$ start to collapse rapidly. Initially, the temperature in the cores is still low ($\lesssim 20$ K). The clumps fragment further into pre-stellar cores that presumably undergo strong interaction with each other due to their small separation. A complicated, so far unresolved process (see the aforementioned formation mechanisms for individual massive stars) of clustered star formation starts to develop.

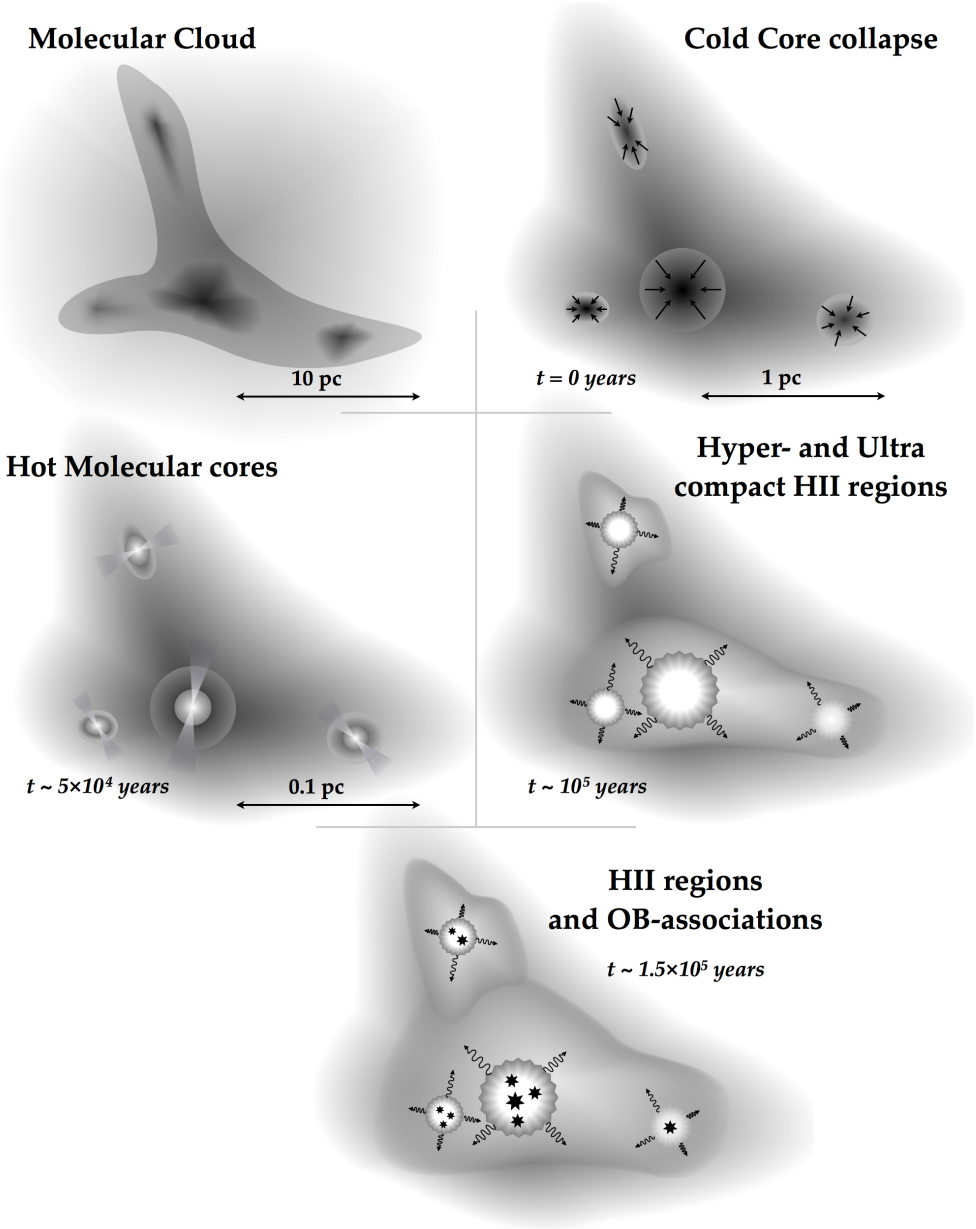

Figure 1.3: This figure displays a schematic illustration of the various observed stages during the formation of a massive stellar cluster, as described in the text.

Hot core – While the clump in whole is probably still collapsing, the excess angular momentum of individual proto-stellar objects drives jets and outflows into the surrounding envelope. Due to heating from the outflows, and from the proto-stellar cores, the temperature near the star forming activity in the clump rises to a few 100 K. This is sufficient to evaporate many of the ices from the dust grains. This hot region is about 0.1 pc in size and is observationally characterised by a rich gas-phase chemistry.

HC/UC-HII – Perhaps already during the hot core phase, the first massive proto-stars begin to fuse hydrogen. Their strong radiation ionises the gas and destroys complex molecules in their immediate surroundings. Observationally, this stage is identified as a hyper-compact HII region (HC-HII). The size of the ionised region is initially less than $\sim$0.01 pc. As the ionisation front expands ($<$0.1 pc) and further accretion ceases, the massive star reaches its final stage. The cluster is still embedded in an envelope of gas and dust and is referred to as an Ultra-Compact HII region (UC-HII).

OB-stars – About 150 000 years after the initial collapse, the HII region breaks through the surrounding envelope and the cluster of stars becomes visible. The presence of massive type O- and B-stars in the cluster gives rise to the name OB-association. The immediate surrounding of massive stars consists mainly of ionised gas and is prominently observed as classical HII regions.

1.1.5 The Initial Mass Function

Massive stars produce $\sim$99% of the UV photons in the Galaxy and are likely to be the dominant sources that ionise large parts of the ISM (the warm and hot ionised gas phase). However, massive stars are rare. By number they account for only $\sim$1% of all stars.
The function that describes the distribution of stellar masses for a given stellar population is referred to as the Initial Mass Function (IMF). Observational evidence suggests that the IMF is very similar in most directions in our Galaxy. The IMF is defined as the number of stars $\xi(m)\,dm$ that are produced in a mass interval m to m+dm and can be written as a power-law

$$\xi(m) \propto m^{-\alpha}\,, \tag{1.12}$$

where α is defined as the power-law value. Salpeter (1955) identified a power-law with $\alpha = 2.35$ for stars more massive than $1\,\mathrm{M}_\odot$. Hence, the high-mass end of the mass distribution is often referred to as a the Salpeter function. Miller & Scalo (1979) showed for stars in the solar neighbourhood that the distribution breaks around $1\,\mathrm{M}_\odot$ objects, where the slope turns shallower. With the sensitive telescopes available at present, the low-mass end of the mass distribution can be studied as well. A standard IMF that is often used and covers the whole range of observed masses is given by Kroupa (2001) and consists of three parts (see Figure 1.4):

$$\alpha = 2.3 \quad 0.5 < \frac{m}{\mathrm{M}_\odot} < 50$$

$$\alpha = 1.3 \quad 0.08 < \frac{m}{\mathrm{M}_\odot} < 0.5 \tag{1.13}$$

$$\alpha = 0.3 \quad 0.01 < \frac{m}{\mathrm{M}_\odot} < 0.08$$

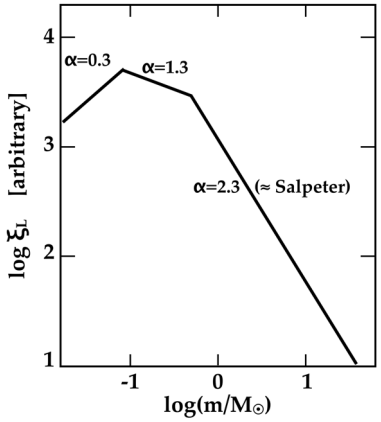

Figure 1.4: Illustration of the IMF described by Equation 1.13. Note on the y-axis $\xi_L(m) = (m \ln 10)\,\xi(m)$

There are indications that the IMF is not as universal as initially thought. In our own Galaxy, variations have been identified toward star clusters located near the Galactic centre (Scalo 1998). In addition, in external galaxies there is evidence that the stellar mass distribution deviates from the standard IMF as observed in our Galaxy. For example, a detailed study of young super star-clusters in the nuclear starburst galaxy M82 (McCrady et al. 2005) reveals variations of the IMF, although mass segregation is an issue.

1.2 Observing the early stages of star formation

From the previous sections, it is clear that the initial stages of clustered star formation are represented by the cold, dense and massive clumps inside Giant Molecular Clouds. On many occasions, distinct regions in the same GMC represent different evolutionary stages of star formation. The main subject of this thesis is an investigation of the early stages of clustered star formation, however, more evolved regions are often encountered in the observations.

In this Section I briefly discuss the observational possibilities that enable a detailed analysis of the physical conditions in different stages of star formation. I will focus mainly on observations that have been essential for the motivation of this thesis.

1.2.1 Interstellar dust

The mass of a molecular cloud consists for about 1% of dust. In general, silicates and graphite are considered the main constituents of interstellar dust. The dust grains have a broad range in size, from only a few molecules sticking together to micrometer sized aggregates. A significant fraction of the total mass of dust is contributed by large grains, i.e., $\gtrsim 0.01\ \mu$m.

Emission characteristics

Except for the smallest grains, interstellar dust is in general close to being in thermal equilibrium with its surroundings. The temperature of dust grains is regulated by various heating mechanisms, depending on the location in a cloud. The interstellar radiation field (ISRF) is the dominant heating source in the outer –lower density– layers of clouds. The grains absorb the stellar radiation and re-emit their energy at typical temperatures around 30 K. Going deeper inside the cloud, most of the ISRF-photons are absorbed and the temperature drops. At high densities ($>10^4$ particles cm^{-3}), the dust is thermally coupled to the gas through collisions. The heating is only due to cosmic rays that penetrate the dense cores and ionise the gas. Even though the energy input per cosmic ray can be enormous, the low rate at which events occur ($\sim 10^{-17}\,s^{-1}$) yields a temperature of only 8 to 10 K. On small spatial scales, temperatures can increase due to local events such as compression, shocks, outflows and radiation from nearby (proto-) stars.

Large grains ($\gtrsim 0.01\,\mu$m) can be treated as blackbodies. The re-emitted radiation of large grains is observed as a modified blackbody spectrum. The intensity I as a function of wavelength λ is expressed as the Planck law multiplied by $M(\lambda)$;

$$I_\lambda(T) = M(\lambda)\frac{2hc^2/\lambda^5}{\exp(hc/\lambda kT)-1}\ . \tag{1.14}$$

Here h is the Planck constant, c is the speed of light, k is the Boltzman constant and T the temperature of the dust. The modification factor can be written as

$$M(\lambda) = 1 - \exp\left[-\tau_{\lambda(0)}\left(\frac{\lambda(0)}{\lambda}\right)^{\beta}\right]\ , \tag{1.15}$$

where $\tau_{\lambda(0)}$ is the optical depth at a reference wavelength $\lambda(0)$ and β is a correction factor depending on the intrinsic dust properties, mainly the size-distribution and composition. Values for β may vary between about unity and 3. Considering the low temperatures in molecular clouds, the majority of the energy is emitted at far-infrared and sub-millimetre wavelengths. The radiation at these long wavelengths is optically thin ($\tau \ll 1$, i.e., radiation can freely escape the cloud). Therefore, the observed intensity is a direct measure of the total column of radiating dust along the line of sight. The wavelength at which the peak of emission occurs ($\lambda_{\rm max}$) relates to the temperature ($T_{\rm dust}$) of the dust and is given by Wien's Law;

$$\lambda_{\rm max} T_{\rm dust} = 0.29\ {\rm cm\ K} \tag{1.16}$$

Small dust grains (i.e., $\sim$20–50 Å) cannot be considered as blackbodies. They readjust to higher temperatures compared to large grains and emit their energy at infrared wavelengths, typically around $\sim 60\,\mu$m for small grains and $\sim 25\,\mu$m for the very small grains. The Polycyclic Aromatic Hydrocarbons (PAHs) account for most of the grains at molecular size scales (4–20 Å). These grains are not in thermal equilibrium with their surroundings. A random absorption of photons heats the individual grains to a range of temperatures. The energy is re-emitted at very specific

wavelengths, predominantly in the near- to mid-infrared, depending on the internal properties of the grains (e.g., Tielens et al. 1999). Frequently used models that describe the grain size distribution and dust composition of the ISM as well as present synthetic dust emission spectra are, e.g., Draine & Li (2001, 2007); Weingartner & Draine (2001).

Extinction characteristics

The presence of dust in the ISM is prominently observed at optical and infrared wavelengths due to the absorbing and scattering properties of dust grains. Star counts were recognised as early as in the mid-20s of the previous century as a powerful tool to map nearby dark globules (Wolf 1923). The amount of extinction at wavelength λ, usually converted to magnitudes of visual extinction (A_V), can be derived directly by comparing the stellar distribution behind the dust with an extinction-free off-position, i.e.,

$$A_V = \frac{1}{b_\lambda}\frac{A_V}{A_\lambda}\log\frac{N_{\rm off}}{N_{\rm on}}\ {\rm mag}, \tag{1.17}$$

where b_λ is the slope of the cumulative λ-luminosity function, $N_{\rm off}$ is the stellar surface density at the off-position and $N_{\rm on}$ is the stellar surface density in the target direction. The ratio A_V/A_λ is the reddening-law and depends on the dust properties. Star counts require a completeness-, or magnitude-limited, set of observations and assume that all observed stars are behind the obscuring material.

In particular at infrared wavelengths, the colour excess of objects behind the dust can be used to measure the extinction. The colour excess is defined as the difference between the observed colour and the intrinsic colour of a source, e.g., for $H-K_{\rm S}$ the colour excess is given by

$$E(H-K_{\rm S}) = (H-K_{\rm S})_{\rm observed} - (H-K_{\rm S})_{\rm intrinsic}\ {\rm mag}. \tag{1.18}$$

Often, the intrinsic colour of individual sources is unknown. However, the near-IR $H-K_{\rm S}$ colour spans only a narrow range for the majority of stars, i.e., about 0.00 to 0.30 mag for spectral types A0V to M6III (Bessell & Brett 1988) with a mean of $\sim$0.15 mag. Typical $H-K_{\rm S}$ extinction values toward the denser parts of molecular clouds are in excess of 0.3 mag, i.e., a mean $(H-K_{\rm S})_{\rm observed} > 0.45$ mag. The infrared colour excess is often converted to visual extinction by multiplication with a constant. This conversion assumes that the reddening-law is known.

1.2.2 Molecular gas

A continuation of the initial collapse of a molecular cloud requires that the material cools down to suppress the thermal and turbulent support. Molecules are very effective in cooling the gas, because of the presence of many rotational energy levels. Transitions between different levels involve only small amounts of energy, i.e., for many molecules the lowest transitions require less than $\sim$10 K. The emitted radiation is therefore dominant in the (sub-) millimetre regime, unlike vibrational or electronic transitions which emit predominantly at infrared and optical wavelengths, respectively. Because of these low energies, the first rotational levels of molecules are

easily populated, even in cold regions. Most of the spectral lines observed toward cold molecular gas are due to pure rotational transitions.

Rotational transitions

In this thesis mainly the rotational transitions of diatomic molecules (mostly CO) are used. The energy levels are characterised by the rotational quantum number J, which denotes the magnitude of the total angular momentum. For diatomic (and linear) molecules, the energies are approximately given by the levels allowed for a rigid rotator, i.e.,

$$E_J = BJ(J+1), \quad J = 0, 1, 2, 3... \tag{1.19}$$

The rotational constant B is given by

$$B = \frac{h^2}{8\pi^2 I}, \tag{1.20}$$

where h is the Planck constant and I the moment of inertia of the molecule. An observer detects the photons that are emitted due to radiative de-excitation from an upper to a lower level. The notation that is generally used, for example for the transition between the $J = 2$ and $J = 1$ level of carbon monoxide is CO 2-1. For radiative rotational transitions, the only allowed transitions between different J levels obey the selection rule

$$\Delta J = \pm 1. \tag{1.21}$$

The energy corresponding to a transition is given by

$$E(J+1) - E(J) = 2B(J+1). \tag{1.22}$$

From this equation, it follows that the rotational spectrum of a molecule consists of evenly spaced lines in the frequency domain. Also, massive molecules have a large inertial momentum I and thus, the energy levels are more closely spaced than less massive molecules.

Critical density, optical depth and intensity

The energy level populations are determined by solving the statistical equilibrium between the excitation and de-excitation of the molecules due to both radiation and collision. Radiation can excite molecules through absorption, and de-excite molecules through spontaneous or stimulated emission. Collisional energy-exchange between molecules (or other collisional partners such as atoms or electrons) can also result in both excitation and de-excitation. In molecular clouds it is usually sufficient to take into account only molecular hydrogen as a collision partner.

In order to simplify the problem, consider a two-level molecule where subscripts u and l denote the upper and lower level, respectively. The equilibrium equation is then given by

$$n_l n\gamma_{lu} + n_l B_{lu} J_{ul} = n_u n\gamma_{ul} + n_u A_{ul} + n_u B_{ul} J_{ul} \ , \tag{1.23}$$

where B_{lu}, B_{ul} and A_{ul} are the Einstein coefficients giving the absorption rate, the stimulated emission rate and the spontaneous emission rate, respectively. The γs

are the collisional rate coefficients. The number density is given by n and the mean photon radiation field is J_{ul}. Solving this equation is not straightforward, because at any location in a cloud the level populations depend on the radiation field while the radiation field itself is determined (partly) by the level populations everywhere.

For a detailed evaluation of the equilibrium equation as well as the basics of radiative transfer I encourage the reader to have a look at Rybicki & Lightman (1986). I will only briefly touch upon some key-topics here to clarify two parameters that will be discussed further on in the thesis, i.e., the critical density and the optical depth.

An important parameter that is used when solving the equilibrium equation is the critical density $n_{\rm cr}$, i.e., the density at which the radiative decay rate equals the collisional de-excitation rate. If we ignore photon-trapping for the moment (optically thin limit), the critical density is defined as the ratio of the de-excitation rates through spontaneous emission and collision, respectively;

$$n_{\rm cr} = \frac{A_{ul}}{\gamma_{ul}} \, . \tag{1.24}$$

The Einstein A_{ul} coefficient is the radiative de-excitation rate. A_{ul} scales with the frequency cubed ($A_{ul} \sim \nu^3$) and thus, higher energy transitions have a higher critical density. The collisional de-excitation rate coefficient γ_{ul} depends on the de-excitation cross-section and the density of the collision partner. A useful implication of the critical density for observers is, that the detection of specific molecules and transitions can be used as constraint on the number density in the region they are observed. In particular, in Chapter 5 we make use of the detection of the $C^{34}S$ 2-1 transition as a probe for high density ($n_{\rm cr} \approx 5{\times}10^5 {\rm cm}^{-3}$) cores.

In the case of an optically thick transition, some of the emitted photons are reabsorbed. The absorption is characterised by the absorption coefficient α_ν. Reabsorption has no net effect on the level populations in a cloud, because a photon that is emitted due to de-excitation of one molecule excites another molecule elsewhere in the cloud. As a result, the critical density is lowered by $1/\tau_\nu$. Here, τ_ν is the optical depth of the line, defined as the integral of the absorption coefficient over the traversed path s, i.e.,

$$\tau_\nu(s) = \int_0^s \alpha_\nu(s')ds' \tag{1.25}$$

At densities much below the critical density ($n \ll n_{\rm cr}$), molecules are radiatively deexcited at a much faster rate than they are de-excited by collisions. At high densities ($n > n_{\rm cr}$), collisions dominate the de-excitation process and the gas is in local thermodynamic equilibrium (LTE).

It is instructive to mention here the dependence of the emergent intensity in a line, i.e., the intensity that is observed by a telescope. In the optically thin limit ($\tau \ll 1$), the intensity scales linear with the column density in the upper level and thus can be used to estimate the total column of material along the line of sight. In case of an optically thick line ($\tau > 1$), the intensity is given by multiplying the Planck function

with the width of the line. This means the intensity is a direct measure of the excitation temperature $T_{\rm ex}$ of the gas. This immediately gives an approximation of the kinetic temperature $T_{\rm kin}$, because at high density $T_{\rm ex} \simeq T_{\rm kin}$.

Line width – size relation

The observed broadening of spectral lines toward molecular clouds is dominated on most spatial scales by supersonic motions. A power-law relation between the velocity dispersion σ (km s^{-1}) inside a dark cloud and the physical extent L (pc) was recognised from observations by Larson (1981) and is written as

$$\sigma = 1.1 L^{0.38} \, . \tag{1.26}$$

The equation is empirically derived for molecular cloud sizes ranging from about 0.1 to 100 pc. The result is almost identical to what is expected on the basis of the classical Kolmogorov law of incompressible turbulence. Because no systematic evidence for other mechanisms is present, such as rotation or in- and outflow motions, the supersonic motions are generally ascribed to the presence of turbulence in molecular clouds.

Molecular hydrogen or carbon monoxide

Molecular hydrogen (H_2) is by far the most abundant molecule in the ISM. However, H_2 is a homonuclear molecule and does not have a permanent dipole moment. This means that it has no allowed dipole transitions. Weak quadrupole transitions ($\Delta J = \pm 2$) do exist, but the energies involved are high, e.g., $E_{J=2} - E_{J=0} \sim 510$ K. Consequently, H_2 is difficult to observe in molecular clouds and cannot be used to trace the molecular content of the Galaxy.

Carbon monoxide (CO) is the most abundant molecule in the ISM after H_2. It is the dominant coolant in cold gas and is widely used as a tracer of molecular gas. The lower rotational transitions require low energies (e.g., $E_{J=1} - E_{J=0} = 5.5$ K) to jump to the first excited rotational states. CO is observed everywhere in molecular clouds. Even though the abundance of CO is low ($\sim 10^{-4}$), the immense column densities in molecular clouds make CO molecules optically thick to their own radiation. This means that the observed CO emission is predominantly coming from the outer layers of molecular clouds. To acquire information on the entire column of CO along a line of sight, which may be converted to a mass column of gas assuming a standard abundance, it is essential to observe the rare isotopes, e.g., ^{13}CO and C^{18}O (abundance ratios are ≈ 50 for ^{12}C/^{13}C and ≈ 500 for ^{16}O/^{18}O).

1.3 Thesis outline

Chapter 1 presents a general review of the current knowledge on star formation and introduces some of the basic physics related to the subject.

Chapter 2 gives an overview of the global properties of IRDCs. I describe the initial identification and spatial distribution toward the Inner Galaxy and give typical

values for the mass, density and temperature. At the end of the chapter I address the main topic of this thesis.

Chapter 3 introduces a statistical approach to identify extended red regions from the Two Micron All Sky Survey (2MASS) in the Outer Galaxy. I explain how we use the Mann-Whitney U-test and a cluster finding algorithm to produce a list of candidate dark clouds. The catalogue is cross-correlated with existing infrared and optical data.

Chapter 4 continues the identification of Outer Galaxy dark clouds by matching candidates with CO data from the FCRAO survey. The presence of CO suggests that the identified objects are red because the 2MASS sources are embedded in, or behind a molecular cloud.

Chapter 5 provides a detailed analysis of molecular line observations toward the dark cloud candidate G111.80+0.58 in the vicinity of NGC 7538. The global properties that I present suggest that the cloud is in an early, but not pristine stage of star formation. The cloud appears to be very similar to Inner Galaxy IRDCs and I conclude that this is very likely the first Outer Galaxy IRDC-like object identified as such.

Chapter 6 presents mid-infrared Spitzer observations of G111.80+0.58. The conclusion is simple. G111.80+0.58 is observed in extinction at 8 micron and thus can be classified as the first real IRDC in the Outer Galaxy. More Spitzer data are expected in the near future that will allow a detailed investigation of the proto-stellar properties of several young stellar clusters associated with the dark cloud complex.

Chapter 7 summarises the main conclusions of the thesis. I address some of the future prospects arising from this thesis.

Chapter 2

Infrared Dark Clouds in the Inner Galaxy

A general overview

W. W. F. Frieswijk

ABSTRACT

INFRARED DARK CLOUDS (IRDCs) are presently believed to be the progenitors of massive stars and stellar clusters. In this chapter I briefly summarise the current knowledge that we have on these objects. I refer to several studies that are available in the literature. This overview is by no means complete. The research into the early stages of clustered star formation constitutes an active topic within astronomy which makes it difficult to be up-to-date.

I start with the discovery of IRDCs in the mid-90s by the MSX and ISOGAL projects and give an overview of the global physical properties that are observed. Thereafter, I describe some of the more recent results of detailed studies that have been conducted, mostly on individual objects or small samples. These studies have pointed out the relation between IRDCs and star formation. At the end of this chapter I discuss the IRDCs in a Galactic context and introduce the search for IRDCs in the Outer Galaxy; the main subject of this dissertation.

2.1 The discovery of Infrared Dark Clouds

Two independent surveys, both active in the mid-1990s, revealed a previously unknown class of objects that was given the name Infrared Dark Clouds (IRDCs), i.e., the Midcourse Space Experiment (MSX, Egan et al. 1998; Price 1995) and the Inner Galactic Plane survey carried out with the Infrared Space Observatory Camera (ISOCAM, Pérault et al. 1996). Both surveys identified many dark silhouettes against the bright mid-IR (8–15 μm) emission emerging from small and hot dust particles present in the Galactic Plane. The idea that these dark features constitute real objects, rather than being 'holes' in the Galactic Plane, suggests the presence of large column densities of material ($N_{\rm H_2} \gtrsim 10^{23}\,{\rm cm}^{-2}$) in order to explain the extinction at mid-IR wavelengths (an $A_{\rm V} \gtrsim 50$ mag is no exception, e.g., Hennebelle et al. 2001; Egan et al. 1998).

2.1.1 Initial results

Early investigations reported lower limit estimates on the distance to some of the larger objects of 2 kpc. This was derived by looking at spectroscopic parallaxes of foreground stars (Egan et al. 1998). Observations of millimetre transitions of H_2CO lines indicated the presence of dense material toward 11 clouds and resulted in similar kinematic distance estimates, i.e., between 2 and 6 kpc (Carey et al. 1998). At these large distances, the diameters of IRDCs are of the order of 1 to 10 pc. Large velocity gradient (LVG) models of the H_2CO lines suggested molecular hydrogen densities in excess of $10^5\,{\rm cm}^{-3}$ (Egan et al. 1998).

Despite the presence of large column- and volume densities, follow-up observations of the ^{13}CO and C^{18}O emission were reported to be surprisingly weak (Teyssier et al. 2002). The interpretation that was given is, that a large fraction of the molecules is depleted onto cold dust grains. The temperature in IRDCs is indeed low. This was already suggested by the lack of emission at 100 micron (Egan et al. 1998). Temperatures above 13 K should have detectable emission at 100 micron in IRAS images, according to Clark et al. (1991). Excitation analysis of sub-millimetre lines and SED models of sub-millimetre continuum emission, e.g., Teyssier et al. (2002); Carey et al. (1998) resulted in kinetic temperatures for most observed IRDCs below 20 K.

Distance	>1 kpc
Size	1–10 pc
Mass	a few 100 – a few 1000 $M_\odot$
Temperature	<25 K
Volume density	$>10^4\,{\rm cm}^{-3}$
Column density	$>10^{23}$–$10^{25}\,{\rm cm}^{-2}$

Table 2.1: Overview of the typical characteristics of IRDCs. Based on these global properties, IRDCs were initially suggested to represent the earliest, cold stages of clustered star formation. Recent studies have revealed that several IRDCs are associated with active star formation (see Section 2.2).

Table 2.1 presents a general overview of the physical properties of IRDCs. Even though IRDCs possess a large range of properties they do constitute a specific group of objects in our Galaxy. They show different properties compared to, e.g., molecular clouds, cloud cores and isolated dark clouds (compare also Table 1.1, Chapter 1). Most noticeably, their mass and size are comparable to values found for molecular clumps whereas the densities are similar to values found for star forming cores.

2.1.2 Galactic distribution

Many thousands of dark features were identified in the mid-IR images of both MSX and ISOCAM. Only recently, a systematic extraction was performed on the MSX survey. This resulted in a catalogue of over 10 000 objects (Simon et al. 2006a) which reports the position, size, orientation and some contrast properties derived from the 8 micron observations. Not surprisingly, the spatial distribution of IRDCs follows the diffuse mid-IR background of the Galactic Plane. In particular, an increase of the number of objects is observed toward bright star-forming regions, spiral arms and the Galactic molecular ring.

2.2 IRDCs and star formation

After the discovery of IRDCs, Egan et al. (1998) suggested that they likely represent a cold and quiescent class of massive molecular clumps. Indeed, at that point there was no direct evidence for any presence of star forming activity.

However, a continually increasing amount of studies shows that many IRDCs are definitely associated with star formation, e.g., Wang et al. (2008); Beuther & Steinacker (2007); Rathborne et al. (2007). In Sections 2.2.1 and 2.2.2 below, I briefly discuss two distinct observational directions, i.e., using sub-millimetre data and infrared data, and I include some additional references. These studies, amongst many others, have resulted in the current idea that IRDCs represent the earliest stages of clustered star formation. In the literature there is many more data available. For an overview of the latest developments I encourage the interested reader to have a look at recent conference proceedings, e.g., 'Massive Star Formation: Observations confront Theory' (Heidelberg 2007).

2.2.1 Sub-millimetre continuum observations

Because of their large column densities and low temperatures, IRDCs are particularly bright at (sub-)millimetre wavelengths due to cold dust emission. Moreover, many IRDCs that have been observed in the radio continuum show the presence of one or multiple centrally peaked (sub-)millimetre cores (e.g., Carey et al. 2000; Redman et al. 2003). A typical example of the dust emission toward IRDCs is given in Figure 2.1 which displays the 450 micron emission toward IRDC DF3103, observed with the SCUBA bolometer array on the James Clerk Maxwell Telescope. The data are part of a larger set of IRDCs that have been mapped in the sub-millimetre wavelength regime, both in continuum and in lines (CO, $C^{18}O$, Frieswijk et al. in progress).
Rathborne et al. (2005) investigate the bolometric luminosities toward a number of

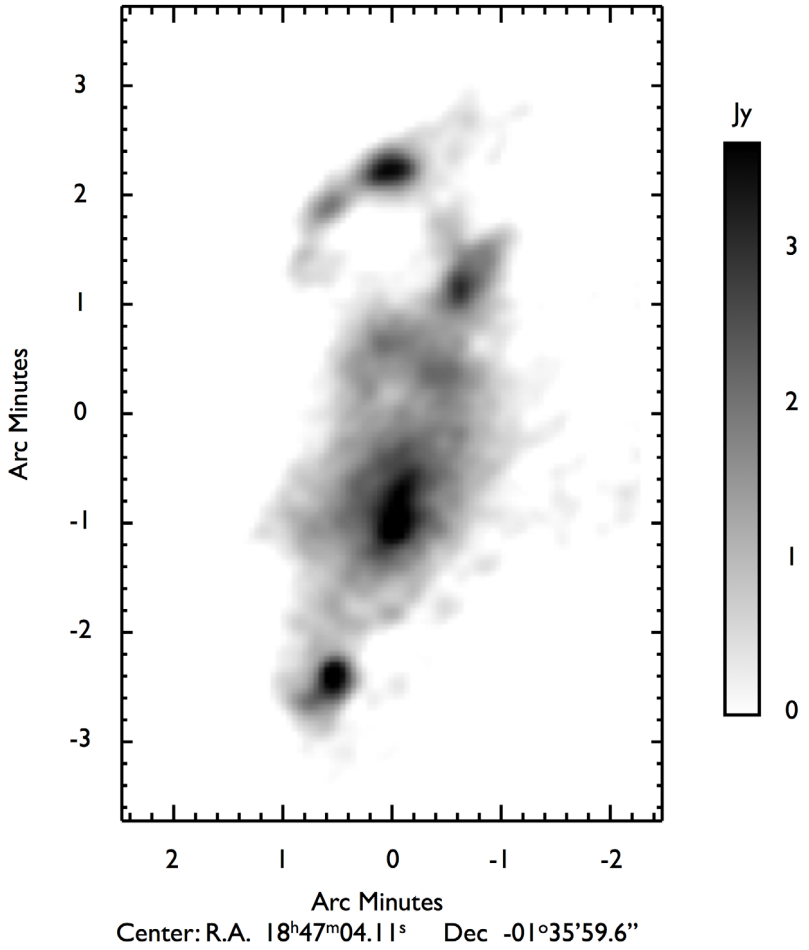

Figure 2.1: SCUBA 450 μm emission toward IRDC DF3103 illustrates the presence of multiple bright sub-mm cores in IRDCs. This object is studied in detail by Teyssier et al. (2002).

sub-millimetre cores in the IRDC labelled MSXDC G034.43+00.24, located at a kinematic distance of 3.7 kpc. The high luminosities ($\gtrsim 10{,}000\,L_\odot$), derived by fitting the spectral energy distribution from mid-IR to millimetre wavelengths, suggest that the cores contain massive proto-stellar objects. The same study shows observations of strong, broad SiO emission toward the sub-millimetre cores. Because SiO preferentially forms in shocks, this detection supports the suggestion of a presence of (massive) star forming activity.

In another study, Ormel et al. (2005) investigate the sub-millimetre emission of the IRDC labelled G48, located at a kinematic distance of 2.7 kpc in the foreground of the W51 complex (see also Figure 2.2). With a self-consistent model of the dust emission, they derive core luminosities of a few 100 $L_\odot$. While they do not claim to have identified the source of the luminosity, these values correspond to a luminosity of intermediate mass stars (B5–B8). Additionally, their models show that the envelope mass is of the order of 100 $M_\odot$.

2.2.2 Mid-infrared Spitzer observations

The unprecedented sensitivity and spatial resolution of the instruments on board the Spitzer Space Telescope supersede the earlier observations of MSX and ISO, especially when IRDCs are concerned. I want to present one example of Spitzer observations taken with the Infrared Camera Array (IRAC) to give an example of how IRDC are observed at mid-IR wavelengths. Figure 2.2 displays a false-colour composite image of IRDC G48. The dark silhouette is very sharply defined at 5.8 μm (yellow) and 8 μm (red). An ongoing investigation into the details of these observations, combined with data from the Multiband Imaging Photometer on Spitzer is ongoing (van der Wiel & Shipman 2008). Preliminary analysis show that many objects that are spatially correlated with the dark filaments have mid-IR colours typical for Young Stellar Objects.

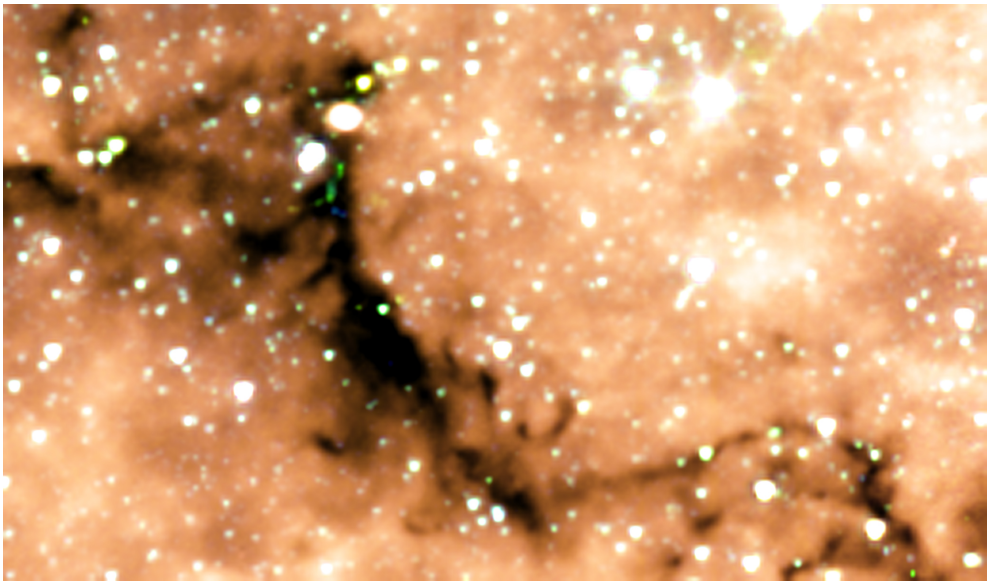

Figure 2.2: This figure shows a false-colour image of the region toward IRDC G48. The bright emission is coming from the W51 complex in the background, at about twice the distance of the IRDC. The displayed emission is from the four IRAC channels, i.e., 3.6 μm (blue), 4.5 μm (green), 5.8 μm (yellow) and 8 μm (red).

2.3 IRDCs in a Galactic context

Infrared Dark Clouds may play a key role in star formation in the Galaxy. The general picture that arises from detailed studies on a handful of objects suggests that IRDCs are in a very early stage of clustered star formation. That is, they constitute the filamentary structures and massive dense clumps in molecular clouds, described as the first stage of massive star formation in Chapter 1, Section 1.1.4. However, the more evolved stages such as cold collapsing cores, hot cores and HII-regions may well be associated with some IRDCs as well.

In that respect, IRDCs may not be too different from probably the best-studied (massive) star forming region in our Galaxy, the Orion Molecular Cloud (OMCI). The OMCI is not observed in mid-IR absorption because it is located outside of the Galactic Plane, where there is no bright background. The filamentary dust continuum emission observed toward the OMCI, however, is strikingly similar to what is seen for many IRDCs, both in structure and dimension (Menten et al. 2005). A noticeable difference, though, is the presence of the very active high-mass star forming region BN/KL in Orion, coinciding with the location of the maximum dust emission. Up to now, such evolved stages of massive star formation have not been observed in IRDCs and concur that they are at an even younger stage of clustered star formation.

Given the fact that IRDCs appear to be ubiquitously present, at least in the Inner Galaxy, it may well be that most of the stars in our Galaxy originated in massive cluster forming clouds. An essential step forward in testing such an idea is to get a complete picture of the distribution of massive dark clouds throughout the Galaxy.

2.3.1 IRDCs and the Outer Galaxy

The spatial distribution of IRDCs, as described in Section 2.1.2, is clearly biased by the fact that identification through mid-IR absorption requires a bright mid-IR background. Because the diffuse emission in the Outer Galaxy is much weaker, IRDCs have not been identified by the traditional method beyond the Solar circle (~ 8.5 kpc). It is well-known that the more evolved, active stages of clustered star formation are present in the Outer Galaxy, e.g., NGC 7538, W3-4-5. Based on their existence, it is expected that the earliest stages are also present out to large distances from the Galactic centre. It will, however, require a different technique of identification to find them. The rest of this dissertation revolves around this question:

Can we identify Infrared Dark Clouds in the Outer Galaxy?

Chapter 3

Towards an identification of Outer Galaxy dark clouds

– I – The identification of near-IR extended red objects

W. W. F. Frieswijk & R. F. Shipman*

ABSTRACT

DARK CLOUDS represent the earliest stages of star formation in the Galaxy. Nearby dark clouds have been studied in great detail and they provide a wealth of information on the low-mass isolated star formation process. In the mid 1990s, infrared surveys (ISO, MSX) have revealed a class of massive dark clouds, called the Infrared Dark Clouds, out to large distances (> 1 kpc). The Galactic distribution and the ambient conditions of these dark cloud complexes are of great importance to our understanding of the clustered mode of star formation. However, up to now they have been identified only toward the inner parts of the Galaxy.

This chapter introduces a statistical method that is the foundation of our identification of dark clouds in the Outer Galactic Plane. We apply the Mann-Whitney U-test on near-IR data from the Two Micron All Sky Survey to identify star colour distributions that are significantly redder ($\gtrsim 99\%$ confidence) compared to their local environment. The method is applied to two different resolutions, i.e., $60''$and $90''$, to account for the decrease in star counts toward the Galactic anti-centre. By means of a cluster finding algorithm (friends-of-friends) we produce a catalogue of red extended objects. We identify 1320 objects with the high resolution grid and 1589 with the low resolution grid. We cross-correlate the catalogue with existing infrared data (MSX and IRAS) and optically identified dark clouds.

We suggest that the catalogue presented in this chapter contains, besides other objects, also massive dark clouds that were previously unnoticed. However, follow-up analysis is required to confirm this proposition (see next chapters).

*To be submitted to Astronomy & Astrophysics

3.1 Introduction

The outer Galactic plane is defined as the part of our Galaxy beyond the Solar circle, i.e., $R_{\rm gal} > 8.5$ kpc. Most of the Outer Galaxy appears quiescent and is often undervalued in studies of star formation with respect to the Inner Galaxy. Prominent star forming regions obviously exist in the Outer Galaxy. These include well studied nearby (< 500 pc) regions such as the Orion and Taurus-Perseus-Auriga complexes and more distant ($\gtrsim 2$ kpc) active regions such as W3 and NGC 7538. But, the majority of the star-forming activity in the Galaxy is located toward the inner spiral arms and the molecular ring ($4 < R_{\rm gal} < 8$ kpc).

However, this contrast between the Inner and Outer Galaxy makes the outer parts so interesting. To understand key topics in star formation, such as the origin of the stellar mass distribution (or initial mass function; IMF) and the starting conditions for clustered (massive) star formation, it is essential to consider the effects of external conditions on the process that initiates stellar birth. The Outer Galaxy is the only nearby region where we can study an environment where properties such as metallicity, pressure and radiation field are different compared to the inner parts (Brand & Wouterloot 1995; Rudolph et al. 2006).

The study of the early stages of star formation in different environments throughout the Galaxy requires large scale surveys to identify a statistically valuable sample of star-forming regions at various stages.

– Large scale surveys: Emission –
A number of surveys are available to the community. We mention the following data sets in particular, because we use them later on: the Midcourse Space Experiment (MSX, mid-IR); the Infrared Astronomical Satellite (IRAS, mid- to far-IR); and the Five Colleges Radio Astronomy Observatory (FCRAO) CO surveys. There exist many regions that have been studied in detail (see PPV, Reipurth et al. 2007, for a recent overview) that were first observed through these large surveys. However, depending on the data, there is a clear bias towards the evolutionary stage of the objects that are identified. For example, in case of mid-infrared continuum emission, e.g., MSX or IRAS, the observed dust is sufficiently heated by embedded objects. This suggests a relatively advanced stage of star formation. On the other hand, CO surveys detect mostly the molecular gas on large spatial scales. Not only because of the low spatial resolution ($\sim 1'$), but also, because CO is optically thick under general interstellar medium conditions. The consequence is, that CO surveys are powerful in detecting the presence of molecular material, but the dense clumps and cores are not easily identified, if at all.

– Large scale surveys: Absorption –
The nearby, cold and dense stages of star formation are without difficulty detected in absorption at optical (e.g., Digitised Sky Survey I) and infrared wavelengths (e.g., 2MASS). Well-known examples are the Bok globules and nearby dark clouds observed through star counts and extinction measurements. At larger distances, there are the recently discovered Infrared Dark Clouds (IRDCs). These are observed in silhouette against the diffuse mid-IR background of the Inner Galaxy (MSX and ISO;

Egan et al. 1998; Pérault et al. 1996, respectively). Recent studies show that IRDCs are often associated with massive star and cluster formation (e.g., Rathborne et al. 2006, 2005; Ormel et al. 2005).

– Massive dark clouds in the Outer Galaxy –
The mid-IR extinction that is observed toward IRDCs (1 –2 mag at 8 μm; Carey et al. 2000) implies that they have column densities well in excess of 10^{22} cm^{-2}. Given their low temperatures (< 30 K), IRDCs are particularly bright at (sub)-millimetre wavelengths due to cold dust emission. Hence, dust continuum observations provide a good tool to identify IRDCs. Unfortunately, data from large scale (sub-)millimetre surveys are not available at present. Dust continuum studies are usually performed on well-selected objects. This is subject to change in the near future with the rapid developments in (sub-)millimetre instrumentation over the last years.

The diffuse mid-IR background emission in the Outer Galaxy is too faint to identify dark clouds in absorption with, e.g., MSX. Up to now, no IRDC-like objects have been identified in regions toward the Outer Galaxy. That raises a question:

Do IRDC-like objects exist in the Outer Galaxy?

Intuitively, the answer is yes, because it is well-known that more evolved stages of massive, clustered star formation are present, e.g., W3 and NGC 7538. The question then becomes:

How can we identify the early stages with data that is available at present?

In this chapter, we present a statistical analysis of the near-IR colour distribution of stars from the Two Micron All Sky Survey (2MASS) towards the Outer Galactic Plane. The 2MASS data are useful for our purposes, because the entire sky is uniformly covered, and near-IR data are less sensitive to extinction due to dust compared to optical data. 2MASS probes the stellar content throughout the Outer Galactic Plane. We produce a catalogue of extended, red, near-IR objects and argue that, besides many known objects, this list contains previously unidentified dark cloud regions in the Outer Galaxy.

Various independent studies are closely related to this work. Dobashi et al. (2005) identified a large number of dark clouds in the Galactic Plane, including the Outer Galaxy, by applying star counts. We use their catalogue to confirm the presence of known dark clouds in the list of objects we identify. A notable difference in their work is that they use optical data. Optical data are more sensitive to the lower extinction regions. They are preferentially identifying low-mass dark clouds that are located nearby, mostly within a few kpc. Star counts have been applied to the 2MASS data by Froebrich et al. (2005). They determine the relative extinction in the Galactic Plane. However, the star count method is limited, because it requires a high level of completeness of the data. That implies the use of a magnitude limited data set in order to justify a correlation with extinction.

In addition to star counts, the Near Infrared Colour Excess (NICE, Lada et al. 1994) method is widely used to determine extinction toward nearby dark clouds (< 1 kpc; e.g., Alves et al. 1998; Lada et al. 1999; Cambrésy et al. 2002). However, the

NICE approach cannot be used uniformly toward the entire Outer Galactic Plane for a number of reasons:

- The extinction law is not uniform in every direction. In particular, deviations have been observed toward dense clouds (e.g., Strafella et al. 2001; Kandori et al. 2003). This is usually attributed to a change in dust properties, e.g., the size distribution of grains (e.g., Mathis 1990; Ossenkopf & Henning 1994);

- An average reference colour of the background stars is required. This is normally adopted from a nearby, extinction-free region;

- The presence of foreground stars reduces the measured colour excess. This becomes particularly significant when an object is located at a large distance and the fraction of foreground stars increases.

Considering the above mentioned possibilities and limitations, ideally, we require an identification method for dark clouds in the Outer Galaxy based on 2MASS that incorporates the following:

- It determines the amount of extinction from the near-IR colours of stars.

- It can be applied to small numbers of stars in order to process at high spatial resolution.

- It can be treated uniformly in all directions.

- It determines a reliability of the measurements.

- It is independent of foreground stars that are present.

We approach the problem, by applying a distribution-free statistical method, i.e., the Mann-Whitney U-test (Sec. 3.3), in combination with a friends-of-friends cluster finding approach (Sec. 3.4). in order to produce a catalogue of near-IR extended red regions in the Outer Galactic plane. This approach can be used uniformly throughout the Galaxy. It does not assume uniform dust properties. It does not require a uniform off-field position. It is not required to make a correction for foreground stars and it returns a reliability of the regions we find. The one thing that we cannot accomplish from the list above, is a determination of the amount of extinction.

An implication of the method is that, a priori, we cannot know what the nature of the identified objects is. We provide an initial analysis by performing a cross-identification of the catalogue with existing data, i.e., the IRAS and MSX point source catalogues and the dark cloud catalogue published by Dobashi et al. (2005).

The chapter is organised as follows: Section 3.2 introduces the 2MASS data. Section 3.3 describes how we apply the U-test and we discuss its strengths and limitations. Section 3.4 describes how we use a friends-of-friends approach to identify clustered red regions. Section 3.5 presents the catalogue, which will be made available online, and the results of the cross-identification. Section 3.6 ends with a discussion and summarises the result of the same method applied to Inner Galaxy IRDC G48.

3.2 Data: the Two Micron All Sky Survey

The Two Micron All Sky Survey (2MASS) scanned the entire sky uniformly in three near-IR bands: J (1.25 μm), H (1.65 μm) and K_S (2.17 μm). The 2MASS Point Source Catalog (2MASS PSC, Skrutskie et al. 2006) consists of accurate positions and brightness information for over 400 million stars. The point source catalogue is $>99\,\%$ complete up to $J<15.8$, $H<15.1$ and $K_S<14.3$ magnitudes. The photometrical signal-to-noise ratio is >10 (i.e. $\sigma_{J,H,K_s} \lesssim 0.1$ mag) for sources brighter than the above stated completeness limits. The fainter sources, hereafter referred to as the faint extension of the point source catalogue, have errors increasing up to $\sigma_{J,H,K_s} \sim 0.4$ mag. We decide to make use of all available sources in 2MASS, including the faint extension. This increases the total amount of objects by almost a factor 2 compared to star count studies, where the faint extension cannot be used because the data are incomplete.

We emphasise that the $H-K_S$ colour is an appropriate choice to perform the identification of red regions because the intrinsic $H-K_S$ colour of stars spans only a narrow range. For spectral types A0V to M6III the range is about 0.00 to 0.30 mag (Bessell & Brett 1988; Wainscoat et al. 1992). In the Solar neighbourhood the average $H-K_S$ colour is about 0.13 mag with a standard deviation of 0.1 mag. This assumes no reddening due to extinction and takes into account the sensitivity limit of 2MASS (14.3 mag for K_s-band). Including the faint extension, the average $H-K_S$ colour increases slightly (0.15 mag) due to faint, intrinsically redder M-dwarfs. If a region appears significantly redder, this suggests that either foreground extinction is present or the intrinsic colour distribution of stars in that direction is different.

We analyse the 2MASS data in the Outer Galaxy from l=90° to 270° and b=-3.5° to +3.5°. In order to process the data, without too much effort, on a desktop computer, the area is divided up in regions of two by two degrees, with a sampling separation between different fields of one degree.

3.3 Identification of red regions: the Mann-Whitney U-test

The Mann-Whitney U-test (also called the Wilcoxon rank-sum test, hereafter referred to as U-test) is a well-known non-parametric significance test that evaluates whether two samples of observations come from the same parent distribution. It was first proposed for equal sample sizes by Wilcoxon (1945) and extended to arbitrary sample sizes by Mann and Whitney (1947). In this Section we explain how we apply the U-test in order to calculate the probability that the colour distribution of stars along a line of sight is different, i.e., redder, compared to the parent distribution.

The great benefit of the non-parametric test is that whatever size the two samples have, the distribution of the U-test statistics is known. Tables of the critical values for the U-test usually do not contain samples with size in excess of 20. However, according to the central limit theorem, the distribution will approach a *normal* distribution for large sample sizes. The mean of the variables is then given by the mean of the *normal* distribution. Moses (1964) states that the *normal* approximation can be applied to the U-test if the smallest sample contains 5 or more sources.

We evaluate this result in a Monte Carlo simulation in which we simulate the distribution of the z-values, where z is the deviation of the mean in multiples of the standard deviation. The simulation shows that, for random drawn samples from a large distribution, the z-distribution is indeed approximately given by a Gaussian probability density function. The results of simulations of samples of 5 and 8 sources are displayed in the left panels of Figure 3.1, corresponding to the upper and lower histogram, respectively.

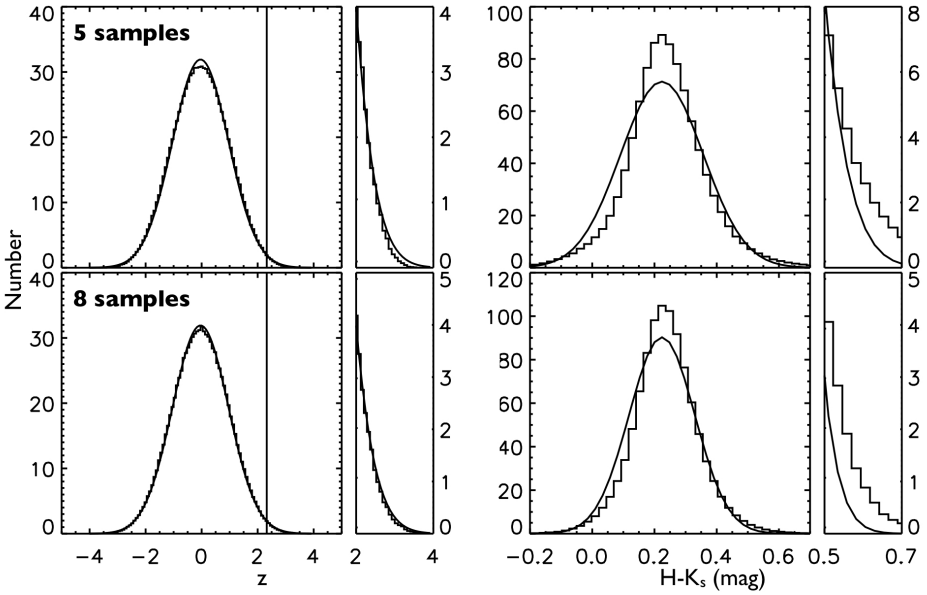

Figure 3.1: Visualisation of the results of a Monte Carlo simulation, where we randomly draw 1000 samples of 5 (upper histograms) and 8 (lower histograms) 2MASS colours from a test field at l=122°, b=1°. The distributions of the significance values z are displayed on the left and those of the average $H - K_S$ colours on the right. The solid curves represent Gaussian density functions with the peak position and variance determined from the simulated distribution.

At the peak position, as well as in the the wings, the Gaussian profile overestimates the simulation for samples of 5 sources. The example of 8 sources shows that the simulation converges fast to a *normal* distribution. This discrepancy is not due to normalisation, i.e., both distributions are normalised. Hence, the simulation has a

slightly broader (larger FWHM) profile than the *normal* distribution. However, the disagreement is less than 10% ($<5\%$ for 8 samples) in the area of the wing ($z>2$) and works in our favour. If we assume the profile is given by a Gaussian distribution, we underestimate the actual probability in the regime considered in this work, i.e., $\geq$99%.

In order to compare the results of the U-test with a parametric test, we simulate the distribution of average colours from random drawn samples. The results are, again for 5 and 8 samples, displayed in the right panels of Figure 3.1.

It should be clear from these figures that the average colour distribution converges much slower to a Gaussian profile. Moreover, we underestimate the area in the wings ($H-K_S>0.5$ mag) by $\sim$50% ($\sim$100% for 8 samples) and the simulated profile is skewed. The assumption that the distribution of colours is known is not applicable. Our simulations indicate that for large sample sizes (30) the distribution does approaches a *normal* profile for the peak and FWHM, but the fit to the wings becomes even worse.

We have intentionally decided to use a non-parametric test to avoid assumptions on the shape of colour distributions. Furthermore, the U-test in particular is less sensitive to variations in the tails of a distribution, not only compared to the average colour, but also to other non-parametric tests such as the Kolmogorov Smirnoff test.

U-test Procedure
The following steps are involved in the calculation of the probability P for each grid-cell in the predefined grids described in Section 3.3.2: (from Wall & Jenkins 2003)

a) Let A be the distribution of colours in the grid-cell, with m the number of members. Let B be the reference distribution, with n members, where n is very large in this study. The null-hypothesis (H_0) is that A and B have the same parent population. Or, in the context of this study, that the parent population of A is given by B. Note that when m is less than 5, we set the probability P to 50% and continue processing the next cell.

b) Rank the colours in ascending order for the combined members (i.e., $m+n$) of A and B. Preserve the information on the A or B identity for each member.

c) Sum the number of A-rankings to get the U-test statistic U_A. When applying the U-test, it is custom that tied observations are assigned with the average of the tied ranks. However, we avoid tied observations by adding very small random number to the colour values (i.e., $\sim 10^{-4}$, which is less than the precision of the data). The impact of this assumption is that we underestimate the probability determined below, i.e., we are being conservative.

As discussed earlier, the sampling distribution tends to a *normal* distribution (Figure 3.1). The mean and variance are given by

$$\mu_A = m(N+1)/2 \quad \text{and} \quad \sigma_A^2 = mn(N+1)/12\,, \tag{3.1}$$

respectively, where $N = m + n$. The significance can be assessed from a *normal* distribution by calculating

$$z = \frac{U_A - 0.5 - \mu_A}{\sigma_A}\,. \tag{3.2}$$

Here, we use a value of -0.5 (instead of +0.5) because we consider only objects in the upper tail, i.e., where the distribution is redder compared to the reference distribution. The probability is calculated using the Gaussian probability density function.

We put effort in producing a list of objects with a high reliability and reject the null-hypothesis at a 99% significance level. That implies that cells with a probability P=99% or higher are considered in the next step, which is the identification of clustered cells using a friends-of-friends approach (Sec. 3.4).

3.3.1 Reference distribution

We cannot use a single, uniform reference distribution toward different directions in the Galactic Plane. To account for the intrinsically variable colour distribution in each direction, we choose to determine a local, i.e., in projection on the sky, reference distribution for each field. The colour distribution of the few stars in a grid-cell is compared to the colour distribution of all other stars in the 2×2 square degree surrounding field. We assume that the stars we observe in a field reflect the proper distribution of colours in that direction.

3.3.2 Limitation of the U-test: resolution

The limiting factor for the spatial resolution that can be achieved in performing the U-test is determined by the minimum of 5 sources required. We use a rectilinear grid to calculate the statistics on. As a requirement for the grid resolution we state that in every field at least 75% of the cells contain 5 or more sources. Because the stellar surface density decreases toward the Galactic anti-centre (l=180°), we process the data at two different resolutions. The highest possible resolution towards the spiral arm regions at $l \sim 90°$–$140°$ and $l \sim 240°$–$270°$ is 60″. For the region between $l \sim 140°$–$240°$ we require a grid with cells of 90″. Note that we process the entire Galactic Plane at both resolutions and put the objects in the final catalogue. The average number of stars per cell is for both resolutions about 8, considering the regions specified above.

3.3.3 Reliability

A number of uncertainties need to be considered when interpreting the cells that are selected by rejection of the U-test method. These are related to the reliability, discussed below, and completeness, discussed in Section 3.3.4, of the cells that are identified as red.

Type I error
The first error is related to the reliability, or the significance level of the selected cells. It is defined at 99%, which suggests that 1% of the cells can be selected due to statistical uncertainty, rather than being truly redder. However, these cells are expected to be randomly distributed over the fields. We can show that this is indeed the case. Consider the following values adopted from the low-resolution 2 by 2 degree field toward l=166°, b=1°. This field is assumed to be devoid of extended red structures, because no clusters of red cells ended up in the final catalogue. However, in the field there are 76 cells out of a total of 6561 where the null-hypothesis of the U-test was rejected. This accounts for $\approx$ 1% and indeed, these cells are spread randomly over the field (no clusters have been identified). Moreover, if we define a reliability of 95%, we identify about 5% of the cells (374 out of 6561) randomly spread across the field. Again, this is consistent with the statistically expected value.

3.3.4 Completeness

Type II error
This error is related to the cells that are not identified, i.e., where the null-hypothesis is not rejected, where it should have been. It is very difficult to put a realistic value to this error. In a broad sense it is inversely related to the Type I error. That is, the more reliable the sample is the less complete it is and vice versa. Furthermore, the Type II error usually occurs when sample sizes are too small. Because we have chosen to produce a high reliability catalogue, we are giving in on completeness due to this error.

Sample statistics
We have selected a resolution so that at most 25% of the cells in a field contain fewer than 5 sources. We cannot trust the probability calculated for these cells. They are omitted in the further identification process and therefore introduce another form of incompleteness.

Considering the limitation and reliability of the method, we have decided to put the effort in producing a reliable target list, rather than being complete. We have given up on completeness in order to process the data at the highest possible resolution. Furthermore, our intention is not to evaluate the content or structure of the Outer Galactic Plane nor finding all dark clouds present in the Outer Galaxy. We simply present a statistical method that enables the identification of real objects.

3.4 Clustering of red regions: a friends-of-friends approach

To increase the reliability of the final list of objects and to avoid the selection of random cells, we add an additional step in the identification process. We allow only clusters of 4 or more red cells in the catalogue.

An extensively used cluster finding technique in cosmology is the percolation or friends-of-friends algorithm, first applied by (Huchra & Geller 1982). The basic algorithm, applied to Galaxy redshift surveys, uses three parameters to identify groups

of objects; two specify the position (e.g., RA and Dec) and one the distance (e.g., spectroscopic redshift). This technique can be simplified to find groups, or structures in projection on the sky, by omitting the redshift parameter. We use a similar approach to identify groups of regions on the sky where the colour distribution of stars is red compared to the local surroundings, i.e., where the U-test returns a probability of P= 99% or higher.

Linking length
A crucial parameter required for the friends-of-friend method is the linking length, L, used to determine whether selected cells belong to the same group or not. If L is taken too large, all cells will be assigned to the same group. If L is too small all cells will be isolated. Because we do not know the cause of the red distribution in different cells (either extinction due to a foreground cloud at unknown distance, or a concentration of intrinsically red objects at unknown distance) it is impossible without further information to put a physical size to L. We therefore choose a linking length in terms of the cell size, $s_{\rm cell}$.

An upper limit can be estimated from an empty field. Consistent with the defined reliability, about 1% of the cells in an empty field are rejected by the U-test and spread randomly over the field. We assess an average distance between rejected cells by using a Monte Carlo simulation, where n cells (=1% of a^2) are selected at random locations from a square box with side a. For a^2 we use the number of cells that make up a 2 by 2 square degree field at the given resolutions, i.e., a=81 cells at 90″ and a=121 cells at 60″ resolution. The average distance in the simulation converges to 5.3 and 5.2 times the cell-size, $s_{\rm cell}$, respectively. This is in agreement with the theoretically expected value, given by

$$\text{average distance} = \frac{1}{2}\sqrt{\frac{a \times a}{n}} = 5 \quad [\times\ s_{\rm cell}] \tag{3.3}$$

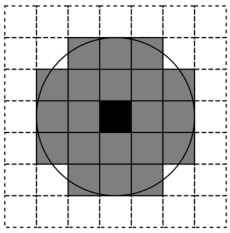

Figure 3.2: Interpretation of the linking length L.

A linking length larger than this average distance will group cells together even if the distribution is random. This obviously contradicts the goal of finding clustered regions. A lower limit is obviously the cell size itself. We have tested the method by varying L between 2 and 4. The higher values (>3) identify mostly large scale structures ($>0.5^\circ$). For a value of 2, many cells are isolated or grouped with fewer than 3 other cells. We decide to use a linking length half that of the average distance between random points, i.e., L=2.5 times the cell size, for both resolutions. The probability for finding 'groups of 4 cells' with L=2.5, considering 1% of the cells are randomly selected by the U-test, is $\sim$0.1% Figure 3.2 shows a graphical representation of the linking length. The centres of the grey cells fall within

distance L of the black cell, indicated by the circle. These are assigned as friends of the central cell.

Friends-of-friends procedure
The friends-of-friends routine runs on all grid-cells selected by the U-test and includes the following steps:

a) Select a cell that has not been assigned to a group and is not considered isolated.

b) Find all friends of this cell, i.e., all other cells to which the distance from centre to centre is less than the linking length L. If there are no friends, the cell is considered isolated and the procedure returns to *a*, else it continues.

c) All friends make up the initial list of group members. The surroundings of all members are inspected for new friends and these are added to the list. This process is repeated until no further friends are found.

d) The output is a list of all members of the current group. If the group contains 4 or more members, it is labelled as an extended red object, else the cells are discarded as being isolated. The procedure returns to *a* as long as there are unassigned cells.

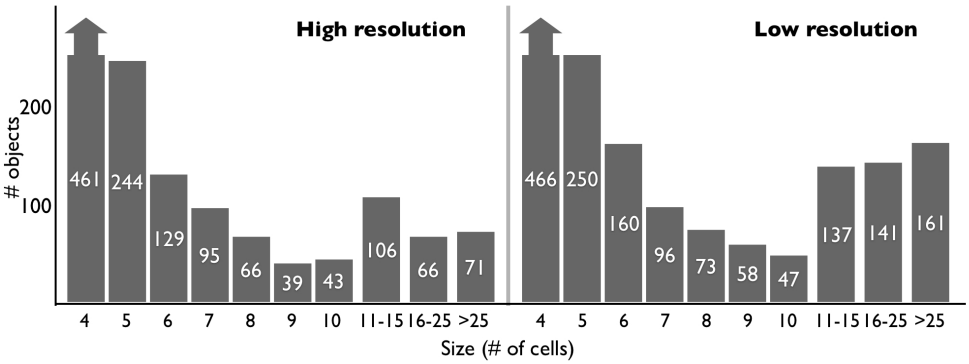

Figure 3.3: This figure gives an overview of the number of objects extracted by the friend-of-friends method as a function of the number of cells the object consists of. The values inside the diagram give the exact number of objects for each column.

Saved parameters
The location of each object is determined by the average coordinates of individual cell members and given in Galactic coordinates l (°) and b (°). The size is defined as

the extent of an object in the probability image in longitude and latitude direction, given as Δl ($'$) and Δb ($'$), respectively. For every object we keep track of the number of cells that it consists of. In addition, we count the total number of 2MASS sources that are contained within these cells. Figure 3.3 shows schematically the number of objects extracted by the friends-of-friends method as a function of size.

3.5 Results

3.5.1 Spatial distribution

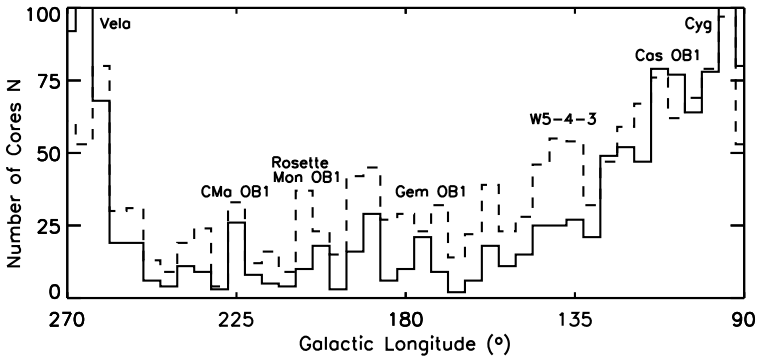

Figure 3.4: These histograms show the spatial distribution in Galactic longitude of the extended red objects identified in this work. The solid and dashed lines represent the distribution of high-resolution and low-resolution objects, respectively. A few well-known regions in the Outer Galactic Plane are given as a reference.

Figure 3.4 displays the spatial distribution of the objects identified in the Outer Galaxy. Some well-known regions associated with molecular clouds and star forming activity in the Outer Galaxy are indicated by name. Most objects we find are well confined within the large scale extent of these complexes. The majority of objects ($\sim$40%) in the high-resolution list, given by the solid line, are located towards the crowded spiral arm regions near *Cygnus* l=90°–100° and *Vela* l=260°–270°. Part of this is probably explained by the fact that more than 25% of the high-resolution grid towards the low stellar density regions consists of cells that have fewer than 5 sources. These cells cannot be used in the identification process. The low-resolution objects are given by the dashed line and are more evenly spread out.

3.5.2 Associations

How can we be confident that the objects that we identify are real?
We establish the first step by cross-correlating the catalogue with existing data, i.e., the IRAS and MSX point source catalogues and the optical dark cloud catalogue by Dobashi et al. (2005). We define an object associated with any of the sources in these catalogues in the following way:

MSX – The spatial resolution of MSX is high enough ($\sim 18''$) to consider sources associated whenever they fall within the boundary of any one of the red cells that the object consists of.

IRAS – For the IRAS sources we adopt a positional uncertainty of $\sim 2.5'$ based on the uncertainty in the 100 μm observations. The actual uncertainty may be much better, certainly if the shorter wavelengths are detected. However, we have decided to process the catalogue with a consistent value, whereas the error in IRAS positions varies from source to source and also depends on the scanning direction during the observations (ellipsoid uncertainty).

Optical – We use the catalogue presented by Dobashi et al. (2005) to match our objects with previously identified dark clouds. Their catalogue is based on optical star count measurements performed on Palomar sky plates and covers the entire Galactic Plane. We define an object in our catalogue associated with an optical dark cloud when any of the cells of an object fall within the area of a dark cloud. This area is adopted from the linear dimension given by Dobashi et al. (2005) at their observed position. Note that because of differences in both data and method, as well as the large projected area of some objects in both catalogues, it occurs that multiple objects in our list are associated to one optical dark cloud, and visa versa.

What can we learn about the nature of the objects in the catalogue, given the information we have from this study?
Below we list a number of characteristics that can help give an interpretation to the way objects are identified in this work. Note, however, that we do not intent to give a complete overview and rule out other possible interpretations. Many of the objects in the catalogue have multiple associated sources, in any combination with the correlation data. This may lead to different interpretations for individual objects.

- The presence of very red 2MASS sources indicates either a clustering of intrinsically red sources, e.g., embedded young stellar objects or AGB-stars, or the presence of foreground extinction. We identify variations in colour distributions locally in projection on the sky. Therefore, we can safely assume that foreground material is in the form of clouds rather than an entire line of sight. In case of the latter, we would expect the reddening not to be confined to spatial scales of the order of arc-minutes.

- The association with mid-IR point sources, e.g., MSX 8 μm, IRAS 12 μm and 25 μm, can be an indication of the presence of embedded young stellar objects. These objects can be the same red sources that are observed in the 2MASS data. The presence of a molecular cloud can additionally be responsible for reddening of background stars.

- The far-IR IRAS 60 μm and 100 μm association can be an indication of the

presence of very young and cold proto-stellar cores. These are likely not visible in the 2MASS data. The molecular cloud may, however, cause reddening of background stars and embedded objects may be present as well.

- The association with an optical dark cloud indicates that we are identifying the same cloud, or part of the cloud, in near-infrared extinction. This does not mean that all red sources in 2MASS are behind the cloud. Some may well be embedded young stars.

- We cannot rule out a confusion with extra-galactic sources. Distant galaxies can be part of the 2MASS catalogue and may appear similar in colour as reddened stars. These galaxies can also be present in the MSX and IRAS data.

3.5.3 The Catalogue of Near-IR Extended Red Objects

	High resolution	Low resolution
Total	1320	1589
No associations	369	434
MSX	298 (22)	428 (32)
IRAS		
12&25 μm	596 (67)	714 (66)
60&100 μm	591 (81)	786 (130)
Optical[a]	494 (194)	594 (188)

Table 3.1: Overview of the high- and low-resolution catalogue of extended red objects derived from 2MASS using the U-test method combined with a friends-of-friends approach. The values give the number of objects that have an associated source in the data listed in the first Column. The numbers between brackets indicate how many of these objects have an association with the respective catalogue but no association with the other catalogues.

[a] (Dobashi et al. 2005)

Table 3.1 summarises the content of the high- and low-resolution catalogue of extended red objects. The complete catalogues, including probability images in *FITS*-format, are available on request from *W. Frieswijk*. Table 3.2 presents an excerpt of the high resolution catalogue of red extended objects. The objects correspond to those that are located in the field centred on l=112°, b=1° (see Figure 3.5). The different columns give the following information:

Column (1): Identification number of the objects.
Column (2)–(3): Galactic coordinates of the centre of the object.
Column (4): Total number of cells that an object consists of.
Column (5): Extent in Galactic longitude of the object in arcminutes.
Column (6): Extent in Galactic latitude of the object in arcminutes.

Column (7): Total number of 2MASS sources associated with the object.
Column (8): Total number of MSX 8 μm sources associated within the boundaries of the object.
Column (9)–(12): Total number of IRAS sources associated with the object for 12, 25, 60 and 100 μm, respectively.
Column (13): Indication of the presence of an optical dark cloud (Dobashi et al. 2005), i.e., Y(es) or N(o).

ID	l	b	N_{cell}	Δl	Δb	IR Point Sources						DC
(1)	(2)	(3)	(4)	(5)	(6)	(7)	(8)	(9)	(10)	(11)	(12)	(13)
	deg	deg		pix	pix	2M	8	12	25	60	100	
456	111.09	1.45	5	5	4	43	0	0	0	0	0	Y
458	111.19	1.37	5	3	6	49	0	0	0	0	0	N
462	111.39	1.92	5	3	3	38	0	1	1	0	0	N
463	111.55	0.77	40	17	9	655	15	8	3	2	0	N
464	111.47	1.00	16	9	8	122	0	0	0	0	0	Y
465	111.46	1.75	9	7	8	67	0	0	0	0	1	N
466	111.46	1.97	4	4	3	29	0	0	0	0	0	N
468	111.51	1.89	10	7	6	70	0	0	0	0	0	N
469	111.58	1.77	13	12	6	80	0	0	1	0	0	N
470	111.61	0.37	8	5	4	123	4	1	1	1	1	N
472	111.64	0.90	4	4	5	32	0	1	2	1	1	N
473	111.72	-0.01	8	6	7	84	0	1	1	1	1	Y
474	111.76	0.72	34	12	20	335	3	1	5	1	0	N
475	111.83	0.46	20	11	8	162	1	2	2	0	1	Y
476	111.85	1.67	16	11	10	122	0	0	1	1	0	Y
477	111.82	0.36	5	4	5	46	0	0	0	0	0	N
478	111.95	0.87	52	20	18	468	6	4	7	3	2	Y
479	111.97	1.10	4	5	3	31	0	1	1	1	0	Y
480	112.03	1.52	5	4	4	53	0	0	0	0	0	N
481	112.05	1.71	4	3	4	29	0	0	0	0	0	N
482	112.07	0.94	4	3	6	34	0	0	0	0	0	Y
483	112.14	1.43	4	4	2	41	0	1	1	0	0	N
484	112.23	1.60	11	8	8	101	0	0	0	0	0	N
486	112.43	1.54	15	15	7	109	0	1	1	0	1	Y

Table 3.2: Excerpt of the high resolution catalogue of extended red objects in the Outer Galactic Plane. The column descriptions are given in the text. The listed objects are located near NGC 7538 and displayed in Figure 3.5

The left panel in Figure 3.5 displays the probability image returned by the U-test method for the field towards NGC 7538, i.e., l=112°, b=1°. The extended red objects that are identified by the friends-of-friends method are given various colours. The extent of the objects is represented by the black ellipses, where the minor and major axis are given by the size of an object listed in Column 5 and 6 of Table 3.2. The black cells are selected by the U-test, but are not part of a group as defined by the friends-of-friends method. They are considered isolated. The right panel in Figure

3.5 displays the same region at 8 μm as observed by MSX. We discuss some of the prominent objects present in this region.

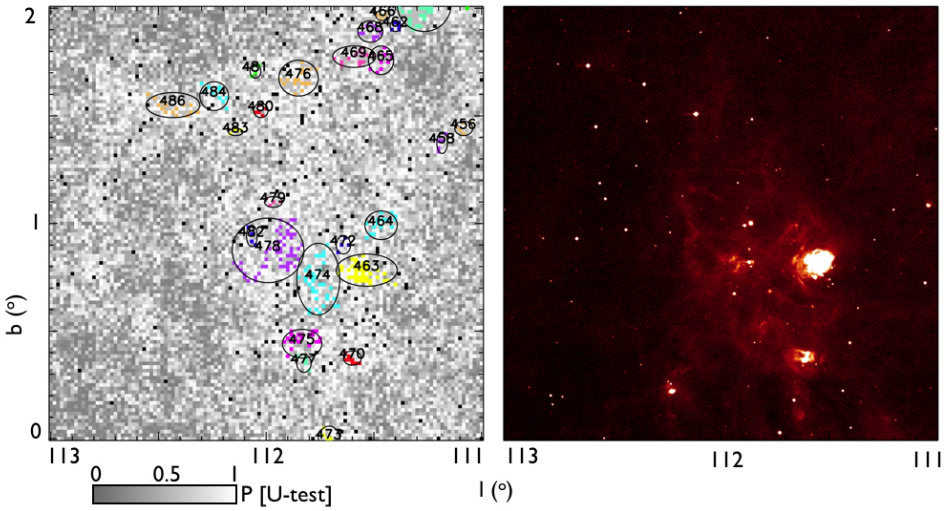

Figure 3.5: The left image displays the probability image returned by the U-test. The grey-scales represent the probability that the colour distribution in the cells are redder with respect to the reference distribution. The friends-of-friends method identified the extended red objects given in arbitrary colours. The black ellipses give the extent of the objects (see Section 3.4). Black cells are identified as being red, but are considered isolated. Objects 463 and 470 correspond to NGC 7538 and S159, respectively. Object 474 is a candidate Outer Galaxy massive dark cloud, identified as such by the method presented in this thesis. The right image shows the region in MSX 8 μm emission. Bright emission from warm dust, heated by embedded, massive young stars, is seen toward both NGC 7538 and S159. The upper part is devoid of extended 8 μm. Some of the objects there do have an association with infrared point sources and optical dark clouds.

Objects 463 and 470 corresponds to the well-studied massive star forming regions NGC 7538 and S159, respectively. They are both located at a distance of about 3 kpc from us in the Perseus spiral arm (van der Tak et al. 2000; Brand & Blitz 1993, respectively). We identify them because of the presence of numerous embedded objects, which are observed as clusters of red sources in the 2MASS data. The objects are both bright at 8 μm emission. This confirms that the method will not only identify extinction in dark clouds, but also at later, active stages of star formation.

Object 474 is the best studied massive dark cloud candidate in the Outer Galaxy up to date. Only very faint 8 μm emission is observed and a number of infrared sources are associated with the object. A detailed analysis of this complex is presented in Chapters 5 and 6.

Object 478 is associated with a number of infrared sources and an optical dark cloud. A SIMBAD search reveals that there are multiple radio sources and masers observed in this area.

The objects located in the upper part ($b > 1.5°$) have no 8 μm extended emission associated. Several of them do have infrared point sources and optical dark clouds associated. We suspect that this region corresponds to nearby dark clouds with some low-mass star forming activity present. This is confirmed by a SIMBAD search that returns multiple Lynds dark clouds (Lynds 1962) in this region (similar to the Dobashi 2005 catalogue).

3.6 Discussion and conclusions

3.6.1 Can we identify IRDC-like objects with this method?

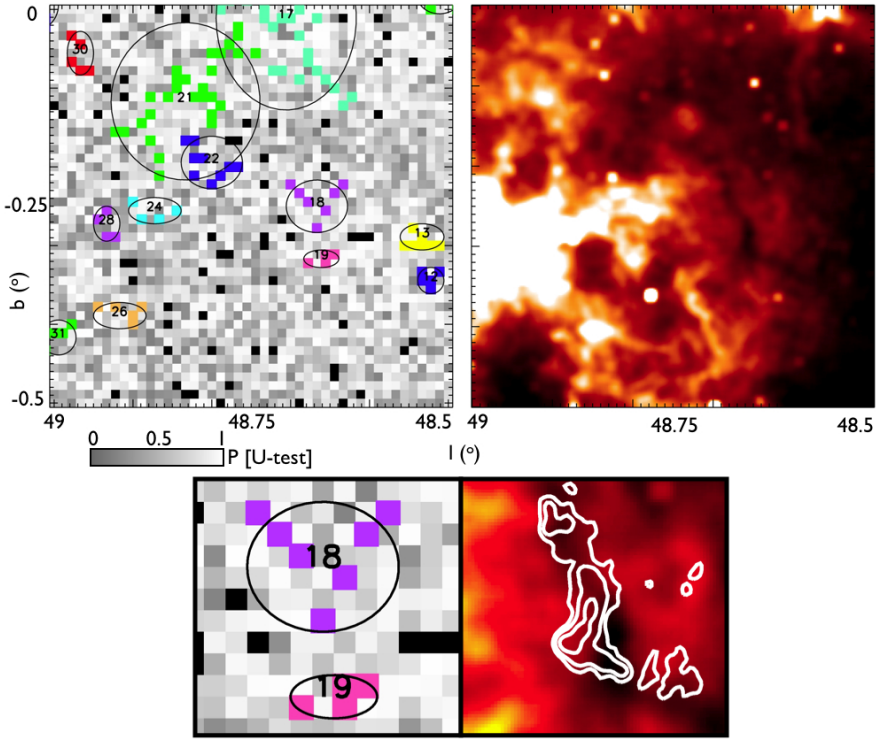

Figure 3.6: The top-left panel displays the probability image returned by the U-test toward the Inner Galaxy IRDC G48. The top-right panel shows the 8 μm image from MSX. The bright emission is coming predominantly from the star forming complex W51 at about twice the distance of the IRDC. The lower panels show a blow-up of IRDC G48. The contours on top of the MSX image display the sub-millimetre continuum emission observed with the JCMT (adopted from Ormel et al. 2005).

In order to investigate whether our method can actually see IRDC-like objects in the Outer Galaxy, we have performed the analysis described in this chapter to a number of true IRDCs in the Inner Galaxy. The important conclusion is, that they are successfully identified. We summarise the results toward IRDC G48.

IRDC G48 towards W51
At a distance of ~ 2.8 kpc, in the foreground of the bright W51 star forming cloud complex is the well-studied intermediate mass (a few 1000 $M_\odot$) IRDC labelled G48 (e.g., Shipman et al. 2003; Ormel et al. 2005). This direction in the Galactic Plane is much more populated with stars compared to the Outer Galaxy. The stellar surface density in the 2MASS data is higher by at least a factor 2. We decide to test the method in the Inner Galaxy using similar conditions. This means that we process the W51 region at the highest possible resolution, i.e., we change the resolution to $40''$ in order to meet the criterion of having at most 25% of the cells containing 5 or fewer sources. The friends-of-friends approach is performed in the same way, i.e., using a linking length L of 2.5 times the cell size. The resulting probability image and the identified objects are displayed in Figure 3.6. Objects 18 and 19 correspond to the location of the IRDC, as shown in the blow-up images. That this is a real cold and massive dark cloud can be seen from the sub-millimetre emission adopted from Ormel et al. (2005). The answer to the above question thus appears to be definite yes.

3.6.2 The Catalogue

Based on a statistical measurement of the distribution of $H - K_S$ colours of stars on a grid, we have identified 1320 high-resolution and 1589 low-resolution extended red objects in the Outer Galactic Plane. The reliability of the individual cells that make up each object is $> 99\%$. The clustering of these cells in groups of 4 or more is $\sim 99.9\%$ reliable. The majority of the objects are located toward well-known molecular cloud complexes. We have given a few examples that correspond to specific, well-studied objects such as NGC 7538 and S159 in Figure 3.5.

We present a correlation of the objects in the catalogue with existing infrared and optical data. The association with these data provide an initial step in resolving the nature of the objects. An interesting result is that we find 369 (434 for low resolution) objects with no associated sources in any of the reference catalogues. We require additional information on these objects to investigate their possible nature.

Our personal interest in producing this catalogue is the search for massive dark clouds (read IRDCs) in the Outer Galaxy. However, many other types of objects are covered. The catalogue provides one with a reliable list of extended red objects in 2MASS that can be compared to other studies in the Outer Galaxy.

Chapter 4

Towards an identification of Outer Galaxy dark clouds

– II – Near-IR extended red objects and associated ^{12}CO

W.W.F Frieswijk, R. F. Shipman and M. Spaans*

ABSTRACT

THE IDENTIFICATION of near-IR extended red objects (Chapter 3) in the Outer Galactic Plane initiated the search for massive dark clouds in a more quiescent environment compared to the inner parts of the Galaxy. However, without further investigation, the nature of the red objects remained uncertain.

In this Chapter we present an analysis of the ^{12}CO 1-0 emission, available from the FCRAO Outer Galaxy Survey, toward 414 high resolution (60″) near-IR extended red objects that were identified using 2MASS. A correlation with molecular material traced by CO, in particular when the CO is confined to specific velocities rather than an entire line of sight, suggests that the reddening of 2MASS objects is caused by foreground molecular clouds. In combination with the analysis of associated optical dark clouds, and near-IR and far-IR sources presented in Chapter 3, the results in this chapter aid in our search for massive dark clouds in the Outer Galaxy. The data are used as a 'finding chart' for follow-up investigation (Chapter 5 and 6). The CO analysis will also expand the usability of the catalogue of red objects for other studies.

Our goal is to determine whether the red objects have associated CO emission and, if so, at what velocity. We report the peak CO intensity and the maximum integrated intensity in different velocity bins (20 km s^{-1} width). At a 10σ detection level ($I_{\rm CO} \geq 1.7$ K) we find 383 objects that are associated with CO. We interpret a number of combinations of associated sources to illustrate how the data can be used. Many objects will have known counterparts, but we do not cross-correlate all objects with search-engines such as SIMBAD. This is left for future studies. A more detailed description of the region toward NGC 7538 is given to demonstrate that the analysis can lead to the identification of Outer Galaxy infrared dark clouds.

*The large amount of data produced in this Chapter will be electronically available through the ISM-group-Groningen web-page at: http://www.astro.rug.nl/∼ISMgroup/OuterGalaxy. It can also be requested by e-mail: frieswyk@astro.rug.nl

4.1 Introduction

In Chapter 3 we have introduced a catalogue of Outer Galaxy near-IR extended red objects that are identified in the Two Micron All Sky Survey (2MASS Skrutskie et al. 2006). We propose that most objects appear red due to extinction caused by foreground molecular clouds and that the catalogue may contain objects similar to Inner Galaxy Infrared Dark Clouds (IRDCs). Such objects have not been identified in the Outer Galactic Plane so far (but see Chapter 6).

An initial correlation between the catalogue and optical dark clouds (Dobashi et al. 2005), mid- and far-IR point sources (MSX, IRAS) suggests that many objects ($\sim$75%) are associated with either dark clouds, mid- to far-IR emission (possibly due to star forming activity) or a combination of the two. However, an actual association with molecular clouds can be established directly by matching the objects with molecular gas tracers.

The availability of large-scale, high-resolution ($\sim 1'$) CO surveys provides important information on the distribution of the molecular gas in the Galaxy. These surveys have been widely used, also toward the Outer Galaxy, in order to correlate pre-selected objects from other surveys with the presence of molecular gas (e.g., Brand & Wouterloot 1995; Wouterloot & Brand 1989; Kerton & Brunt 2003). In addition, catalogues are produced that contain the molecular clouds in the Outer Galaxy (e.g., Brunt et al. 2003). However, the CO itself is highly optically thick toward the Galactic Plane and therefore not suitable to use as a high column density tracer.

The Outer Galaxy extended red objects catalogue described in Chapter 3 presents an opportunity to locate objects that are identified in a completely different way, i.e., based on statistical arguments that the colour distribution of stars is red due to foreground extinction. Unfortunately, the catalogue itself does not contain any information whether a molecular cloud is present. The goal of this chapter is to support the assumption of the presence of molecular clouds and to provide additional information (e.g., distance) that can be used to identify objects of interest.

The outline of the chapter is as follows: Section 4.2 presents the CO data that we use. The method is explained in Section 4.3, where we also present the parameters that we derive from the CO. Section 4.4 gives an overview of the resulting associations and a brief interpretation of them. At the end of the section we present a detailed investigation of the region toward NGC 7538, which contains a massive dark cloud candidate. In Section 4.5 we summarise our main conclusions.

4.2 Data

4.2.1 Molecular gas tracer: CO 1-0

The Five College Radio Astronomy Observatory (FCRAO) Outer Galaxy Survey (OGS) was carried out in the mid-90s and first described by Heyer et al. (1998). It covers the Outer Galactic Plane between Galactic longitudes 102.49°and 141.54° and latitudes -3.03° and 5.41° at 45″ resolution sampled every 50.22″. The velocity range is between -152 and +40 km s^{-1} at 0.98 km s^{-1} resolution (1.39 km s^{-1} for l<106°), sampled every 0.81 km s^{-1}. The typical sensitivity of the survey is 0.6 K.

The original data were reprocessed with the main aim to improve noise levels and suppress negative emission (Brunt et al. 2003). The data were smoothed at the

Nyquist resolution limit resulting in an angular resolution of 100.44″. The CO data cubes are released as part of the Canadian Galactic Plane Survey (CGPS Taylor et al. 2003). The cubes were spatially regridded to 18″ pixels, matching the pixel scale of the CGPS. Similarly, the velocity channels are regridded to 0.82446 km s^{-1}. The reprocessed FCRAO OGS data has a typical sensitivity of 0.17 K.

The spatial extent covered by the OGS includes two major contributors to the molecular emission at different distances from us (e.g., Heyer et al. 1998). The Local spiral arm, with velocities ($V_{\rm LSR}$) ranging approximately from -20 to 4 km s^{-1} and the Perseus spiral arm, with velocities between -61 and -33 km s^{-1}. In addition, CO is seen at velocities $<$ -80 km s^{-1}, corresponding to the Far Outer Galaxy spiral arm. The local emission arises from molecular clouds within about 1–1.5 kpc from the Sun. Much of the local CO emission in the OGS constitutes low surface brightness emission ($<$ 3 K Heyer et al. 1998). The Perseus spiral arm region is located at a kinematic distance between approximately 3 and 7.5 kpc, assuming a flat rotation curve and IAU standard constants $V_\odot = 220$ km s^{-1} and $R_\odot = 8.5$ kpc. Note however, that there is a significant uncertainty in the distance of objects in the Perseus region. The distance to W3, at $l \approx 134°$, is reported as $\sim$ 2 kpc by Hachisuka et al. (e.g., 2006) and NGC 7538, at $l \approx 111°$, is often placed at $\sim$ 3 kpc (e.g., van der Tak et al. 2000). This is much closer to us than suggested by the kinematically derived distances, i.e., $\sim$ 4 kpc and $\sim$ 5 kpc, respectively.

We find no correlation between red extended objects and CO in the Far Outer Galaxy and omit further discussion of this region of the Galaxy in this chapter. Based on the identification method in Chapter 3, we do not expect to find Far Outer Galaxy clouds because of the lack of background sources in 2MASS.

4.2.2 Dark cloud candidates

Chapter 3 describes in detail the identification of near-IR extended red objects based on the 2MASS data. An initial analysis is presented there in order to obtain a census of the abnormally red colours by matching the objects with mid- and far-IR data and optically identified dark clouds. The intention here is to provide an unbiased overview of the red objects and their association with molecular gas. Therefore, we analyse the CO emission for all objects in the region where CO is available (Sec. 4.3.1), regardless of the fact whether objects correspond to well-known sources. We process the catalogue of objects that are identified at 60″ resolution. In total, 414 objects are covered by the FCRAO OGS data. Because the objects are identified as groups of cells where the star colour distribution is red, the coordinates of individual cells are adopted from Chapter 3 and used in the process of matching the CO (Sec. 4.3.2).

4.3 Method

4.3.1 Velocity bins

The goal of this chapter is to investigate whether the near-IR extended red objects are associated with molecular gas or not. In principle, a simple estimate can be obtained by correlating the objects with the Outer Galaxy Molecular Cloud Catalog (Brunt et al. 2003). However, the CO data cubes are easily accessible and we decided to

derive the CO information from the data cubes themselves, instead of being biased by a pre-selected cloud catalogue.

A line-of-sight correlation with molecular gas can be assessed by matching the objects with the CO emission integrated over the entire velocity range. However, the assumption is that the red colours of the objects are caused by extinction due to discrete foreground clouds, rather than due to material along an entire line-of-sight. Therefore, we divide the CO cubes in velocity bins of approximately 20 km s^{-1} width (the velocity resolution, 0.82446 km s^{-1}, times 24 channels $\approx$20 km s^{-1}) and match objects with CO in each velocity bin. The radial velocity information gives a rough estimate of the distance. The combined information that we present for each bin (Section 4.4) enables us to distinguish between an entire line-of-sight column of material, local CO- and distant CO-clouds.

Velocity bin	Distance (kpc) and Galactocentric radius (kpc) at Galactic longitude:									
(km s^{-1})	100°		110°		120°		130°		140°	
-10 to 10	1.6	8.9	1.1	8.9	0.9	9.0	0.8	9.0	0.8	9.1
-30 to -10	3.7	9.9	3.0	9.9	2.6	10.1	2.6	10.3	2.8	10.8
-50 to -30	5.7	11.1	5.0	11.2	4.6	11.5	4.7	12.1	5.4	13.1
-70 to -50	7.9	12.6	7.2	12.9	7.0	13.4	7.5	14.5	9.4	16.8

Table 4.1: Overview of the CO velocity bins that are used to match the extended red objects with. For the lowest velocity in each bin, the corresponding distance from us (left values) and from the Galactic Centre (right values) are given for a number of locations along the Galactic Plane.

The velocity bins are listed in Table 4.1. We include the distance corresponding to the lowest velocity in each bin for a range of Galactic longitudes. In this, we assume a flat rotation curve and the IAU standard constants $V_\odot = 220$ km s^{-1} and $R_\odot = 8.5$ kpc. Note that positive velocities do not occur when assuming a standard, flat rotation curve in the Outer Galaxy. Positive velocities presumably correspond to local material (within a few 100 parsec), where intrinsic motions dominate, rather than the line-of-sight velocity of Galactic rotation. A correlation between extended red objects and CO at more negative velocities does not occur and these bins are omitted in the table. The distance to the Perseus spiral arm (-60 $\lesssim V_{LSR} \lesssim$ -30 km s^{-1}) is possibly less than the kinematic distance listed in the table (see Section 4.2.1).

4.3.2 The procedure

Before the CO-matching is performed, the CO data cubes are regridded to the astrometry of the probability images presented in Chapter 3. Note that the size of cells that make up an object, i.e., the resolution of the probability images, is 60″ against a $\approx$100″ resolution for the CO data. A bilinear interpolation is used to sample the CO data at 60″. The CO-matching procedure runs consecutively on the individual velocity bins. It incorporates the following steps:

- For every cell that an object consists of, it produces a one-dimensional spectrum of CO emission at that location.
- The upper quartile intensity is determined, i.e., the median intensity of the upper half of the spectrum.
- It determines the peak of the CO emission, which can be in any of the cells.
- We adopt a noise of σ=0.17 K (see Section 4.3.3: *Upper quartile intensity: noise estimate*) for all velocity bins and define that an object is associated with CO if the peak intensity is at least a 10σ signal. In that case, the procedure determines the velocity at which the peak of emission occurs.
- The one-dimensional spectra are integrated over the velocity bin, and the maximum integrated emission is determined.
- Images of the CO emission integrated over the velocity bin are produced.

4.3.3 Notes on derived parameters

Peak CO intensity

The peak CO intensity is given in units of Kelvin (K) on the radiation temperature scale (T_R^*) in columns 2, 6, 10 and 14 of Table 4.2 in the Appendix. Because CO is optically thick under general ISM conditions it can be used as a tracer of the excitation temperature ($T_{\rm ex}$) at the surface where the optical depth (τ) is unity. From basic radiative transfer follows (e.g., Dickman 1978) that the excitation temperature is given by

$$T_{\rm ex} = \frac{5.53}{\ln[1 + \frac{5.53}{T_{\rm R}^*({\rm CO})+0.782}]} \ ({\rm K}) \ , \tag{4.1}$$

where the constants include a background temperature of 2.7 K. The excitation temperature is approximated (within 0.5 K) by adding 3 K to the radiation temperature. However, we do not intent to derive actual temperatures of the objects. First, because the temperature is only representative of a single cell. Second, the τ=1 surface is located at an unknown depth inside a cloud and a physical interpretation of the temperature is difficult. Third, because of the low resolution (100″), the CO emission on small spatial scales is smeared out over the beam. Furthermore, there is always a contribution to the emission due to low column density CO gas. The magnitude of these effects is obviously unknown. Therefore, the temperatures have no unambiguous physical meaning. What this merely demonstrates is that higher observed CO intensities probably correspond to warmer environments. E.g., this may indicate the presence of star forming activity. An example of a high CO intensity is presented in Section 4.4.7, i.e., object 470.

Velocity at maximum CO intensity

It should be kept in mind that the derived velocity in each bin corresponds to the peak CO intensity. It is likely that the other cells of an object have their peak intensity at a similar velocity if they correspond to the same cloud. However, because the identification of extended red objects is in projection on the sky, overlap between multiple components in one velocity bin can occur. Obviously, line-of-sight confusion between different velocity bins occurs frequently because we are observing through both the local spiral arm and the Perseus spiral arm.

Maximum integrated intensity

We determine a value of the maximum integrated intensity of an object (in a single cell). We do not interpret this as a measurement of a physical parameter. However, it can be useful to compare this value with the peak intensity in order to distinguish between narrow emission features (peak intensity $\approx$ integrated intensity) and broad emission features (peak intensity $\ll$ integrated intensity). Caution should be taken when considering emission at the edges of velocity bins. In that case, the true integrated emission of a CO component is divided over two bins. Also the presence of multiple components in one velocity bin can be misleading and a visual check on the spectra is always advised.

Upper quartile intensity: noise estimate

The upper quartile, or median of the upper half, of the intensity gives a good estimate of the noise if there is no emission in a spectrum. This approximation still gives a reasonable estimate if less than 25% of the spectrum is filled by a true signal. For all velocity bins, we investigate the distribution of the upper quartiles. The median value of the distribution is about 0.17 K for the first velocity bin (-10 to +10 km s^{-1}) and decreasing to 0.13 K for the last velocity bin (-70 to -50 km s^{-1}). The average values are higher ($\sim$ 0.25 K). This is because the distribution is skewed toward higher values. However, the high values of the upper quartile arise from the fact that often too much signal is present in a velocity bin. A high value of the upper quartile is often encountered when emission features are broad (FWHM $\gtrsim$ 5 km s^{-1}), or, when multiple components of CO are present in the respective velocity bin. Based on the values above, we conclude that the noise that we use to define an association, i.e., 0.17 K, is an appropriate choice.

4.3.4 Tables and figures

Table 4.3 in the Appendix presents an excerpt of the table of CO associations with extended red objects. The full tables can be obtained on request from W. Frieswijk. The objects listed in the table correspond to those in the region near the star forming complex NGC 7538. Similar as in Chapter 3, this region will be discussed in Section 4.4.7. The different columns in Table 4.3 give the following information:

Column (1): Identification number of the objects, adopted from Chapter 3.
Column (2): The peak intensity, as described in Section 4.3.3, in the velocity bin ranging from -10 to 10 km s^{-1}.

Column (3): Velocity of the peak intensity in this bin. Blank values indicate that there is no emission present above the 10σ level.
Column (4): The maximum integrated intensity in a single cell, as described in Section 4.3.3.
Column (5): The upper quartile intensity as an estimate of the noise. See Section 4.3.3 for further explanation.

Columns (6) to (9), (10) to (13) and (14) to (17) give the same information for the velocity bins centred on -20, -40 and -60 km s^{-1}, respectively.

The values presented in the table give an initial indication of the presence of molecular gas. However, images can reveal much more detail. In particular, the spatial extent and correlation between the extended red objects and CO is difficult to express in numbers because of the way the objects are identified, i.e., as grouped but not necessarily neighbouring cells (see Chapter 3). For all objects we produce images of the CO emission integrated over the different velocity bins. Overlaid on the images are the locations of the cells of an object as well as two spectra. The first spectrum (solid line) shows the emission of the cell that contains the peak CO intensity. The second spectrum (dashed line) shows the total emission, i.e., the emission integrated over cells. All figures are available on request from W. Frieswijk. In Appendix 4.A we present the figures corresponding to the objects listed in Table 4.3.

4.4 Results

In this section we present some basic results that we derive from the CO analysis. It is by no means a complete overview of what is available in the tables. The main purpose is to show how the data can be used. Where we feel that it is appropriate we specifically mention typical objects, but these serve only as an example. At the end of this section we examine the region toward NGC 7538 in some more detail. We show particular interest in this region because it contains the first Outer Galaxy infrared dark cloud candidate identified as such (see Chapter 5). The identification followed from the analysis presented in Chapter 3 and the information presented in this Chapter.

4.4.1 No CO association

We choose a CO emission threshold of 1.7 K as a lower limit definition to identify whether an extended red object is associated with CO. This corresponds to an approximate 10σ signal in all velocity bins. Of the 414 objects that we have investigated, 31 have no CO counterpart in any of the velocity bins. Five of these objects do have an association with an optical dark cloud (Chapter 3). These are objects 341, 381, 496, 498 and 690.

Only 11 of the 31 objects have no CO signal above 1 K. We do not have an explanation why these objects were identified. Some may be affected in their colour by a neighbouring bright star in 2MASS (e.g., 353, 354). Two other objects are worth mentioning. Object 350 and 402 have a significant excess in 2MASS objects, i.e., 14 and 13 stars on average per cell with the peak at 19 and 17 stars per cell, respectively.

Compared to the median in these regions, 10 and 9 respectively, these values are excessively high. Both objects are within 6′ of CO emission in the velocity bin centred on 0 km s^{-1}. Perhaps these objects represent clusters of stars that have been removed from their natal cloud.

4.4.2 Nearby clouds

Nearby clouds have a fair chance of being identified as optical dark clouds. For simplicity, we define all CO with a velocity higher than -30 km s^{-1} as local. If we consider the separate velocity bins, then 255 objects have a counterpart in CO at velocities in the bin centred on 0 km s^{-1} and 240 objects in the bin centred on -20 km s^{-1}. For these velocity bins, 135 and 128 of the objects have also an optical dark cloud associated. However, this does not take into account the possibility of additional CO components at larger distances. If we consider only the local CO associations, i.e., without any distant counterparts, there are 195 out of a total of 225 objects identified ($\sim$85%).

4.4.3 Distant clouds

We do the same analysis for objects associated with distant CO, i.e., $V_{\rm LSR}$<-30 km s^{-1}. In the separate velocity bins, -40 km s^{-1} and -60 km s^{-1}, we find 119 and 75 objects with 43 and 29 associations with optical dark clouds, respectively. Considering the distant CO associations without nearby counterparts, we find 65 objects out of which 37 have an optical dark cloud associated.

4.4.4 Infrared sources

$N_{\rm MSX}$	$N_{\rm objects}$	$< I_{\rm CO} >$ [K]	$\sigma(I_{\rm CO})$ [K]
=0	187	4.3	1.9
$\geq$1	227	6.7	4.2
$\geq$3	39	11.0	5.3
$\geq$5	13	14.8	4.9

Table 4.2: Column 1 represents the number of associated MSX objects that is being considered. Column 2 gives the number of extended red objects that have the respective number of MSX sources associated. Column 3 gives the average CO peak intensity of the objects. Column 4 gives the spread of the peak-CO intensity.

The association with infrared sources (IRAS, MSX), in particular when multiple sources are present, can give an indication of star forming activity. Of the 414 sources that have been matched with CO, 227 have at least one infrared source associated. If star forming activity is occurring, a presence of relatively warmer CO gas may be expected. Table 4.2 gives an overview of the correlation between the number of MSX sources associated with objects and the average of the CO peak intensity. Although the spread in the CO peak intensities is significant, the trend of the average value indicates an increase of the CO peak intensity for increasing infrared associations. The

overall properties of CO and the association with infrared sources in the catalogue are in agreement with our expectations.

4.4.5 Kinematics

As described in Section 4.3.3, we determine the maximum integrated intensity in order to distinguish between narrow emission features and broad emission features. If we assume for simplicity that features have a Gaussian profile, we can derive a rough measure of the width of the CO emission. The ratio of the integrated intensity and the peak intensity gives an approximation to the Full Width Half Maximum (FWHM) of the Gaussian distribution, i.e.,

$$\frac{I_{\max}}{\Sigma_{\max} I} = \frac{\sqrt{2\pi}}{2\sqrt{2\ln 2}} \times \mathrm{FWHM} \approx \mathrm{FWHM} \; . \tag{4.2}$$

Figure 4.1 displays the distribution of the FWHM for CO components that are present in all velocity bins. The light-grey histogram represents the CO of all objects and all components. The measured FWHM in a velocity bin is narrower than the actual FWHM if the CO emission is near the edge of a bin. This is illustrated by the shaded histogram, which displays the distribution of the FWHM for CO components that lie $> 2\,\mathrm{km\,s^{-1}}$ away from the bin edges.

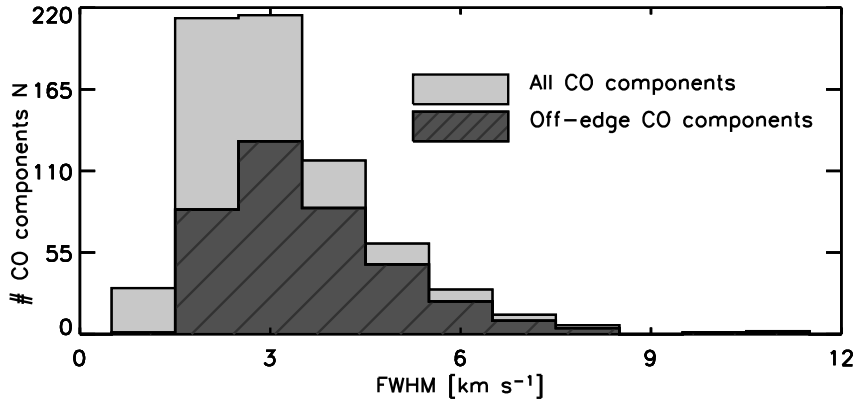

Figure 4.1: Distribution of the estimated FWHM of the CO emission features present in all velocity bins, assuming these features have Gaussian profiles.

The FWHM truncates at low velocities because of the finite velocity resolution, i.e., $\approx 0.8\,\mathrm{km\,s^{-1}}$. Most objects have a FWHM around 2–4 $\mathrm{km\,s^{-1}}$, which is a typical velocity width for molecular clouds. We interpret this result as evidence that the reddening of the objects is predominantly due to extinction caused by discrete molecular clouds. The higher FWHM values ($> 5\,\mathrm{km\,s^{-1}}$) may indicate that we are observing either large cloud complexes or multiple components.

4.4.6 Galaxies

We mention objects 555 and 557 as two examples to show that some objects correspond to extra-galactic sources. Object 555 is associated with IRAS and MSX emission as well as CO emission at -38 and -60 km s^{-1}. It corresponds to the location of a galaxy labelled LEDA 750. Object 557 is associated with CO emission at -50 km s^{-1} and is also associated with MSX and IRAS sources. It was reported as an unknown object by Brunt et al. (2003). Both objects may have been identified in 2MASS as extended red objects because the colours of stars were measured incorrectly due to confusion with the emission coming from the galaxies.

4.4.7 Example region: NGC 7538 and its surroundings

Appendix A at the end of this chapter presents figures for a number of objects in the region toward NGC 7538. This region is also discussed in Chapter 3 and Figure 3.5 can be used to locate the positions of the objects. We display the images and spectra that resulted from the CO analysis for a number of typical objects in the region. This illustrates the power of the method and demonstrates how the images can be interpreted. The caption of the first figure explains the information that is presented. We briefly discuss the different objects here.

Object 463 (Figure 4.2) matches with the CO emission around -55 km s^{-1} and corresponds to the well-studied massive star forming region NGC 7538, located at a distance of about 2.8 kpc from us in the Perseus spiral arm (van der Tak et al. 2000). Some local CO emission around -10 km s^{-1} is present along the line-of-sight. Note that the CO emission is broad, especially in the bin centred on -60 km s^{-1} (FWHM $\sim$ 10 km s^{-1}). This gives an example of a case where the noise determination from the upper quartile emission fails (Section 4.3.3; upper quartile gives 5.66 K). Note also, that the broadness of the emission can be approximated from the values in Table 4.2 (see 4.4.5); the ratio of the integrated intensity (194.9 K km s^{-1}) and the peak intensity (17.1 K) gives a width of 11.4 km s^{-1}.

Objects 469, 476 and 486 (Figures 4.3, 4.6 and 4.8, respectively) are located north of NGC 7538 and belong to a filamentary structure of extended red objects. In Chapter 3 we suggest that this region corresponds to local dark clouds with some low-mass star forming activity. This idea is based on the absence of extended mid-IR emission, the presence of mid-IR-point sources and the association of some of the objects with optically identified dark clouds. The CO emission toward these objects identifies them as local molecular clouds. All have emission features around -10 km s^{-1}, supporting the suggestion mentioned above. Interestingly, the identification method that we present in this thesis finds objects that often correspond spatially well with the outline of local peaks in the CO emission. The three objects displayed here exemplify this result for nearby clouds. Objects 469 and 486 have a nearby ($< 10'$) Lynds dark cloud (Lynds 1962) associated, i.e., LDN 1227 and LDN 1234, respectively. Note however, that the position of LDN 1227 does not fall within the spatial extent of object 469. Object 476 is associated with an optically identified dark cloud (Dobashi et al. 2005).

Object 470 (Figure 4.4) consists only of 8 cells. It is an example of an object at larger distance that is spatially well correlated with CO. The object corresponds to the well-known source S159, also located in the Perseus spiral arm at a distance of 3.1 kpc (Brand & Blitz 1993). Active star formation is observed in the immediate surrounding of S159 in the form of multiple compact HII regions (e.g., Lebrón et al. 2001). Probably, this is reflected also by the high peak intensity of CO (26.2 K), as explained in Section 4.3.3.

Object 474 (Figure 4.5) is an important object throughout this thesis. It represents one of the larger extended red objects (12′ by 20′). CO emission is present around both -10 km s^{-1} and -50 km s^{-1}, depending on which part of the object is considered. It exemplifies that the identification method cannot distinguish between clouds at different distances along the line of sight. In projection on the sky, the objects appear to be one and the same. The distant CO component makes this object interesting. The relatively cold (13.3 K) and broad ($\sim$ 10 km s^{-1}) CO emission, combined with the fact that no known objects are found to be associated (except for some weak IRAS and MSX point-sources) made us select object 474 as our primary target for follow-up observations. The target area for these observations covers the cells identified in the lower region of the image, i.e., those that correspond only to CO emission around -50 km s^{-1}. Chapters 5 and 6 present the observations and show that this object is the first Outer Galaxy IRDC identified as such.

Object 478 (Figure 4.7) is located just left of our primary target and is associated with dark cloud LDN 1232. This object gives an even better example of confusion between CO components along the line-of-sight. Most of the identified cells have CO emission at both the local and distant velocity, which makes it impossible to determine the cause of the red colours. It is clear though, that the CO emission around -60 km s^{-1} is much narrower ($\sim$ 5 km s^{-1}) compared to the width observed for object 474.

4.5 Conclusions

The main conclusion and bottom-line of the CO analysis is, that we have found 383 CO associations out of a total of 414 objects, i.e., $>$ 90%. The rough estimate of the velocity width of CO features indicates that we are observing molecular clouds, as was suggested in Chapter 3. We conclude that the red appearance in 2MASS is most likely due to extinction caused by these clouds.

The results of the analysis presented here and in Chapter 3 are used as a 'finding chart' for massive dark clouds in the Outer Galaxy. After selecting candidates, follow-up observations are required to further investigate the nature of the objects, e.g., by using molecular lines or sub-millimetre/IR continuum observations. The candidate that we put forward in this chapter, i.e., G111.80+0.58 near NGC 7538, was selected this way and follow-up observations are presented in Chapters 5 and 6.

4.A The NGC 7538 region: Tables and figures

Table 4.3: CO toward objects in the NGC 7538 region

ID	v=10 to -10 km s^{-1}				v=-10 to -30 km s^{-1}				v=-30 to -50 km s^{-1}				v=-50 to -70 km s^{-1}			
(1)	(2)	(3)	(4)	(5)	(6)	(7)	(8)	(9)	(10)	(11)	(12)	(13)	(14)	(15)	(16)	(17)
	I_{max}	$V_{I_{max}}$	$\Sigma_{max} I$	σ	I_{max}	$V_{I_{max}}$	$\Sigma_{max} I$	σ	I_{max}	$V_{I_{max}}$	$\Sigma_{max} I$	σ	I_{max}	$V_{I_{max}}$	$\Sigma_{max} I$	σ
456	6.56	-9.71	8.55	0.16	5.48	-10.53	6.95	0.17	0.39	-	0.23	0.12	2.76	-51.76	7.13	0.12
458	6.41	-9.71	7.48	0.10	6.99	-10.53	9.41	0.13	1.69	-	2.15	0.12	1.70	-	3.63	0.08
462	8.41	-8.88	22.48	0.23	5.83	-10.53	10.81	0.14	2.27	-49.28	3.99	0.14	2.35	-50.11	5.78	0.12
463	3.34	-9.71	6.46	0.12	3.02	-10.53	5.11	0.12	8.76	-49.28	34.05	0.29	17.10	-56.70	194.88	5.66
464	5.69	-9.71	8.90	0.10	6.94	-10.53	12.75	0.11	1.12	-	2.16	0.11	5.31	-54.23	22.24	0.25
465	8.38	-9.71	24.87	0.20	5.13	-10.53	6.06	0.14	0.39	-	0.85	0.13	2.35	-54.23	6.11	0.13
466	8.14	-9.71	22.16	0.26	3.80	-10.53	9.70	0.26	0.67	-	1.33	0.09	0.42	-	1.07	0.13
468	7.86	-9.71	21.85	0.71	3.92	-10.53	9.22	0.13	2.54	-49.28	5.43	0.16	2.66	-50.11	5.16	0.17
469	8.76	-9.71	25.03	0.18	8.31	-10.53	10.81	0.12	0.43	-	0.77	0.08	0.34	-	0.54	0.09
470	0.44	-	0.93	0.09	0.50	-	0.75	0.12	1.23	-	2.48	0.15	26.18	-55.88	124.88	5.47
472	1.67	-	2.89	0.20	3.80	-10.53	7.97	0.13	8.78	-49.28	30.05	1.22	9.06	-50.11	44.70	0.59
473	0.40	-	0.64	0.11	7.38	-28.67	35.02	0.25	5.88	-31.14	31.50	0.47	0.54	-	0.47	0.15
474	5.59	-9.71	15.42	0.16	5.46	-10.53	7.94	0.11	10.28	-49.28	66.28	1.21	13.28	-51.76	96.07	2.07
475	4.61	-9.71	9.68	0.11	7.53	-11.36	14.39	0.11	6.71	-49.28	21.25	0.24	12.49	-51.76	71.03	2.20
476	9.89	-9.71	32.55	1.47	8.40	-10.53	11.32	0.12	1.28	-	3.35	0.09	0.43	-	0.62	0.12
477	0.65	-	0.12	0.14	0.52	-	1.85	0.13	1.53	-	1.57	0.07	11.06	-53.40	62.00	4.11
478	7.34	-9.71	18.74	0.15	4.70	-10.53	7.89	0.12	13.28	-48.46	50.04	0.25	14.75	-50.93	66.49	0.35
479	7.55	-9.71	12.57	0.14	5.84	-10.53	9.58	0.17	4.88	-49.28	12.61	0.16	3.67	-50.11	6.03	0.16
480	6.03	-9.71	17.00	0.23	6.45	-10.53	11.27	0.07	0.32	-	0.51	0.07	0.31	-	0.16	0.10
481	8.29	-9.71	24.52	0.39	5.08	-10.53	9.45	0.09	0.26	-	0.44	0.07	0.54	-	1.52	0.11
482	6.20	-9.71	13.43	0.10	5.95	-10.53	8.60	0.10	7.33	-48.46	28.96	0.37	2.65	-50.11	4.54	0.10
483	7.10	-9.71	18.38	0.46	4.40	-10.53	5.11	0.14	0.46	-	1.12	0.10	0.36	-	0.18	0.08
484	7.57	-8.88	25.90	0.26	3.15	-10.53	5.22	0.16	0.44	-	0.70	0.08	0.47	-	0.88	0.13
486	5.08	-9.71	14.23	0.19	6.54	-10.53	30.79	0.64	0.57	-	1.31	0.14	0.50	-	1.33	0.14

Object 463: NGC 7538

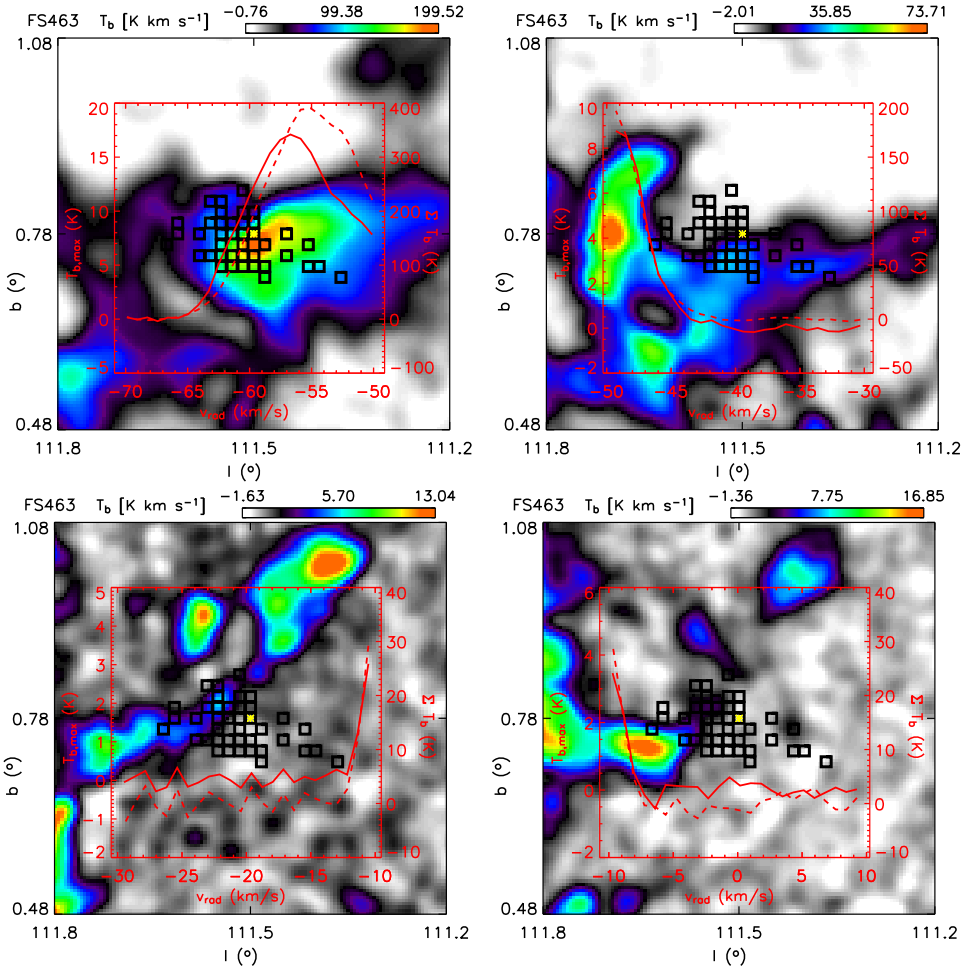

Figure 4.2: The figures presented in this Appendix are the result of the CO matching, described in Section 4.3.2, with the extended red objects identified in Chapter 3. The colour images give the integrated CO emission over each velocity bin, scaled according to the colour bars on top. The velocity bins are 20 km s^{-1} wide and centred on: -60 km s^{-1} (top left), -40 km s^{-1} (top right), -20 km s^{-1} (bottom left) and 0 km s^{-1} (top right). The black squares represent the cells that make up the extended red object. The solid line is the CO spectrum in the cell that contains the peak intensity (left axis). The dashed line is the CO emission summed over all cells (right axis). The title at the top gives the object identification number followed by an Astronomical designation if it corresponds to a well-known source in SIMBAD. A question-mark indicates that the well-known source is located nearby ($\sim$ a few arc-minutes), but the position does not fall within the identified region of the extended red object.

Object 469: LDN 1227 ?

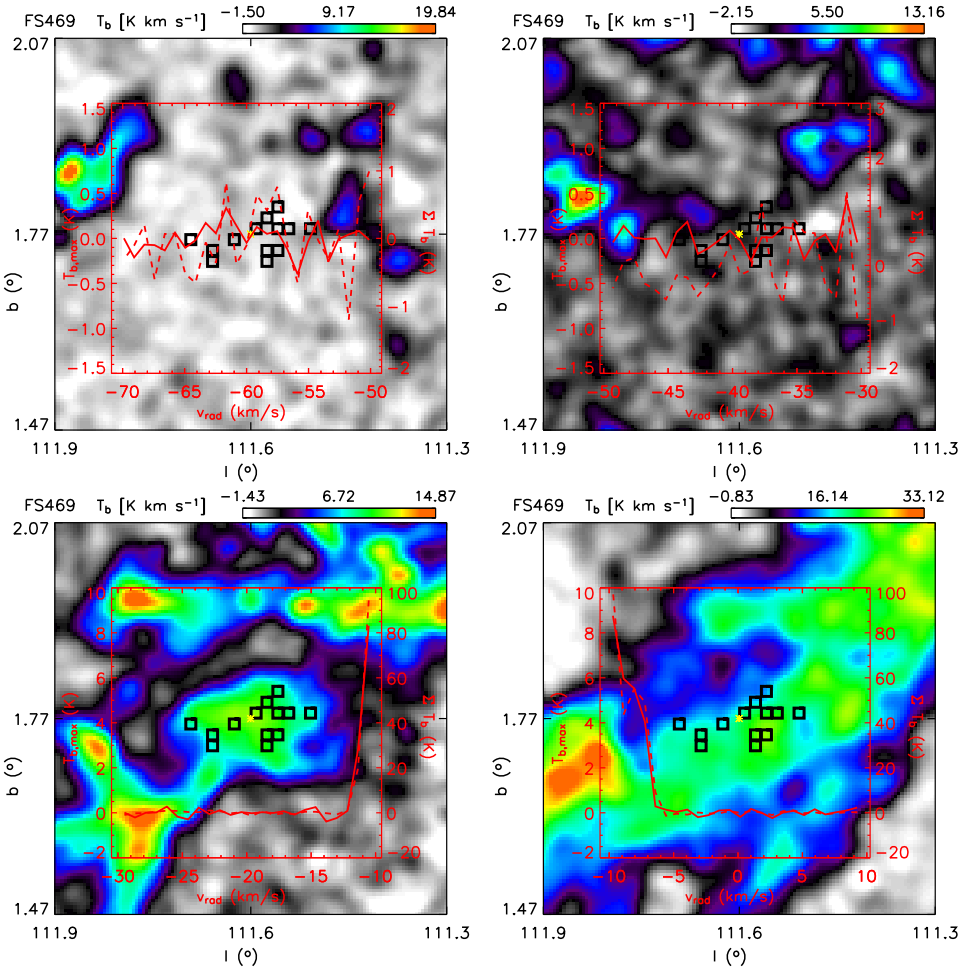

Figure 4.3: Same as Figure 4.2 for object 469.

Object 470: S159

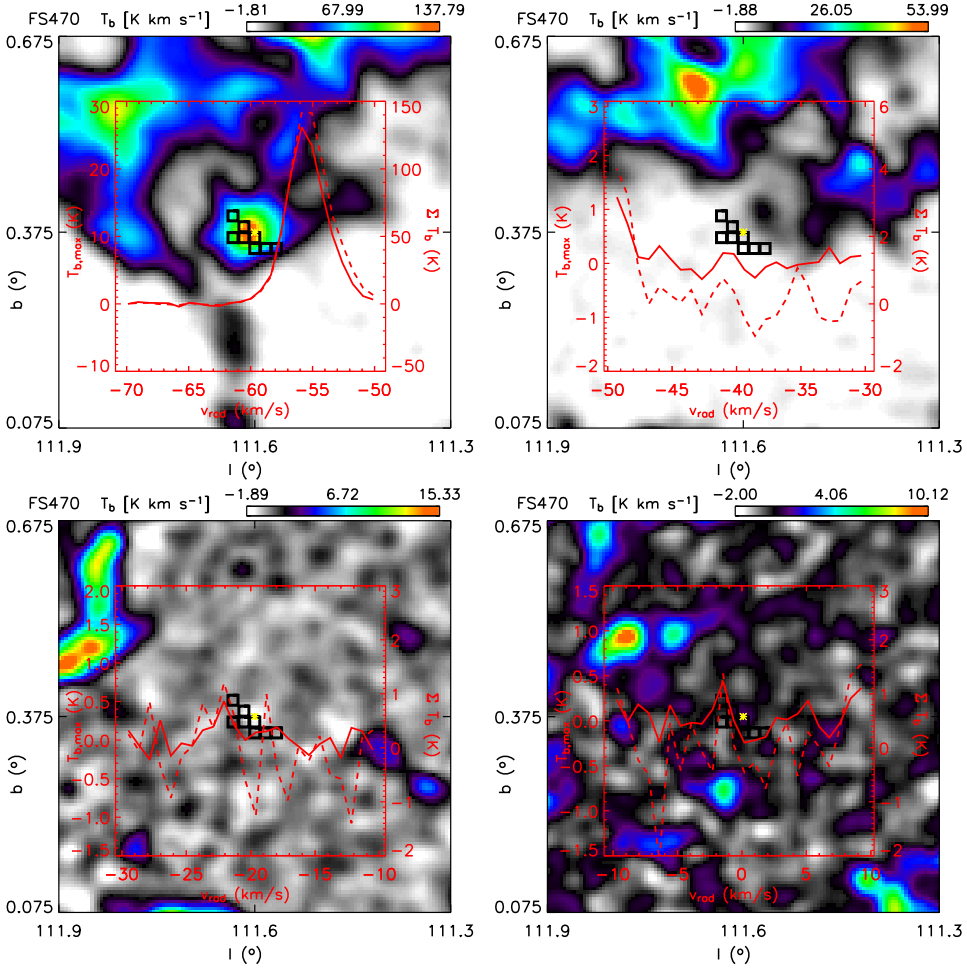

Figure 4.4: Same as Figure 4.2 for object 470.

Object 474: Selected candidate for Outer Galaxy IRDC

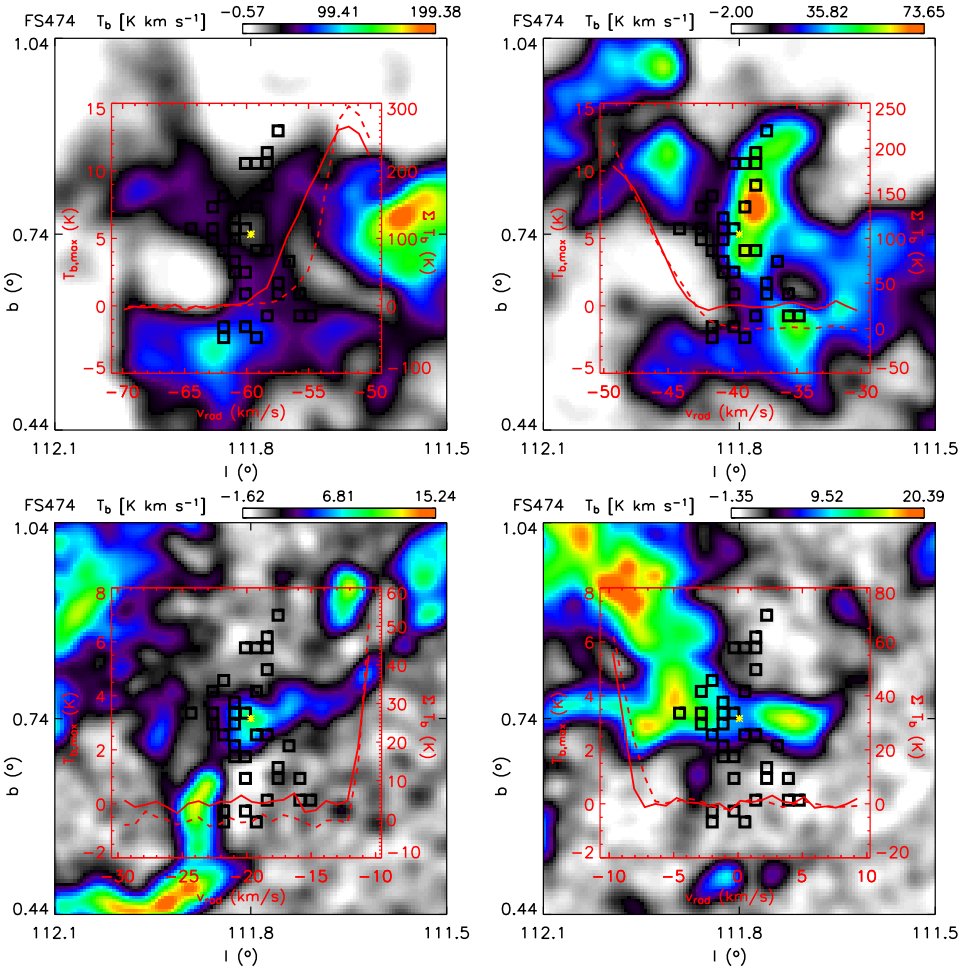

Figure 4.5: Same as Figure 4.2 for object 474.

Object 476: Optically identified dark cloud

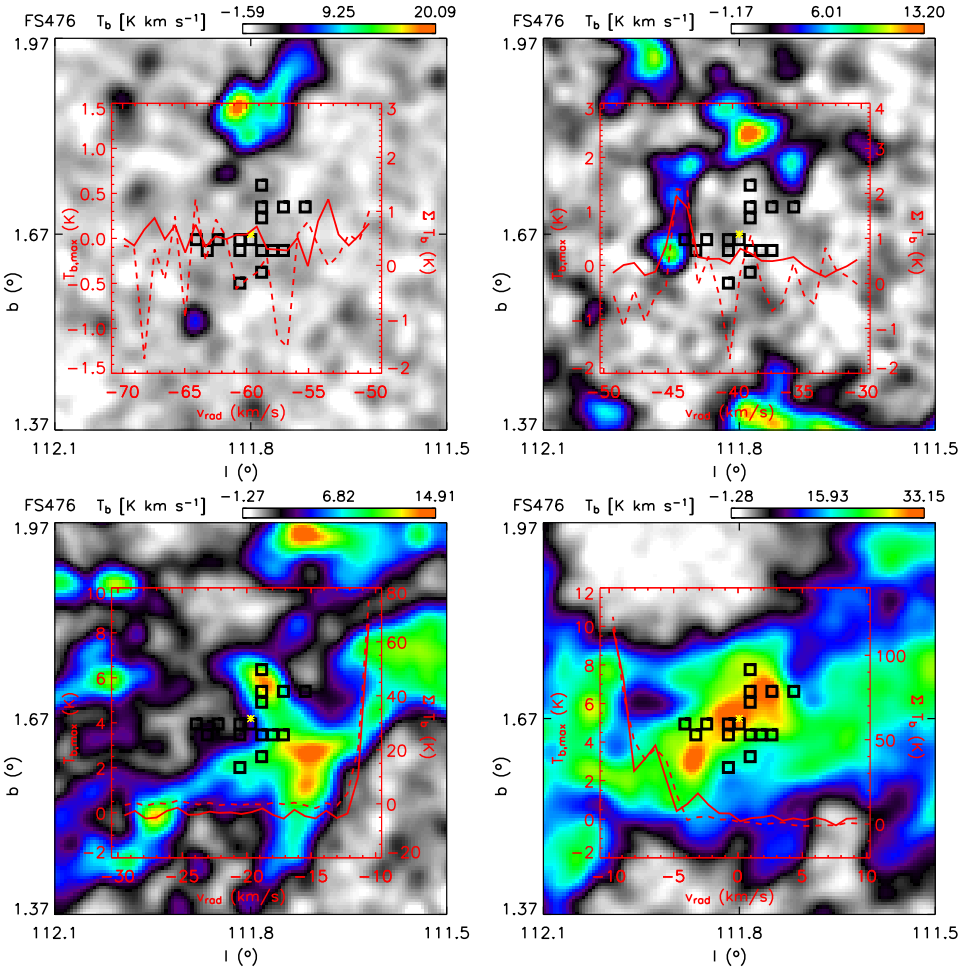

Figure 4.6: Same as Figure 4.2 for object 476.

Object 478: LDN 1232

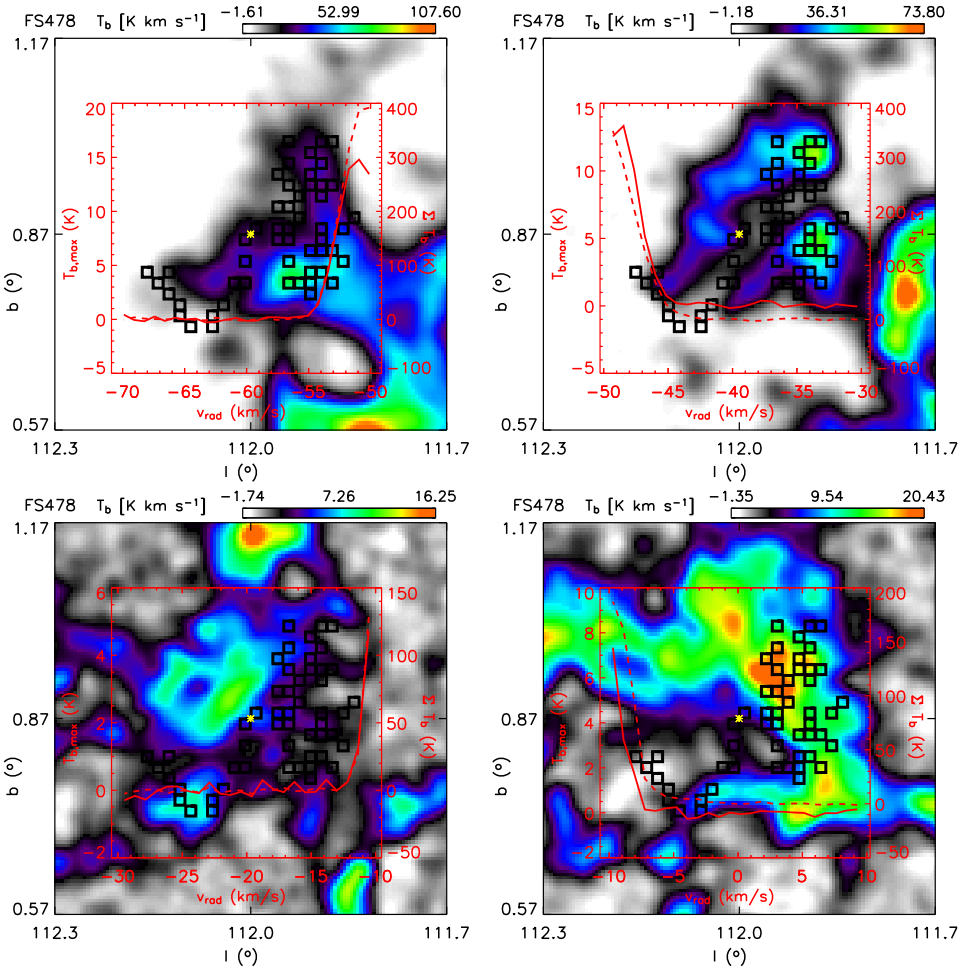

Figure 4.7: Same as Figure 4.2 for object 478.

Object 486: LDN 1234

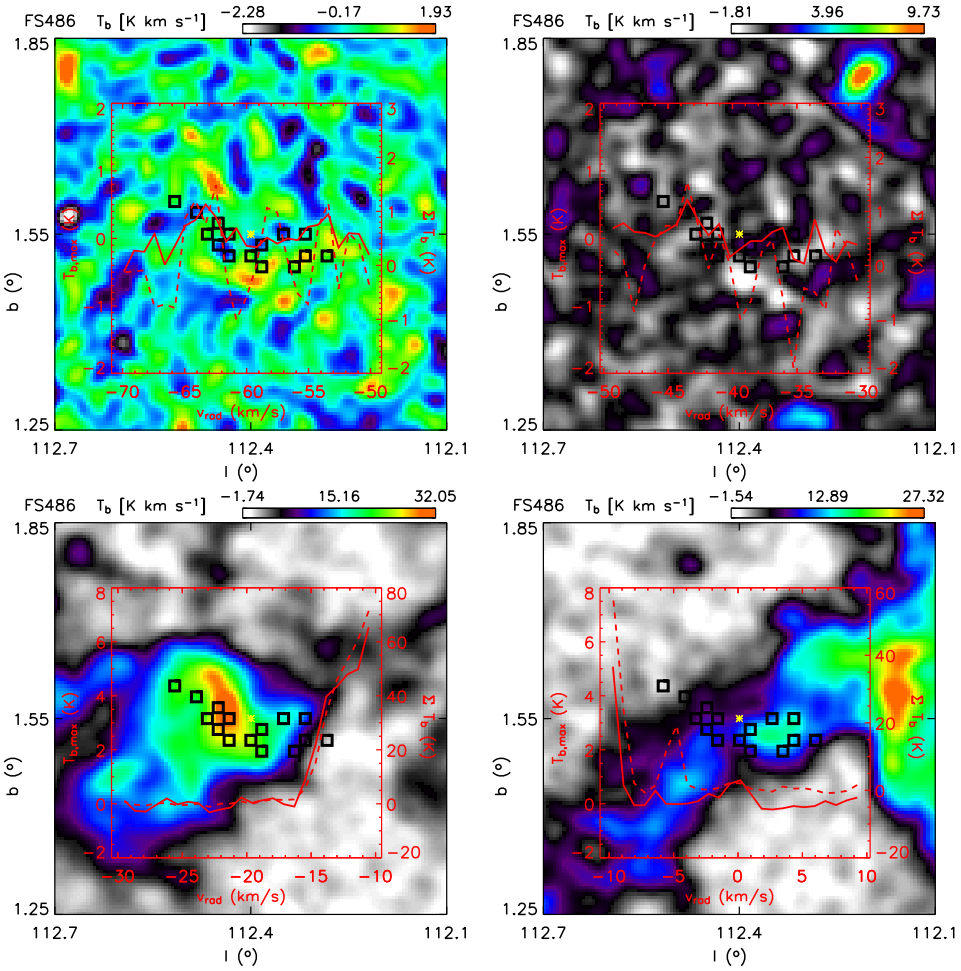

Figure 4.8: Same as Figure 4.2 for object 486.

Chapter 5

Physical characteristics of a dark cloud in an early stage of star formation toward NGC 7538 – An Outer Galaxy Infrared Dark Cloud?

W. W. F. Frieswijk et al. 2007*

ABSTRACT

THIS CHAPTER presents a detailed study of the Outer Galaxy dark cloud candidate G111.80+0.58, based on molecular line observations (^{13}CO, C^{18}O, C^{34}S and NH_3). The object is located in the vicinity of active star forming regions such as NGC 7538 and S159.

We analyse the line data in terms of excitation temperature, column and volume density, mass and stability. The temperatures we find (15 – 20 K) are higher than expected from only cosmic ray heating, but are comparable to those found in massive cores, such as IRDCs. Star forming activity could be present in some cores, as indicated by the presence of warm gas (NH_3, ^{13}CO self-absorption) and Young Stellar Object candidates. The observed super-thermal line-widths are typical for star forming regions. The velocity dispersion is consistent with a turbulent energy cascade over the observed size scales of the complex. We do not find a correlation between the gas temperature and the line-width. The LTE masses we derive are much larger than the thermal Jeans mass. Therefore, fragmentation is expected and may have occurred already, in which case the observed lines represent the combined emission of multiple unresolved components.

We conclude that G111.80+0.58 is a molecular core complex with bulk properties very similar to IRDCs in an early, but not pristine, star forming state. The individual cores are close to virial equilibrium and some contain sufficient material to form massive stars and star clusters. The ambient conditions suggest that turbulence is involved in supporting the cores against gravitational collapse, at least down to the observed sizes. Additional high resolution data are necessary to resolve and analyse the smaller scale properties.

*Published as Frieswijk, W. W. F., Spaans, M., Shipman, R. F., Teyssier, D., & Hily-Blant, P. 2007, A&A, 475, 263

5.1 Introduction

Infrared Dark Clouds (IRDCs) were discovered a decade ago as dark silhouettes against a bright mid-infrared background by the Midcourse Space Experiment (MSX, Egan et al. 1998) and the Infrared Space Observatory (ISO, Pérault et al. 1996). Many IRDCs contain compact (sub-) millimetre cores (Carey et al. 2000; Garay et al. 2004; Ormel et al. 2005; Rathborne et al. 2005) and the current picture is that these massive dense cores represent the early, cold stages of clustered star formation (Rathborne et al. 2006; Menten et al. 2005, and references therein) and that they are potentially the birth sites of massive stars. In order to assess the role of IRDCs in the process of star formation, their ambient physical conditions need to be determined. Only then insight may be gained into the differences between low- and high-mass star formation, the nature of the initial mass function and the impact of environment on star (cluster) formation. That is, the putative early stage that IRDCs represent implies that their physical state provides a direct record of the initial conditions pertinent to stellar birth.

A complete picture of the star forming properties in massive dark clouds, specifically the effects of external conditions on the formation process, requires a study of similar objects in different environments. The Outer Galaxy obviously represents the place in our Galaxy where the conditions, such as metallicity, density, interstellar radiation field and overall star forming activity are different compared to the inner regions of the Galaxy (e.g., Brand & Wouterloot 1995; Rudolph et al. 2006). Variations of these properties from cloud to cloud may affect the local star formation rate, the mass distribution (IMF) or the star forming efficiency. In fact, only a direct comparison between Inner and Outer Galaxy star forming regions can asses in what way star formation differs with Galactic radius, if at all. However, due to a lack of bright background emission elsewhere, IRDCs were identified only in the inner parts of the Galaxy, mainly toward the Molecular Ring and the inner spiral arms (Simon et al. 2006b). Can we identify massive dark clouds in an early evolutionary stage in the Outer Galaxy using a different approach?

Frieswijk & Shipman (2007, Chapter 4, FS07 hereafter) propose a list of candidate IRDC-like objects in the Outer Galactic Plane in their investigation of the distribution of highly reddened point sources observed in the Two Micron All Sky Survey (2MASS, Skrutskie et al. 2006). They suggest that a number of these clustered red sources are reddened due to foreground extinction in the form of dark clouds. As a verification of the presence of molecular material, they identified CO structures, observed in the Five College Radio Astronomy Observatory CO Survey of the Outer Galaxy (FCRAO, Heyer et al. 1998), that match the global morphology of the regions. Even though CO traces mainly the outer layers of molecular clouds, the amount of extinction they find indicates the presence of large column densities. A subset of the structures in this near-IR study are not associated with MSX or IRAS point sources and this would also suggest an early star forming nature. Additional data, e.g., of molecular lines and dust continuum are required to confirm if some of these near-IR structures are indeed the Outer Galaxy counterparts to the Inner Galaxy IRDCs.

In this paper we present follow-up molecular line observations of Outer Galaxy dark cloud candidate G111.80+0.58 in the direction of Cepheus in the Perseus spiral

arm. We derive physical properties for a number of dense cores located along the filamentary cloud structure, such as temperature, density and mass and we characterise the nature of the cloud by comparing the results to existing studies. The cloud is part of the Cas OB2 complex at a radial velocity around $-55\,\mathrm{km\,s^{-1}}$ (e.g., Blitz et al. 1982). There are a few well-known star forming regions located nearby, such as NGC 7538 and S159 . NGC 7538 is actively forming stars and extensive studies have been conducted and reveal various stages of evolution including compact dense cores, HII regions, several massive proto-stellar objects and many lower mass Young Stellar Objects (YSO's) (e.g., Werner et al. 1979; Kameya et al. 1990; Sandell & Sievers 2004). S159 is a bright reflection nebulae illuminated by an optically visible O-type star (Chini & Wink 1984). Part of the cloud is associated with IRAS 23133+6050 and seen as an emission nebula. In the immediate surrounding of S159 several compact radio continuum sources and (compact) HII regions have been identified (e.g., Lebrón et al. 2001).

Section 5.2 describes how the object was identified and gives a brief overview of the the appearance of the region and its immediate environment in MSX, 2MASS and FCRAO data. The observational setup and the target positions are given in Section 5.3 and Section 5.4 describes the observational properties. The derived physical properties of the cores are given in Section 5.5. In Section 5.6 we discuss the results and present our conclusion on the nature of dark cloud G111.80+0.58. Section 5.7 ends with some concluding remarks.

5.2 G111.80+0.58: Source selection

G111.80+0.58 was selected from a list of candidate dark clouds. This list comprises all sources that were identified in the 2MASS Point Source Catalog (PSC) as extended red features in the Outer Galactic Plane (FS07). In this work, a statistical measure, using the Mann-Whitney-U-test, is performed on a $60'' \times 60''$ grid covering the entire Outer Galactic Plane. Adjacent cells where the $H - K_S$ colour distribution of stars is different from the local surroundings on a high ($> 99\%$) confidence level are selected as initial targets. The dark cloud candidates are then chosen on the basis of their abnormal red colour and an absence of counterparts in SIMBAD. In this Section we briefly describe the appearance of the G111.80+0.58 region in MSX, 2MASS and FCRAO data. Details of interest for the individual target positions which were selected for single pointing observations (see Sec. 5.4.3) are discussed in Section 5.6.5.

We selected this region specifically for a follow-up study because it was identified as an excessively red, filamentary region in a pilot-survey covering blindly about ten square degrees in the second Galactic quadrant. The colour scaling in the images in Figure 5.1 shows the MSX 8 μm emission toward the location of the complex and its immediate surroundings. The two prominent emission regions labelled A and B correspond to NGC 7538 and S159, respectively. The weaker emission near label C is associated with several masers and radio sources. The outlined region depicts the area mapped in $C^{18}O$ (Fig. 5.2). The target positions for single pointing observations (Table 5.1) are indicated by the black open stars. Compared to the active regions in the field, only faint 8 μm emission ($< 5 \times 10^{-6}\,\mathrm{Wm^{-2}sr^{-1}}$) is associated with this area. Within the box, several IRAS sources are present, indicated by the red stars.

The blue contours in the top left image of Figure 5.1 display the red tail of the $H - K_S$ colours of stars observed in 2MASS on an oversampled $30'' \times 30''$ grid. The solid and dashed contour represent the values 0.52 and 0.68 mag, respectively. Assuming that the $H - K_S$ colours are related to the extinction they can be analysed using the Near Infrared Colour Excess technique (e.g., Lada et al. 1994). The near-IR extinction in a cell is then given by

$$< E(H-K_S)_{\rm cell} >= \frac{\sum_{i=1}^{N} E(H-K_S)_i}{N} \quad , \tag{5.1}$$

where the summation is over N stars present in a grid-cell. The colour excess $E(H - K_S)_i$ per star is the difference between the observed colour and the intrinsic colour, where the latter is derived from an off-position chosen to represent the colour distribution free of extinction. Note that foreground stars will play a significant role and reduce the average reddening per cell at large cloud distances. A correction for this, e.g., by comparing with the off-position, is required to determine the extinction accurately. This is the main reason why the identification is based on a statistical colour distribution instead of the colour excess, because a priori a distance to the objects is unknown and off-positions were not chosen while processing the entire Outer Galactic Plane. Keeping this in mind and adopting an intrinsic $H - K_S$ value of 0.14 mag, the contour values correspond to ~ 6 and ~ 8.5 mag extinction, for convenience converted to A_V using a standard extinction law (i.e., A_V=15.9$\times < E(H - K_S)_{\rm cell} >$; Rieke & Lebofsky 1985). The peak extinction that is measured this way corresponds to ~ 15 mag in A_V. Note that these values are similar to those reported for Inner Galaxy IRDCs using the same colour excess method (e.g., G48 toward W51 with peak $A_V \sim 10-20$ mag; Shipman et al. 2003).

The contours in the top right image of Figure 5.1 give a measure of the 2MASS stellar distribution. The mean distribution of the 2 by 2 square degree surrounding field is ~ 8 stars per $60'' \times 60''$ cell with a 1σ spread of 3 stars. The red contours depict the regions deficit in stars (4 and 3 stars per cell) whereas the blue contours show a surplus (11 and 13 stars per cell). The star counts are also related to the extinction along the line of sight, but here, a direct translation is difficult because they represent data from an incomplete 2MASS catalogue, i.e., the Point Source Catalog including the faint extension. Therefore, they merely give an indication of the stellar distribution and the number of stars that is used for the identification and colour excess method.

Based on the 2MASS data, four different appearances can be distinguished in the area of interest and may be explained intuitively by the following:

1) The combination of colour excess and a deficit in star counts. The measured extinction is due to background and, if present, embedded stars and the column of foreground material is large resulting in fewer background stars compared to the off-position.

2) The combination of colour excess and a surplus in star counts. The measured extinction is due to background and embedded sources. The embed-

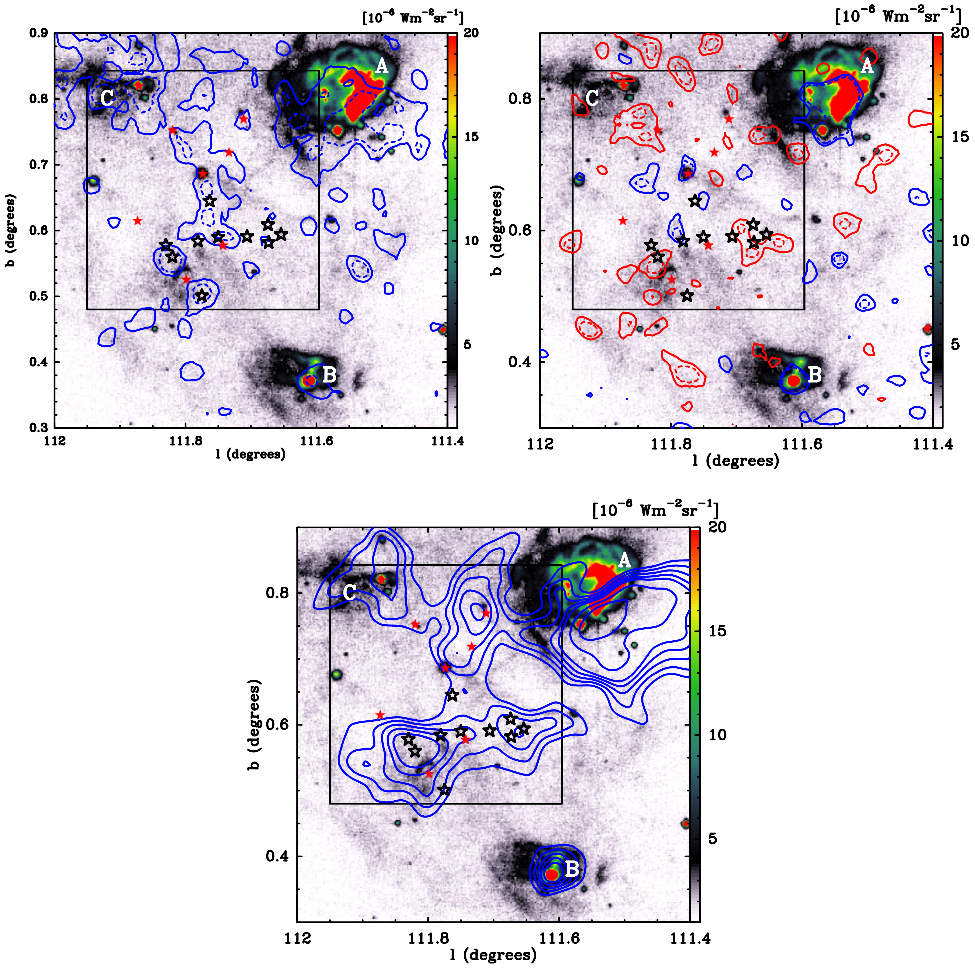

Figure 5.1: The colour scales in the three panels represent the 8 μm emission of the region toward G111.80+0.58. The two prominent sources labelled A and B are NGC 7538 and S159, respectively. Region C is associated with several masers and radio sources. The region of interest for the current work is outlined by the box and is mostly devoid of bright 8 μm emission. The black open stars represent the target positions (Table 5.1) where we conducted single pointing observations. The red filled stars correspond to IRAS point sources. – *Top left* – The solid and dashed contours represent the $H - K_S$ colour distribution, corresponding to 0.52 and 0.68 mag, respectively. – *Top right* – The 2MASS star count distribution on a $60'' \times 60''$ grid. Red dashed and solid contours correspond to 3 and 4 stars per cell, respectively. Blue dashed and solid contours correspond to 13 and 11 stars per cell, respectively. The average star count per cell is 8. – *Bottom* – The contours represent the integrated CO emission between -45 and -60 km s^{-1} as observed in the FCRAO survey. The contours range from 60 to 100 K km s^{-1} in steps of 10 K km s^{-1}.

ded objects result in an enhancement in the star count distribution.

3) Only star count contours. A large column of material prevents the observation of sufficient background reddened stars resulting in a decline of the stellar distribution. The average colour distribution is normal either due to a complete absence of red background stars or due to the presence of too many foreground stars.

4) Only colour excess contours. Red background and embedded sources account for the average red colour and the embedded sources may compensate for the deficit of background stars due to the extinction.

Note that S159 and NGC 7538 both show up as reddened regions and have a surplus of stars, as can be expected for these active star forming regions where multiple embedded sources are present.

G111.80+0.58 is not an entirely unknown object. It was identified in the FCRAO survey and catalogued as part of a molecular cloud (Brunt et al. 2003). The blue contours in the bottom image of Figure 5.1 display the CO data integrated approximately between -45 and $-60\,\mathrm{km\,s^{-1}}$. The cloud is in velocity space as well as in projection on the sky part of a large star forming molecular cloud complex in the Perseus spiral arm which also includes the aforementioned regions NGC 7538 and S159. The kinematic distance to the G111.80+0.58 complex, assuming a flat rotation curve and the IAU standard constants $V_\odot = 220\,\mathrm{km\,s^{-1}}$ and $R_\odot = 8.5\,\mathrm{kpc}$, is $\sim 5.0\,\mathrm{kpc}$. S159 has a similar central velocity ($-56\,\mathrm{km\,s^{-1}}$) as the object presented in this paper. However, a distance of 3.1 kpc was reported by Brand & Blitz (1993) for this cloud, based on spectro-photometric observations of associated stars. Also, the distance to NGC 7538 is generally considered to be less (2.8 kpc; e.g., van der Tak et al. 2000) than the kinematic distance. It appears that this part of the Perseus spiral arm is actually closer to us than suggested by the radial velocity. For the analysis in this paper we adopt a distance of $3.1 \pm 0.2\,\mathrm{kpc}$, but this may be scaled accordingly.

More extensive details on the identification of candidate IRDCs in the Outer Galactic Plane are given in FS07, but the spectroscopic data presented in this paper indeed confirm the presence of a filamentary molecular cloud complex at the identified position.

5.3 Observations

The observations presented in this paper were carried out with the Effelsberg 100-m telescope in Germany and the IRAM 30-m telescope in Spain early 2005. An overview of the observed positions and the main parameters of the observed lines are given in Tables 5.1 and 5.2.

Table 5.1: Source list

Name	l (°)	b (°)	S^a ($\frac{D}{3.1}$ pc)
G111.80+0.58	111.80	0.575	
P1	111.65	0.59	1.04
P2	111.67	0.58	0.80
P3	111.67	0.61	1.14
P4	111.71	0.59	0.77
P5	111.75	0.59	1.01
P6	111.76	0.65	1.01
P7	111.78	0.50	0.90
P8	111.78	0.58	1.19
P9	111.82	0.56	0.60
P10	111.83	0.58	1.13
S159 (reference)	111.61	0.38	0.60

[a]Size of the corresponding core (see Sec. 5.5.2), derived from the $C^{18}O$ map displayed in Fig. 5.2 and assuming a distance D of 3.1 kpc, where D is adopted from S159 (Brand & Blitz 1993).

Table 5.2: Line parameters

Line		Frequency (GHz)	HPBW ($''$)	T_{sys} (K)	F_{eff}[a]	B_{eff}[b]
^{13}CO	1-0	110.201	22.5	100-200	0.95	0.75
	2-1	220.399	11.2	400-900	0.91	0.77
$C^{18}O$	1-0	109.782	22.5	110-200	0.95	0.75
	2-1	219.560	11.2	200-600[c]	0.91	0.77
$C^{34}S$	2-1	96.413	25.5	115-135	0.95	0.55
NH_3	1,1	23.694	40	120-400	-	0.58
	2,2	23.723	40	120-400	-	0.58
	3,3	23.870	40	120-400	-	0.58

[a]Forward efficiency, only for IRAM observations
[b]Beam efficiency
[c]200 – 350 K for the map, 400 – 600 K for single pointing observations

5.3.1 Effelsberg 100-m observations

Single pointing observations of the NH_3 (1,1), (2,2) and (3,3) inversion transitions were performed using the Effelsberg 100-m telescope of the Max-Planck-Institut für Radioastronomie to assess the gas kinetic temperatures at the positions listed in Table 5.1. The first set of data were taken under reasonable winter conditions in January and February 2005 using the 18 – 26 GHz frontend in position switch mode. The receiver was tuned to a central frequency of 22 GHz and the auto-correlator with 2 sub-units of 20 MHz bandwidth covered the 3 transitions simultaneously. After smoothing the data the spectral resolution was $\approx 0.2\,\mathrm{km\,s^{-1}}$. At the 100-m telescope, no chopper wheel calibration is available, so that the atmospherical opacity and the gain response of the receiver need to be calibrated with photometric references. The details of the procedure used to calibrate our data are given in Appendix A. The resulting system noise temperatures are of order 120 – 400 K. A beam efficiency of $\eta = 0.58$ is used to convert the antenna temperature T_A^* to the main beam temperature T_{mb}. Additional data were taken in the following months and calibration was performed using a position observed in the first run. Data reduction was done using the CLASS package (Forveille et al. 1989). For the analysis of the kinetic temperature the absolute scaling is not a concern because it depends only on the ratio of the hyperfine (1,1) lines and the (1,1) to (2,2) brightness temperature ratios. The spectra are displayed in Figures 5.7, 5.8 and 5.9 in Appendix 5.B.

5.3.2 IRAM 30-m observations

Observations at the IRAM-30m telescope were conducted under excellent winter conditions (zenith opacity at 220 GHz $\lesssim 0.05$) in February 2005. A fully-sampled map of $18' \times 18'$ in $C^{18}O$ 2-1, covering the main complex, was obtained using the HERA multi-beam instrument (Schuster et al. 2004). The corresponding SSB receiver and system temperatures were $\approx$100 – 250 K and $\approx$ 200 – 350 K, respectively. The on-the-fly observing mode was used to allow continuous data acquisition as the antenna was moving, with a scanning velocity of $1''\,\mathrm{s^{-1}}$. Frequency-switching mode was used to subtract the sky background contribution. The HERA matrix projected on the sky was rotated by 9.6° to provide a 4″ spatial sampling in both directions. Maps were done in lambda and beta directions to minimise striping effects due to temporal drifts. Each spectrum has 896 channels of 80 kHz or $0.1\,\mathrm{km\,s^{-1}}$ width thanks to the VESPA autocorrelator facility backend. Data were reduced using the `GILDAS` software[†]. The bandpass of the system was removed from each spectrum prior to folding, by subtracting a low-order (≤ 3) polynomial. The spectra were then resampled on a 6″ grid by Gaussian convolution with a final rms of 0.17 K in each $0.1\,\mathrm{km\,s^{-1}}$ channel.

In addition, pointing observations were performed toward the integrated intensity peaks in $C^{18}O$ 1-0 and 2-1 (for column density), ^{13}CO 1-0 and 2-1 (for temperature) and $C^{34}S$ 2-1 (as a high density tracer). The receivers were connected to an autocorrelator with a resolution of 80 kHz resulting in velocity channels of 0.2 – 0.25 and $0.1\,\mathrm{km\,s^{-1}}$ at 3 and 1.3 mm, respectively. The rms noise levels are of the order of 0.3 and 0.5 K at 3 and 1.3 mm, respectively. The absolute calibration to obtain the

[†]URL: `http://www.iram.fr/IRAMFR/GILDAS/`

main beam temperature $T_{\rm mb}$ involved a standard conversion of the antenna temperature $T_{\rm A}^{*}$ using the forward and beam efficiencies listed in Table 5.2. The observed intensities, and hence all the derived parameters, are overestimated due to a contribution of the emission present in the error beam. We adopt a very conservative estimate for this contribution of 20%.

5.4 Observational properties

5.4.1 Spatial distribution: $C^{18}O$ 2-1 map

The high-resolution ($\sim 12''$) intensity map of the $C^{18}O$ 2-1 transition (integrated between -48 and $-56\,{\rm km\,s^{-1}}$) is displayed in Figure 5.2. The $C^{18}O$ molecule, being optically thin under typical ISM conditions, traces the gas column along the line of sight and reveals the filamentary structure in great detail. Several high column density regions are identified along the filaments and a number of these were selected for single pointing observations (P1 – P10). The extend of the $C^{18}O$ emission in the map is used to determine the size of the cores (Sec. 5.5.2).

The reddening contours derived from 2MASS, displayed in Figure 5.1 (top left), show a similar structure, but they do not trace the $C^{18}O$ everywhere. This can be explained by both a lower resolution and the limitations of the colour excess method, which relies completely on the presence of background and embedded red objects along the line of sight. If the extinction is too high, no red background sources are detected and the method fails. However, in such a case, a decrease in star counts (Figure 5.1 top right) can be expected and indeed this is seen for the regions near P1, P2, P3 and P4.

Filamentary structure is frequently observed in IRDCs (e.g., Carey et al. 1998; Johnstone et al. 2003) and is predicted by theories of cloud evolution and clump formation (e.g., Klessen et al. 2004).

In this paper we focus on the physical properties of a number of $C^{18}O$ intensity peaks, indicated by the open stars and corresponding to the positions listed in Table 5.1. The filled red stars represent the location of IRAS point sources in the region. Except for P5 and possibly P9 and P10 (see Section 5.6.5), the IRAS sources do not coincide or appear to interact with any of the target intensity peaks and though they may be associated with the complex, their connection is not considered further in the work presented here.

5.4.2 Velocity distribution: $C^{18}O$ 2-1 channel maps

Though it is beyond the scope of this work to fully analyse the velocity maps of the region it is worth showing the spectral velocity channels to reveal the complexity and different components present in the region. The velocity maps are given in Figure 5.3 and below we list the characteristic features that can be identified:

a) the horizontal structure just below the centre (e.g., at $-51.5\,{\rm km\,s^{-1}}$) containing several of the observed positions (P4, P5, P8, P10);

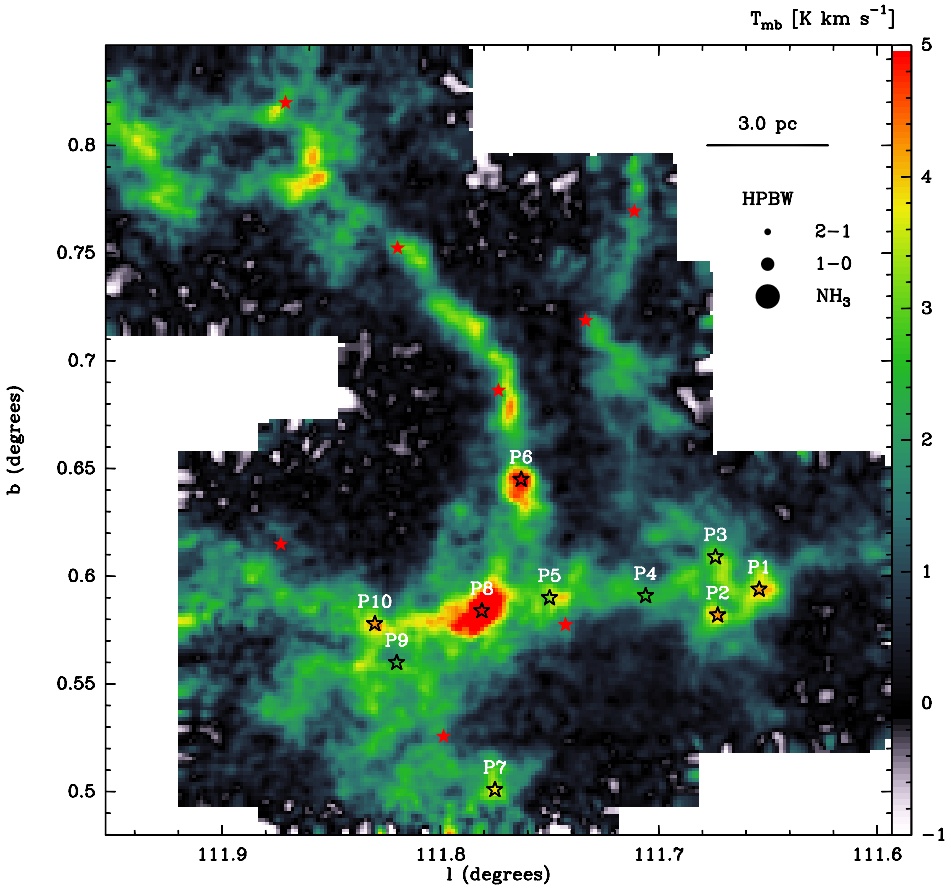

Figure 5.2: This figure shows the $C^{18}O$ 2-1 map of the filamentary dark cloud complex G111.80+0.58 observed with the HERA instrument on IRAM, integrated between -56 and $-46\,\mathrm{km\,s^{-1}}$. The cores listed in Table 5.1 are given and correspond to the positions indicated by the open black stars, where additional single pointing observations were conducted. The filled red stars represent the IRAS point sources. The linear scale is indicated assuming a distance of 3.1 kpc. The approximate half-power-beam-widths (HPBW) represent the ^{13}CO and $C^{18}O$ 2-1, the $C^{34}S$ 2-1, ^{13}CO and $C^{18}O$ 1-0 and the NH_3 beams, respectively.

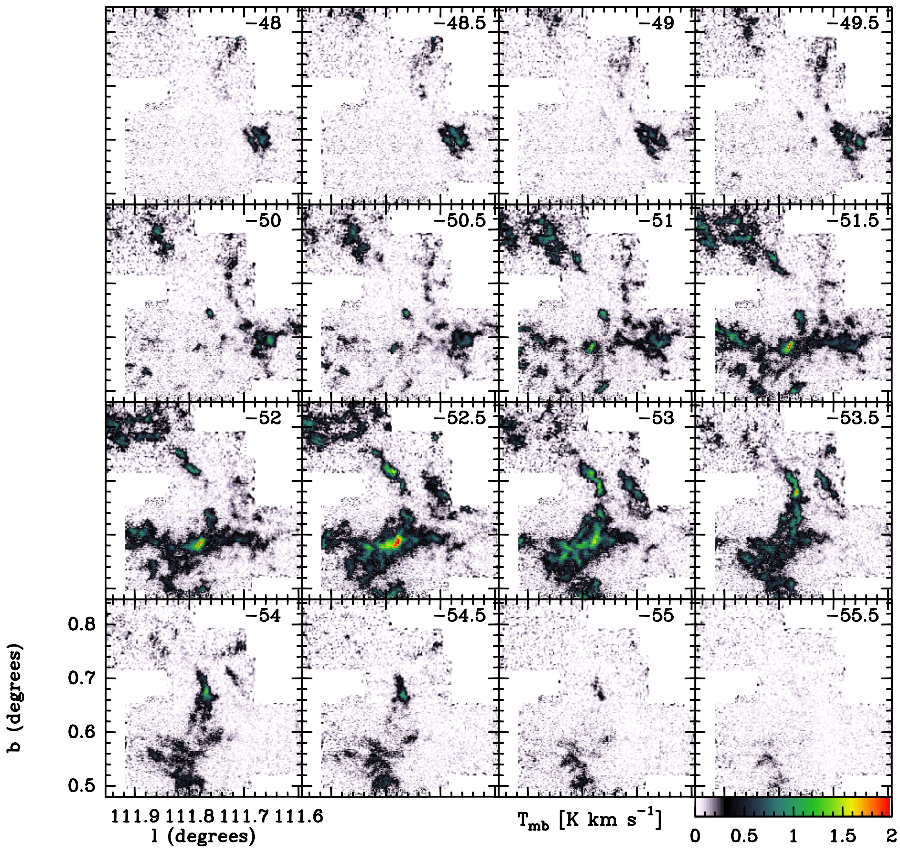

Figure 5.3: This figure displays the velocity channels centred on the velocities given in the upper right corners in the range between -48 and $-55.5\,\mathrm{km\,s^{-1}}$ and integrated over $0.5\,\mathrm{km\,s^{-1}}$. The region shows a complex velocity distribution and several main features can be identified (see text).

b) the curved, vertical structure (e.g., at $-53.5\,\mathrm{km\,s^{-1}}$) containing position P6 and moving up at nearer velocities;

c) the main intensity peak (corresponding to P8), possibly enhanced in intensity because of the superposition of the filamentary structures mentioned above, though the core itself is seen already at $-51\,\mathrm{km\,s^{-1}}$;

d) the positions of P1, P2 and P3 on the right side are dominant at the nearest velocities (-48 to $-51\,\mathrm{km\,s^{-1}}$) and appear to be the end of the horizontal structure, bending toward us;

e) the structures in the upper left corner, where no target positions are located, may be connected with the vertical curved structure.

5.4.3 Single pointing

The observed spectra of ^{13}CO, C^{18}O and C^{34}S toward the main C^{18}O 2-1 intensity peaks in the map are presented in Appendix 5.B. Furthermore, the Gaussian components that were fitted using the `GILDAS` software are displayed as dashed lines. Some positions have additional components in the CO lines that do not correspond to a C^{34}S detection. The focus of this paper however, is on dense cores, i.e., cores that do have a C^{34}S detection. Therefore, the apparently lower density components, likely associated with lower density cores, cloud envelopes or specific phenomena such as outflows are not included in the analysis.

We used the following approach to define the dense components; 1) Gauss-fitting the C^{34}S with N components, 2) Gauss-fitting the C^{18}O and ^{13}CO species with at least N lines, 3) imposing as constraints the positions that correspond to the C^{34}S fits. The different components are numbered according to increasing central velocity (Column 2, Table 5.3, Appendix 5.A). Some of the ^{13}CO lines show high optical depth effects and are impossible to match in velocity with the optically thin lines. In that case fits are produced with the central velocity as a free parameter. Hence the C^{18}O is used to determine the column densities and masses.

5.5 Results: Physical properties of the clouds

The physical characteristics of the cores that are determined from the molecular lines are listed in Tables 5.3 and 5.4 in Appendix 5.A. The integrated properties (column density and derived parameters) as well as the ^{13}CO temperature are determined by using the Gaussian fits of the individual components. A brief description of the tables and their content is given here. More details on the derivation of the values are presented in the following sub-sections:

Table 5.3- *a*) Physical properties assuming the kinetic temperature given by ^{13}CO. Column (1): Identification number of the cores sorted according to Galactic coordinates.

Column (2): Identification number n of the component along the line of sight; corresponds to the n^{th} component in the spectra counting from the left, where n is the same for the different molecules if they have a similar central velocity. Note that only those components that correspond to $C^{34}S$ emission are part of the analysis and only these are listed.
Column (3): Kinetic temperature $T_{\rm kin}$ (K) derived from ^{13}CO.
Column (4-5): Column density (in units of 10^{14} cm^{-2}) of the CO molecules assuming LTE and optically thin emission. In brackets the optical depth $\tau_{\rm c}$ at the line centre is given. Note that the ^{13}CO emission is in general optically thick in dense cores and for some positions only a lower limit could be determined for both $\tau_{\rm c}$ and $N_{\rm mol}$.
Column (6): Column density (in units of 10^{21} cm^{-2}) of H_2 derived from the $C^{18}O$ emission using a standard abundance of 1.67×10^{-7} (Frerking et al. 1982).
Column (7): Average H_2 volume density (in units of 10^2 cm^{-3}) derived from the H_2 column and using the size.
Column (8): LTE Mass ($M_\odot$) given by Equation 5.9 assuming a constant volume density and using the size from Table 5.1.

Table 5.3- *b*) Physical properties assuming the kinetic temperature given by NH_3.
Column (1-2): Same as part *a*.
Column (3): Kinetic temperature $T_{\rm kin}$ (K) derived from NH_3.
Column (4-8): Same as part *a*.

Table 5.4) Line-widths and mass characteristics derived from the IRAM data.
Column (1-2): Same as Table 5.3.
Column (3-5): Line-width (FWHM) of the observed molecules. The ^{13}CO and $C^{18}O$ values are an error-weighted mean of the 1-0 and 2-1 transitions.
Column (6): The error weighted mean FWHM of the optical thin $C^{18}O$ and $C^{34}S$ lines that is used to derive the virial mass.
Column (7): Virial mass ($M_\odot$) as given by Equation 5.10 assuming a constant volume density $n(H_2)$ and using the line-width ΔV given in Column 6.
Column (8): LTE mass ($M_\odot$). Same as Column (8), Table 5.3-a. Listed here for comparison with the other masses.
Column (9): Thermal Jeans mass as given by Equation 5.11.
Column (10): Thermal over gravitational energy ratio η as given by Equation 5.12.

5.5.1 Kinetic temperatures

The kinetic temperature of the cores can be estimated from both the NH_3 and the ^{13}CO lines. In general, considering the conditions in dense cores, collisions dominate the excitation process and the levels are thermalised. In this case, the kinetic temperature equals the excitation temperature, i.e., $T_{\rm kin} = T_{\rm ex}$. A brief description of the determination of $T_{\rm ex}$ for both molecules is given below.

A comparison between the temperatures derived from NH_3 and ^{13}CO can be misleading because they likely represent different regions within the cores. NH_3 is a good temperature tracer and because the molecules do not freeze out onto the dust grains for densities below $\sim 10^6$ cm^{-3} (Bergin & Langer 1997) they are observed even in very dense regions. In the inner, dense parts of cores the heating is due to

cosmic rays and, if present, internal sources. The ^{13}CO molecule is likely depleted in dense and cold cores and it is optically thick due to its much larger abundance. Thus it traces mostly the outer parts of molecular clouds where heating is due to the interstellar radiation field penetrating the outer layers.

Ammonia

The rotational temperatures of the NH_3 molecule, characterising the level populations, were determined by fitting the main and hyperfine components of the (1,1) transition and the main component of the (2,2). The reduction of the (1,1) transition was done using 'METHOD NH3(1,1)' in CLASS to fit the hyperfine structure, whereas for the (2,2) line a standard Gauss fitting procedure was sufficient. A detailed description of the standard analysis is given by Bachiller et al. (1987). The kinetic temperature is derived using the analytical expression given by Tafalla et al. (2004);

$$T_{\rm kin} = \frac{T_{\rm rot}}{1 - \frac{T_{\rm rot}}{42}\ln[1 + 1.1\exp(-16/T_{\rm rot})]}\ ({\rm K})\ , \tag{5.2}$$

where $T_{\rm rot}$ is the rotational temperature. Table 5.5 in Appendix 5.A lists the properties derived from the NH_3 observations. Columns 1 to 4 give the target position, line component, central velocity and line-width (FWHM) of the (1,1) transition, respectively. Columns 5 – 6 and 9 – 10 give the main beam temperatures and the noise of the spectra for the (1,1) and (2,2) transition, respectively. The optical depth τ and the corresponding error derived from the hyperfine structure fitting for the (1,1) transition are listed in Columns 7 and 8, respectively. Typical values for the optical depth are around unity with the exception of P1 and S159 CP2. Note however that the error is of the order of τ itself and the hyperfine fitting is considered dubious. The emission of the hyperfine structure for P2, P6 and P9 CP2, if present at all, is too weak to be detected at the observed signal to noise levels. Hence the missing entries. The rotational temperatures are given in Column 11 with the corresponding error in Column 12. Column 13 and 14 give the kinetic temperatures derived using Equation 5.2 and the corresponding error, respectively. Typically, the kinetic temperatures range from 13 – 30 K. Note that P2 is detected only in the (1,1) transition and P6 not at all, hence the missing entry of a central velocity for the latter. The $T_{\rm mb}$ values for P2 and P6 are derived from the noise of the observations and the temperature parameters merely give an upper limit.

Optically thick ^{13}CO

From basic radiative transfer (e.g., Dickman 1978), the observed radiation temperature for a certain molecule toward a core is given by the expression

$$T_{\rm R}^{*} = [J_\nu(T_{\rm ex}) - J_\nu(T_{\rm bg})][1 - \exp(-\tau_\nu)]\ , \tag{5.3}$$

in which

$$J_\nu(T) = \frac{h\nu}{k}\frac{1}{\exp(\frac{h\nu}{kT}) - 1}\ . \tag{5.4}$$

The constants h, k, $T_{\rm ex}$, $T_{\rm bg}$ and τ_ν are the Planck constant, the Boltzmann constant, the excitation temperature, the background temperature ($\sim$2.7 K) and the optical

depth at frequency ν, respectively. In the dense cores considered in this paper, the ^{13}CO lines are usually optically thick and the results derived in Section 5.5.3 confirm indeed that τ_ν exceeds unity at the line centres. The radiation temperature of the molecule is approximately given by

$$T_R^*(^{13}\mathrm{CO}) = [J_\nu(T_{ex}) - J_\nu(T_{bg})] \,, \tag{5.5}$$

where $T_R^*(^{13}\mathrm{CO})$ is the observed peak intensity of the ^{13}CO line (here we use the 1-0 transition). From this equation the excitation temperature can be derived:

$$T_{ex} = \frac{5.29}{\ln[1 + \frac{5.29}{T_R^*(^{13}\mathrm{CO})+0.868}]} \,(\mathrm{K}) \,. \tag{5.6}$$

The values are listed in Column 3 of Table 5.3-a.
In the following analysis the ^{13}CO 1-0 temperature is adopted as the kinetic temperature of the clouds. When the data allow, the analysis is also performed using the kinetic temperature derived from the NH_3 lines.

5.5.2 Core sizes

We define a size for each core as the average of the minor and major axis of the 50% peak intensity level observed in the C^{18}O 2-1 map. The sizes are given in parsecs in Column 4 of Table 5.1, assuming a distance to the cores of 3.1 kpc. Several positions have multiple components along the line of sight and obviously the size is then determined from a superposition of several cores. However, a distinction between the components is difficult because of the small separation in velocity so that the same size is adopted for all components. Position P9 is not identified as a coherent core in the map and a size of 40″ is adopted. P4 is part of a filamentary structure and the size is assumed equal to the projected width of the filament.

5.5.3 Column densities

The following approach (see e.g., Bourke et al. 1997) assumes these conditions: a) the cores are isothermal, and the kinetic temperature, T_{kin}, is given by the excitation temperature derived from ^{13}CO or NH_3; b) the cores have a constant density; c) the cores are in local thermodynamic equilibrium (LTE). Then, using the observed C^{18}O radiation temperature T_R^* (K), the optical depth can be calculated as a function of the LSR velocity V (km s^{-1}) parameterised by the frequency ν:

$$\tau_V(\mathrm{C}^{18}\mathrm{O}) = -\ln\left\{1 - \frac{kT_R^*}{h\nu}\left[\frac{1}{\exp(\frac{h\nu}{kT_{ex}}) - 1} - \frac{kJ_\nu(T_{bg})}{h\nu}\right]^{-1}\right\} \,. \tag{5.7}$$

The corresponding column density can be estimated using

$$N(\mathrm{C}^{18}\mathrm{O}) = 2.42 \times 10^{14} \sum \frac{\tau_V(\mathrm{C}^{18}\mathrm{O})\, \Delta V\, T_{ex}}{1 - \exp(-\frac{h\nu}{kT_{ex}})} \,(\mathrm{cm}^{-2}) \,, \tag{5.8}$$

where h, ν, k, $J_\nu(T_{bg})$ are the same as before and ΔV is the velocity step size in km s^{-1}. The column densities derived for C^{18}O 1-0 are given in Column 5 of Table 5.3. The

values listed in brackets corresponds to the optical depth, τ_c, at the line centre and are typically much less than unity for $C^{18}O$.

An analogous derivation is done for the ^{13}CO 1-0 transition and these values are listed in Column 4, Table 5.3. However, as noted before, in the dense cores the ^{13}CO is usually optically thick (i.e., $\tau_c > 1$) and the lines cannot be used to determine a reliable column density. Nonetheless, the results are listed and for the cases where the optical depth becomes too large, a lower limit is given. The total molecular column densities, $N(H_2)$, are derived from the $C^{18}O$ 1-0 results using a canonical abundance of 1.67×10^{-7} (Frerking et al. 1982). These values are given in Column 6 of Table 5.3.

5.5.4 Volume densities

Column 7 (Table 5.3) lists the volume density derived from the H_2 column density, assuming the depth of the core equals the size. The density is by definition an average over the actual density profile along the line of sight. In the inner parts of the cores the density is considerably higher, as suggested by the presence of $C^{34}S$.

5.5.5 Mass estimates

LTE mass

Given the size and adopting a constant volume density, the molecular mass derived from the lines, referred to as the LTE mass, is determined using

$$M_{\rm LTE} = \frac{4}{3}\pi\ \mu\ m_{\rm H}\ n({\rm H_2})\ (\frac{1}{2}S)^3{\rm C}\ ({\rm M_\odot})\ , \tag{5.9}$$

where $n(H_2)$ is the volume density, S is the size, m_H is the mass of a hydrogen atom, $\mu = 2.33$ is the mean molecular weight consistent with a 25% mass fraction of helium and $C = 1 pc^3 /\ 1 M_\odot \sim 1.48 \times 10^{22}\ cm^3/\ g$, the conversion to solar masses. The values are listed in Column 8 (Table 5.3). Because the volume density is derived from the column density, i.e., $n(H_2) \sim N(H_2)/S$, the LTE mass of the cores scales with the square of the size and thus the distance ($M_{\rm LTE} \sim S^2$ and $\sim D^2$).

Virial mass

Comparing the LTE mass with the virial mass enables an evaluation of the dynamical state of the cores. Assuming a spherical core with uniform density and considering only thermal and dynamical broadening (neglecting e.g., magnetic fields, internal heating) the virial mass can be derived using the expression (e.g., MacLaren et al. 1988)

$$M_{\rm vir} = 210\ R\ (\Delta V)^2\ ({\rm M_\odot})\ , \tag{5.10}$$

where $R\ (=\frac{S}{2})$ is the radius of the core in pc and ΔV is the FWHM of the line in km s^{-1}. In our case a weighted average of the observed optically thin lines, given in Column 6 of Table 5.4, is used. The resulting virial masses are given in Column 7 of Table 5.4. Equation 5.10 assumes a constant density. The constant may be replaced by 190 or 126 for a density profile given by $\rho \sim r^{-1}$ or $\rho \sim r^{-2}$, respectively.

Jeans mass

Thermal Jeans fragmentation, often referred to as the mechanism to set the mass scale for star formation (Larson 1985), is approximately given by

$$M_{\rm Jeans} \approx \frac{90}{\mu^2} \times T^{\frac{3}{2}} n^{-\frac{1}{2}} \, (\mathrm{M}_\odot) \, , \tag{5.11}$$

where T is the gas temperature and n is the total volume density. The values are listed in Column 9 of Table 5.4. The typical value is of the order of $10\,\mathrm{M}_\odot$, much smaller than the derived LTE masses of the cores. Therefore, structure on much smaller scales may be expected within the cores.

Stability

The energy ratio η listed in Column 10 (Table 5.4) is defined as the thermal energy over the gravitational energy:

$$\eta = \frac{E_{\rm T}}{E_{\rm grav}} = {}^{\frac{3}{2}kT\frac{M_{\rm LTE}}{\mu m_{\rm H}}} \Big/ {}_{\frac{3}{5}\frac{GM_{\rm LTE}^2}{0.5\,S}} \, , \tag{5.12}$$

where $M_{\rm LTE}$ is given in Column 8 (Table 5.4), T is the kinetic temperature listed in Column 3 (Table 5.3-a), S is the size of the core, described in Sec. 5.5.2, μ, $m_{\rm H}$, k and G are the mean molecular weight (= 2.33), the mass of a hydrogen atom, the Boltzmann constant and the gravitational constant, respectively. Typically, η is much less than unity and it suggests that the thermal energy by itself is insufficient to support the cores against gravitational collapse.

5.6 Discussion and conclusion

What kind of object is G111.80+0.58?
Before we attempt to answer this question it is worthwhile to discuss some key properties derived from the observations and compare the results with other studies.

5.6.1 Gas temperature

The gas temperatures derived from NH_3 (13 – 20 K) and, less obvious also from ^{13}CO (7 – 14 K), are higher than expected inside molecular cores if only cosmic ray ionisation is considered as a heating source (a mean Galactic value of $\zeta_{\rm CR} \sim 3 \times 10^{-17}$ s^{-1} yields a temperature of $T \sim 8 - 10$ K, van der Tak & van Dishoeck 2000). The NH_3 temperatures suggest that deep inside the cores additional heating sources are present. Because the ^{13}CO is usually optically thick at the observed positions, it traces the temperature of the material at an optical depth of about unity. The actual location of this $\tau = 1$ surface in the cores cannot be determined, but it is likely that the two molecules trace the temperatures at different depths in the cores.

The derived temperatures are in agreement with values found for massive and dense cores (e.g., < 20 K for IRDCs, Carey et al. 1998). The temperature found for S159 is significantly higher (29 K), which is consistent with its more advanced star forming state.

5.6.2 Core masses and total mass

The individual core masses ($M_{\rm LTE}$) vary from about 20 to 1000 $M_\odot$ (approximately 100 – 600 $M_\odot$ for $M_{\rm vir}$) with an average of around 190 $M_\odot$ (about 280 $M_\odot$ for $M_{\rm vir}$). Most cores are massive when compared to low-mass dark clouds (e.g., Evans 1999, and references therein), but correspond well with masses found for high-mass protostellar objects (HMPOs; e.g., Williams et al. 2004). The LTE mass we find for S159 is in agreement with previous high resolution studies (Lebrón et al. 2001) where the core is resolved into multiple substructures.

A rough estimate for the total mass of the complex, including only the observed cores in this paper, is 3000 $M_\odot$ (about 4500 $M_\odot$ for $M_{\rm vir}$). This is comparable to masses found for Inner Galaxy IRDCs (e.g., Carey et al. 2000).

5.6.3 Physical characterisation of the cores

The observations suggest that the thermal energy is insufficient to support the cores against gravitational collapse. Additional support is seen in the observed line-widths toward the cores. These are much broader than expected from purely thermal motion (see Column 3 – 5, Table 5.4 and Column 4, Table 5.5). The average line-width is about 1.8 ± 0.4 km s^{-1}. The sound speed $\Delta V_{\rm s}$, considering that the cores have a typical temperature T of 15 – 20 K, is given by

$$\Delta V_s = \left(\frac{8\ln(2)kT}{\mu m_{\rm H}} \right)^{\frac{1}{2}} \approx 0.6 \text{ km s}^{-1} , \tag{5.13}$$

and thus the velocities are supersonic.

The broad lines could be due to turbulent motions in the clouds and are indicative of regions of high-mass star formation (e.g., Myers & Fuller 1993), in contrast to mostly thermal broadened lines often seen toward low-mass pre-stellar cores (e.g., Goodman et al. 1998). The line-width across the filament, extending over 10 pc (at a distance of 3.1 kpc), is about 5 km s^{-1}. The relation between velocity dispersion of substructures (ΔV_l) and the velocity dispersion over the larger complex (ΔV_L) in a turbulent medium can be expressed using the empirically derived Larson's law (Larson 1981);

$$\Delta V_l \sim \Delta V_L \left(\frac{l}{L} \right)^{0.38} , \tag{5.14}$$

where L is the size of the filament and l the size of the sub-structure. For a typical core size in our sample of ≈ 1 pc, the expected line-width is then ≈ 2 km s^{-1} for individual cores. The values we find are consistent with this relationship. The standard relations of mass versus line-width are, however, for much smaller cores and the larger cores presented here may be a superposition of such small cores. Extending the relation to smaller cores of 0.1 pc, the expected line-width using Equation 5.14 is about 0.8 to 0.9 km s^{-1}. This is still in agreement with values found for typical massive starless cores (e.g., Caselli & Myers 1995).

A decay of the turbulence is expected on short time-scales (see Ballesteros-Paredes et al. 2006, for a review on star formation and turbulence) and some mechanism is needed to sustain the turbulent support. Internal sources, e.g., deeply embedded

YSO's may be present and stir up the material from the inside through outflows. Indicative of the presence of a heating source can be the high temperatures traced by NH_3. However, we find no correlation between the line-width and the gas temperature.

The line-width could also be the result of a number of small dense clumps at slightly different velocities within the spatial resolution element of the observations. This idea is supported by the presence of multiple components along the line of sight toward many of the observed positions. In addition, the derived Jeans mass (Column 9, Table 5.4) for the cores is typically $\approx 10\,M_\odot$ and therefore, fragmentation is expected to occur on smaller mass scales compared to the observed core masses, if thermal processes dominate stability. Figure 5.4 shows a plot of the virial mass versus the LTE mass. The virial parameter α can be defined as the ratio of the two

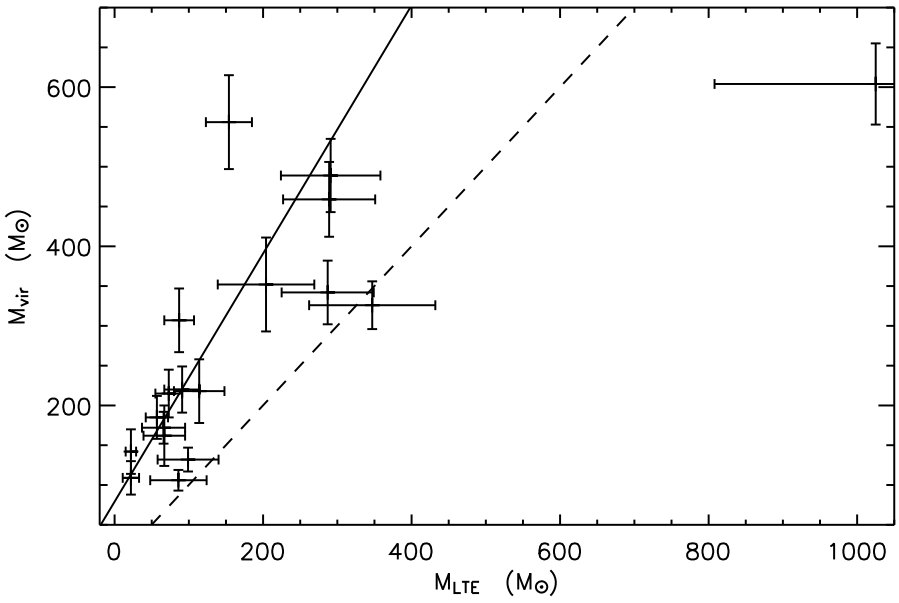

Figure 5.4: The virial mass is plotted against the LTE mass. The dashed line corresponds to equal masses, where the virial parameter $\alpha = 1$. The solid line is the fit to the data points.

and a value of unity corresponds to a virial equilibrium state (dashed line). The observed values for α range from about 1 to 3 and thus suggest that, on a global scale, the cores are close to virial equilibrium. Note that depletion of the $C^{18}O$ molecule may play an important role for densities in excess of $10^4\,cm^{-3}$ if $T_{dust} \sim T_{gas}$ (Bergin et al. 1995) and consequently, the LTE mass could be underestimated. Core P8 is an exceptional case where $M_{LTE} > M_{vir}$. As seen from the channel maps (Fig. 5.3, Sec. 5.4.2), in projection P8 appears to be a superposition of two crossing filaments. The material traced by the $C^{18}O$ may just be the line of sight sum of two components.

Alternatively, because the components have a similar LSR velocity, a collision may be taking place between the two filaments. This would lead to the formation of a dense (perhaps gravitationally unstable) central core. If so, then we may be witnessing this scenario prior to the system being fully virialised.

5.6.4 Star forming activity

The NH_3 lines are very sensitive to the temperature and therefore the presence of the higher transitions, particularly of the (3,3) line, is a good indicator for the occurrence of warmer gas, possibly indicating internal heating sources. The (3,3) line is clearly seen toward S159, as expected from work by Lebrón et al. (2001), and also position P5, where it may result from the presence of the associated IRAS point source. A very weak detection is seen toward positions P8 and P9.

Signatures of self-absorption in the ^{13}CO lines can be an additional indication of the presence of the warmer gas inside the cores. This may explain also the failure in fitting the ^{13}CO lines at the central velocities of the optically thin lines. Most noticeable are the positions toward S159, P5 and P8.

If embedded sources are present, they may have been identified in the 2MASS data. Figure 5.5 shows the $H - K_S$ versus $J - H$ colours of the sources present in the 2×2 square degree field. The grey scaling represents the overall distribution of the field and the majority of the sources are located near the dwarf and giant sequence, indicated by the black solid curves. The spread in the colours is significant but can be addressed entirely by the use of the very faint sources in the 2MASS catalogue (the faint extension) where the photometric errors are larger. The dashed lines give the reddening vectors (Rieke & Lebofsky 1985) for the dwarf and giant sequence and the arrow corresponds to an A_V of 10 magnitudes. In addition, the figure shows for each of the cores the associated 2MASS sources in different symbols. Note that most star colours toward the cores resemble main sequence stars with or without reddening, and these are likely reddened background or 'normal' foreground stars. However, the very red $H - K_S$ area right of the reddening vectors corresponds to colours of proto-stellar objects (e.g., Robitaille et al. 2006). Most promising candidates for YSO's correspond to sources associated with S159, P5 and P8.

5.6.5 Notes on individual cores

P1, P2, P3 and P7: These are regions of the molecular cloud where multiple components with enhanced densities (based on C^{34}S) appear to be present along the line of sight. There are no clear indications for star forming activity from ^{13}CO self absorption, 2MASS colours or NH_3 heating (NH_3 is only available for P1 and P2).

P4: This is part of the horizontal filamentary structure. No clear core is seen in the C^{18}O 2-1 map but high density gas is present, indicated by the C^{34}S line. Gravity may have induced a density enhancement along the filament. Two components are fitted by the software to the spectra, but possibly opacity effects cause a non-Gaussian behaviour of a single component. Manual fitting of one component would result in an LTE mass of about 138 $M_\odot$, a velocity width of 1.8 km s^{-1} and a virial mass of 262 $M_\odot$.

P5: This position may be associated with, and heated by, the nearby IRAS point-source IRAS23137+6105, which can explain the presence of the higher NH_3 transitions. One object in the 2MASS data has typical colours of a YSO. Also here, the spectra suggest that a single manual fit may be favoured to two components. This would result in an LTE mass of about 220 $M_\odot$, a velocity width of 2.57 km s^{-1} and a virial mass of 702 $M_\odot$.

P6: Two dense ($C^{34}S$) components are present along the line of sight. The stellar density appears slightly enhanced but this may be a chance encounter along the line of sight. There is no indication for the presence of YSO's and none of the NH_3 transitions is detected which suggests a quiescent, cold stage.

P8: This is the most profound core in the region and the best candidate for being an object similar to Inner Galaxy IRDCs (see Section 5.6.6). Automatic fitting of the CO lines resulted in two components, but in $C^{34}S$, a single profile is seen. Manual fitting of a single component to the CO lines results in an LTE mass of about 1250 $M_\odot$, a velocity width of 2.28 km s^{-1} and a virial mass of 647 $M_\odot$. This makes the case for being an Outer Galaxy IRDC even stronger. Star formation may have started here, indicated by the NH_3 lines and the presence of YSO candidates in the 2MASS colour plot. Opacity effects such as self absorption due to colder foreground gas can explain the non-Gaussian appearance of the CO lines. The stellar density derived from 2MASS is significantly higher (11-13 stars per cell), compared to the rest of the field.

P9 and P10: There is arc-like MSX 8 μm emission nearby these cores (see Figure 5.1). This may be caused by heating due to radiation from the neighbouring IRAS point-source IRAS23143+6103. Such heating may also explain the detection of NH_3 (2,2) and faint NH_3 (3,3) emission. Compression of the material due to a shock may then lead to the observed high densities. No indication of embedded sources is seen from the 2MASS data.

5.6.6 Conclusion: Is G111.80+0.58 similar to Inner Galaxy IRDCs ?

The global characteristics of the G111.80+0.58 complex that are presented in this paper, such as its size ($\sim$ 10 pc), column density (peak $> 10^{22}$ cm^{-2}) and LTE mass ($\sim$ 3000 $M_\odot$) indicate a clear resemblance to the bulk properties of Inner Galaxy IRDCs (Simon et al. 2006b). However, except for P8, the individual core properties (e.g., size: $\sim$1 pc, LTE mass: 20 – 350 $M_\odot$, density: $10^3 - 10^4$ cm^{-3}) fall short of the values found for compact (sub)mm cores in IRDCs (size: 0.02 – 0.8 pc, mass: 10 – 10^3 $M_\odot$, density: $10^3 - 10^7$ cm^{-3} Rathborne et al. 2006).

Would this cloud be seen in extinction were it observed toward a bright mid-IR background?

A typical molecular column density found for the cores is $10 - 20 \times 10^{21}$ cm^{-2}, which corresponds to an A_V of 10 – 20 mag (Bohlin et al. 1978). The corresponding extinction at 8 μm can be expressed as $A_{8\mu m} \sim 0.04 A_V < 0.4$ mag, using conversions

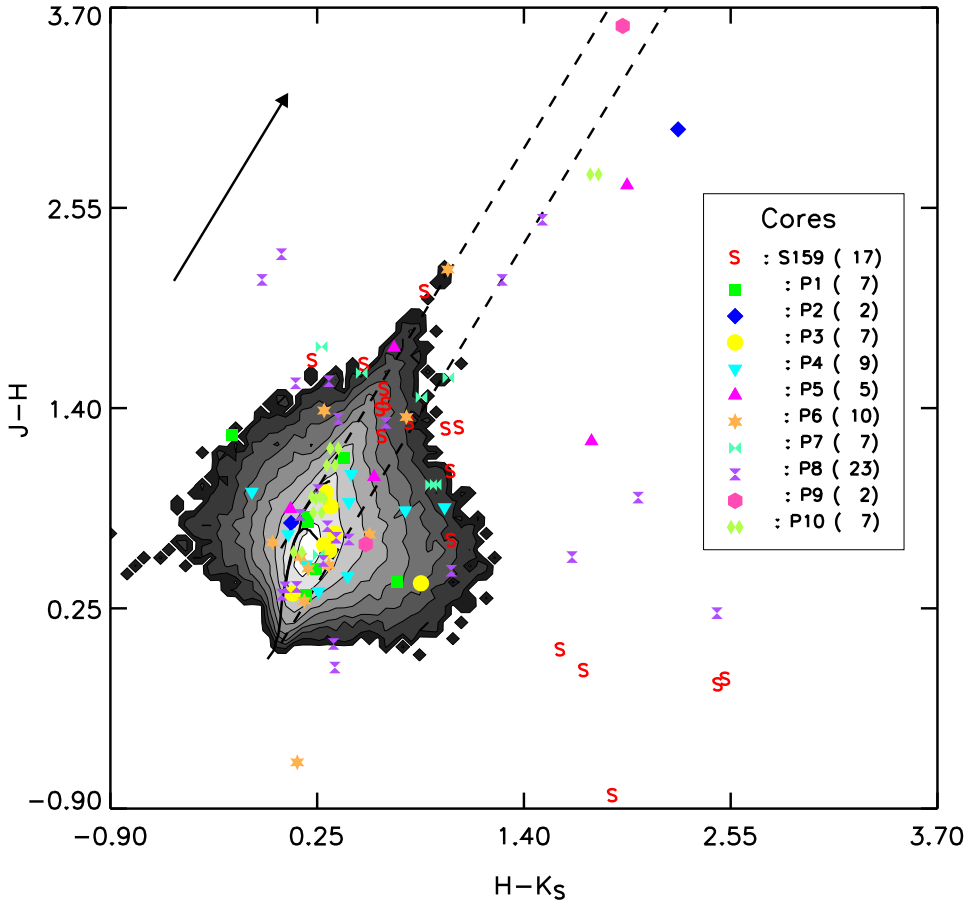

Figure 5.5: This figure shows the 2MASS colour-colour plot of stars in the direction of G111.80+0.58. The grey-scales represent the location of colours of all stars in the 2 by 2 square degree field. Lighter colours correspond to a higher occurrence. The majority of the stars are situated with some spread around the dwarf and giant sequences overlaid as black curves. The arrow corresponds to a visual extinction of 10 magnitudes, in the direction of the reddening vectors (dashed lines, Rieke & Lebofsky 1985). The sources associated with the cores are plotted using the symbols listed in the legend. The number of associated sources is given in brackets.

adopted from Indebetouw et al. (2005) and Rieke & Lebofsky (1985). Typical extinction measurements at 8 μm for Inner Galaxy IRDCs show values in excess of 1 mag (Carey et al. 2000). Thus, based on this simple reasoning the cloud would not meet the IRDC criterion of mid-IR extinction. However, following the same analysis, the extinction toward position P8 ($N_{H_2} \approx 7 \times 10^{22}$ cm^{-2}) is about 2.8 mag at 8 μm. Con-

sidering that the above values represent the densest component of the two CO fits toward P8, the actual 8 μm extinction is even higher when using a single fit (> 3 mag). This central part of the cloud makes the region a very promising Outer Galaxy IRDC candidate. The presence of possible embedded heating sources at this position may indicate that the core is not in a very early, quiescent state, but already forming stars. Recent studies (Rathborne et al. 2005; Ormel et al. 2005, v.d. Wiel, privat comm.), using sub-millimetre and Spitzer data indicate that some Inner Galaxy IRDCs are presently forming stars in their cores and along the filaments as well.

Obviously, the dark cloud candidate presented in this paper is in the vicinity of star forming activity (NGC 7538, S159) and in that sense the boundary conditions may not be that deviant from Inner Galaxy IRDCs. It should be noted however, that there are environmental differences in the Outer Galaxy (e.g., radiation field, density, abundance; Brand & Wouterloot 1995; Rudolph et al. 2006, and references therein) when compared to the inner spiral arms and the Molecular Ring, where most of the IRDCs are found.

The super-thermal line-widths and the presence of massive, cold and dense cores in G111.80+0.58 are both indicative of a high-mass star forming complex. The combined mass of the cores is perhaps too low to form a massive star cluster (like Orion). However, this region is part of a much larger molecular cloud complex. We conclude that the G111.80+0.58 complex likely belongs to a category of objects similar to intermediate-mass IRDCs (e.g., IRDC G48 toward W51; Ormel et al. 2005) in an early, but not pristine stage of star formation.

5.7 Concluding remarks

Radiative transfer codes can provide a better understanding of the properties of the gas, e.g., radial density and temperature profiles can be investigated, but require more detailed observations. We did conduct tests with a multi-zone escape probability code (β 3D, Poelman & Spaans 2006, 2005) and these resulted in similar temperature, density and mass estimates as presented in this paper. We therefore conclude that for the integrated properties these codes have no additional contribution to the results. The main advantage when using these models is getting a better understanding of the line profiles. In particular, effects such as self absorption or velocity structures, like infall motion may explain some of the double peaked and non-Gaussian features (see e.g., Evans 1999). In the work presented here, non-Gaussian features are treated as separate components. Note in this respect that different optically thin lines (e.g., $C^{18}O$ and $C^{34}S$ for core P1) show their peak emission at opposite sides of the central velocity $V_{\rm LSR}$.

High spatial and spectral resolution in addition with radiative transfer models are required in the future to get better constraints on the physical properties on smaller scales. A spatial resolution at sub-arcsecond scales may resolve the presence of small high density clumps. Resolving this substructure will allow an investigation of the Dense Clump Mass Function (DCMF). It is of great importance to conduct these studies to put constraints on the origin of the stellar mass spectrum. Not only in nearby, generally low mass star forming clouds (e.g., Pipe Nebula; Lombardi et al. 2006), but particularly in the more massive and distant IRDCs, including the Outer

Galaxy region presented in this paper.

A different way of characterising IRDCs is by using (sub)mm continuum observations. All Inner Galaxy IRDCs show strong sub-millimetre emission (e.g., Carey et al. 2000) and some contain bright, centrally peaked cores. In addition, these data allow an independent measurement of properties such as temperature, mass and luminosity. It will be worthwhile to observe the G111.80+0.58 cloud in dust continuum and compare the data with the molecular line results presented here and with existing sub-millimetre studies in the Inner Galaxy.

5.A Calibration of the 100-m telescope data

At the frequency considered here (23 GHz), the Effelsberg telescope offers a calibration based on noise diodes, so that the received signal is not converted into K but into internal receiver counts. In order to both convert the receiver counts into antenna temperature, as well as to correct for the atmospherical absorption, we have observed a photometric calibrator (here NGC 7027) at various elevations in the course of each observing night. This approach is similar to the so-called 'antenna tipping' used to measure the sky opacity during e.g., bolometer observations. The weather conditions were stable enough to assume that the opacity derived through this technique was reasonably representative of the daily set of data. If $\mathrm{F_{int}}$ is the conversion factor between internal counts and Jy above the atmosphere and corrected for backward losses, the measured receiver counts are (in a given spectrometer channel):

$$T_{\mathrm{A}}^{\mathrm{int}} = G(\mathrm{el}) \times \mathrm{e}^{(-\tau_z \mathrm{A})} \, , \times \frac{\mathrm{T_A^*}\, \eta_\ell}{\mathrm{F_{int}}} \tag{5.15}$$

where A is the airmass at elevation el, τ_z the zenith opacity and G(el) the normalised elevation gain. Observing a photometric calibrator of known flux $S_{\nu,\mathrm{ref}}$ one has:

$$T^*_{\mathrm{A,ref}} \quad = \quad \frac{A_{\mathrm{geom}}\, \eta_A}{2k\, \eta_\ell}\, S_{\nu,\mathrm{ref}} = \frac{G_{(\mathrm{K/Jy})}}{\eta_\ell}\, S_{\nu,\mathrm{ref}} \tag{5.16}$$

and

$$\mathrm{Log}\left(\frac{G_{(\mathrm{K/Jy})}\, S_{\nu,\mathrm{ref}}}{T_{\mathrm{A}}^{\mathrm{int}}}\right) \quad = \quad \mathrm{Log}\left(\frac{F_{\mathrm{int}}}{G(\mathrm{el})}\right) + \frac{\tau_z}{\sin(\mathrm{el})} \, . \tag{5.17}$$

Using the calibrated flux published by Ott et al. (1994) and observing the reference at various elevations, the calibration procedure thus consists of fitting the previous expression with a pair of (F_{int},τ), assuming that the opacity has not significantly changed in the course of the observations. The antenna temperature is then given by:

$$T_{\mathrm{A}}^* = \frac{T_{\mathrm{A}}^{\mathrm{int}} \times G_{(\mathrm{K/Jy})} \times F_{\mathrm{int}}}{G(\mathrm{el}) \times \mathrm{e}^{(-\tau_z \mathrm{A})} \times \eta_\ell} \, . \tag{5.18}$$

The NGC 7027 flux at 23 GHz was taken as 5.11 Jy. We derived a conversion gain of 1.86±0.1 and the opacity was around 0.2, consistent with expected atmospherical

transmission in the centimetre domain. Figure 5.6 illustrates the steps involved in the calibration process. It shows the combined effect of antenna gain and opacity for data taken at various elevations. Finally, assuming that our sources emit in a solid angle comparable to the main beam, the derived fluxes are translated into antenna main beam temperatures using the antenna efficiencies provided by the 100-m staff (A. Kraus, priv. comm.).

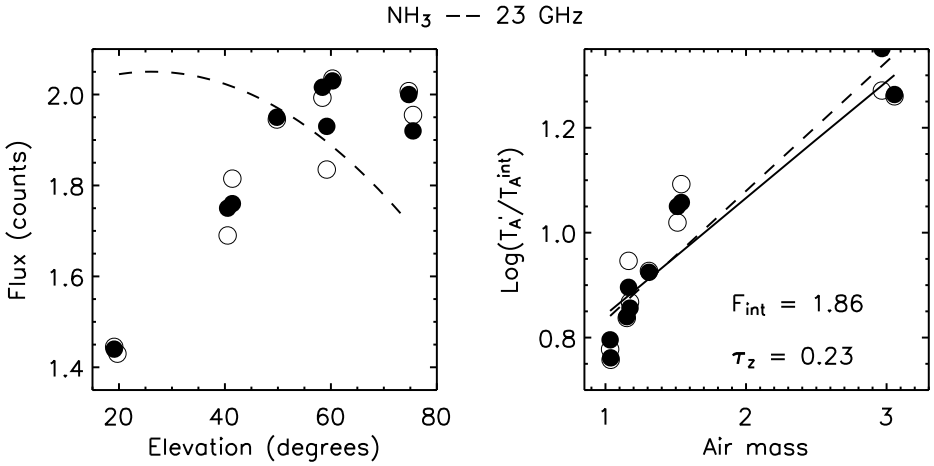

Figure 5.6: Example of an Effelsberg calibration measurements taken on NGC 7027 for one day at the frequency considered here. **Left**: Flux measurements for azimuthal (open circles) and elevation (filled circles) scans. The elevation gain curve is plotted, normalised to the highest flux of the data points. **Right**: Fit to Eq. 5.17 of data points collected during a single day for azimuthal (solid line) and elevation (dashed line) scans. The resulting τ_z and F_{int} are the mean of these two fits.

5.B Tables and spectra

Table 5.3: Physical properties

	ID	CP	T_{kin} $^{13}CO^a$	N_{mol} [τ_c]				N_{H_2}	n_{H_2}	M_{LTE}
				^{13}CO (1-0)		$C^{18}O$ (1-0)		$(\frac{1.67\times10^6}{A}\times$	$(\frac{3.1\text{ kpc}}{D}\times$	$(\frac{D^2}{9.6\text{ kpc}^2}$
(a)			(K)	(10^{14} cm^{-2})		(10^{14} cm^{-2})		10^{21} cm^{-2})	10^2 cm^{-3})	M$_\odot$)
	(1)	(2)	(3)	(4)		(5)		(6)	(7)	(8)
	S159	2	29.1 (±5.1)	1340 (±751)	[1.27]	97 (±31)	[0.09]	58 (±19)	313 (±100)	204 (±65)
	P1	2	10.6 (±1.6)	> 496	[> 4.79]	11 (±4)	[0.11]	6 (±3)	20 (±8)	67 (±28)
	P1	3	9.8 (±1.4)	125 (±29)	[1.44]	45 (±10)	[0.41]	27 (±6)	85 (±18)	287 (±62)
	P2	2	6.8 (±0.9)	> 195	[> 2.88]	23 (±5)	[0.39]	14 (±3)	56 (±13)	87 (±20)
	P2	3	10.2 (±1.5)	589 (±228)	[4.38]	24 (±6)	[0.22]	15 (±4)	59 (±16)	91 (±24)
	P3	1	8.7 (±1.3)	107 (±26)	[2.02]	9 (±4)	[0.14]	5 (±2)	15 (±6)	66 (±29)
	P3	2	13.1 (±2.1)	656 (±547)	[4.51]	38 (±9)	[0.20]	23 (±5)	65 (±15)	291 (±67)
	P4	1	7.5 (±1.0)	51 (±13)	[1.30]	16 (±4)	[0.27]	10 (±3)	41 (±11)	57 (±15)
	P4	2	10.0 (±1.4)	> 488	[> 3.68]	21 (±5)	[0.18]	13 (±3)	53 (±13)	73 (±18)
	P5	2	9.7 (±1.4)	227 (±36)	[1.84]	26 (±5)	[0.19]	15 (±3)	50 (±10)	154 (±31)
	P6	1	12.4 (±1.9)	168 (±53)	[1.54]	17 (±7)	[0.15]	10 (±4)	32 (±13)	99 (±41)
	P6	2	12.1 (±1.9)	> 655	[> 4.60]	48 (±10)	[0.28]	29 (±6)	93 (±20)	289 (±62)
	P7	2	13.2 (±2.1)	199 (±57)	[1.24]	24 (±7)	[0.14]	14 (±4)	52 (±16)	114 (±34)
	P7	3	10.2 (±1.5)	> 318	[> 5.13]	18 (±8)	[0.28]	11 (±5)	39 (±17)	86 (±38)
	P8	2	13.9 (±2.4)	> 625	[> 3.69]	124 (±26)	[0.54]	74 (±16)	202 (±43)	1025 (±217)
	P9	2	9.4 (±1.3)	67 (±18)	[1.00]	10 (±3)	[0.11]	6 (±2)	33 (±11)	22 (±7)
	P9	3	13.0 (±1.9)	250 (±88)	[2.29]	11 (±5)	[0.10]	6 (±3)	34 (±17)	22 (±11)
	P10	3	11.2 (±2.0)	> 389	[> 2.29]	46 (±11)	[0.36]	28 (±7)	80 (±20)	347 (±85)
(b)^b			$T_{kin}(NH_3)$ (K)							
	S159	2	29.3 (±3.4)	1341 (±742)	[1.25]	97 (±25)	[0.09]	58 (±15)	315 (±82)	205 (±54)
	P1	2	14.4 (±2.6)	434 (±108)	[1.50]	12 (±6)	[0.07]	7 (±4)	23 (±11)	76 (±38)
	P2	2	19.0 (±8.4)	149 (±39)	[0.36]	30 (±20)	[0.08]	18 (±12)	73 (±48)	113 (±74)
	P5	2	18.2 (±2.7)	217 (±46)	[0.45]	34 (±9)	[0.08]	20 (±5)	65 (±17)	201 (±53)
	P8	2	16.7 (±1.4)	470 (±159)	[1.63]	131 (±29)	[0.40]	79 (±17)	215 (±47)	1090 (±240)
	P9	2	20.0 (±2.3)	78 (±27)	[0.26]	15 (±7)	[0.04]	9 (±4)	47 (±24)	31 (±16)
	P9	3	18.0 (±2.6)	219 (±92)	[0.90]	13 (±8)	[0.06]	8 (±5)	41 (±26)	26 (±17)
	P10	3	13.5 (±2.1)	435 (±141)	[2.68]	49 (±13)	[0.07]	29 (±8)	84 (±22)	366 (±94)

[a] The kinetic temperature is assumed equal to the excitation temperature.
[b] Part b is the same as part a, except here the kinetic temperature is derived from NH_3. Note that the results are very similar.

Table 5.4: Line-width and mass properties

ID	CP	ΔV				$M_{\rm vir}$	$M_{\rm LTE}$	$M_{\rm Jeans}$	η
		^{13}CO	C^{18}O	C^{34}S	virial				
		(km s^{-1})	(km s^{-1})	(km s^{-1})	(km s^{-1})	($\frac{D}{3.1\ \rm kpc}$ M$_\odot$)	($\frac{D^2}{9.6\ \rm kpc^2}$ M$_\odot$)	(M$_\odot$)	$\left[\frac{E_{\rm T}}{E_{\rm grav}}\right]$
(1)	(2)	(3)	(4)	(5)	(6)	(7)	(8)	(9)	(10)
S159	2	2.84 (±0.01)	2.40 (±0.02)	2.25 (±0.04)	2.36 (±0.02)	352 (±59)	204 (±65)	15 (±5)	0.09 (±0.03)
P1	2	3.00 (±0.06)	1.07 (±0.15)	1.57 (±0.25)	1.22 (±0.13)	162 (±38)	67 (±28)	13 (±4)	0.17 (±0.08)
P1	3	1.77 (±0.08)	1.74 (±0.05)	2.27 (±0.50)	1.77 (±0.06)	342 (±40)	287 (±62)	5 (±1)	0.04 (±0.01)
P2	2	2.19 (±0.02)	1.95 (±0.03)	1.33 (±0.33)	1.91 (±0.04)	307 (±40)	87 (±20)	4 (±1)	0.07 (±0.02)
P2	3	3.98 (±0.02)	1.62 (±0.02)	1.67 (±0.85)	1.62 (±0.03)	220 (±29)	91 (±24)	7 (±2)	0.09 (±0.03)
P3	1	1.34 (±0.02)	1.17 (±0.04)	1.47 (±0.29)	1.20 (±0.05)	172 (±20)	66 (±29)	11 (±3)	0.16 (±0.07)
P3	2	2.91 (±0.02)	2.07 (±0.03)	1.06 (±0.34)	2.02 (±0.03)	489 (±46)	291 (±67)	10 (±3)	0.05 (±0.01)
P4	1	1.28 (±0.02)	1.63 (±0.05)	0.82 (±0.19)	1.51 (±0.05)	185 (±27)	57 (±15)	5 (±1)	0.10 (±0.03)
P4	2	2.52 (±0.02)	1.74 (±0.05)	1.26 (±0.12)	1.63 (±0.05)	215 (±30)	73 (±18)	7 (±2)	0.11 (±0.03)
P5	2	2.83 (±0.02)	2.25 (±0.04)	2.62 (±0.24)	2.29 (±0.05)	556 (±59)	154 (±31)	7 (±2)	0.07 (±0.02)
P6	1	1.49 (±0.01)	1.14 (±0.03)	0.96 (±0.16)	1.12 (±0.03)	132 (±15)	99 (±41)	13 (±4)	0.13 (±0.06)
P6	2	2.88 (±0.01)	2.09 (±0.02)	1.20 (±0.01)	2.08 (±0.03)	459 (±47)	289 (±62)	7 (±2)	0.04 (±0.01)
P7	2	1.91 (±0.02)	1.49 (±0.11)	1.62 (±0.30)	1.52 (±0.11)	218 (±40)	114 (±34)	11 (±3)	0.11 (±0.04)
P7	3	1.41 (±0.01)	1.05 (±0.02)	1.68 (±0.77)	1.06 (±0.02)	106 (±13)	86 (±38)	9 (±3)	0.11 (±0.05)
P8	2	2.32 (±0.02)	2.22 (±0.01)	2.08 (±0.05)	2.20 (±0.01)	604 (±51)	1025 (±217)	6 (±2)	0.02 (±0.00)
P9	2	1.55 (±0.02)	1.48 (±0.08)	1.57 (±0.22)	1.50 (±0.08)	142 (±28)	22 (±7)	8 (±2)	0.27 (±0.10)
P9	3	1.64 (±0.02)	1.23 (±0.06)	1.82 (±0.28)	1.31 (±0.07)	109 (±21)	22 (±11)	13 (±5)	0.36 (±0.19)
P10	3	2.22 (±0.71)	1.60 (±0.02)	1.99 (±0.08)	1.66 (±0.02)	326 (±30)	347 (±85)	7 (±2)	0.04 (±0.01)

Table 5.5: NH_3 derived properties

ID	CP	V_{LSR} (km s^{-1})	ΔV (km s^{-1})	$T_{mb}(1,1)$ (K)	$E_{T_{mb}(1,1)}$ (K)	$\tau(1,1)$	$E_{\tau(1,1)}$	$T_{mb}(2,2)$ (K)	$E_{T_{mb}(2,2)}$ (K)	T_{rot} (K)	$E_{T_{rot}}$ (K)	T_{kin} (K)	$E_{T_{kin}}$ (K)
(1)	(2)	(3)	(4)	(5)	(6)	(7)	(8)	(9)	(10)	(11)	(12)	(13)	(14)
S159	1	-58.01	1.13 (±0.17)	0.59	0.06	1.3	0.7	0.19	0.05	17.1	2.0	18.2	2.0
″	2	-55.87	2.16 (±0.25)	0.45	0.06	0.1	0.1	0.32	0.05	25.7	3.4	29.3	3.4
P1	2	-50.12	2.15 (±0.19)	0.74	0.10	0.3	0.3	0.13	0.07	13.7	2.6	14.4	2.6
P2	2	-50.95	1.50 (±0.00)	0.41	0.20	-	-	0.14	0.14	17.6	8.4	19.0	8.4
P5	2	-52.76	2.25 (±0.05)	1.58	0.09	1.1	0.1	0.50	0.19	17.0	2.7	18.2	2.7
P6	-	-	-	0.12	0.12	-	-	0.08	0.08	26.4	23.9	30.2	23.9
P8	2	-52.83	2.07 (±0.08)	2.11	0.15	1.0	0.2	0.55	0.12	15.8	1.4	16.7	1.4
P9	2	-54.18	2.82 (±0.82)	0.54	0.06	-	-	0.21	0.05	18.5	2.3	20.0	2.3
″	3	-52.03	1.40 (±0.82)	0.47	0.06	1.0	0.1	0.14	0.05	16.8	2.6	18.0	2.6
P10	3	-52.23	1.65 (±0.11)	1.35	0.14	0.8	0.3	0.20	0.10	13.0	2.1	13.5	2.1

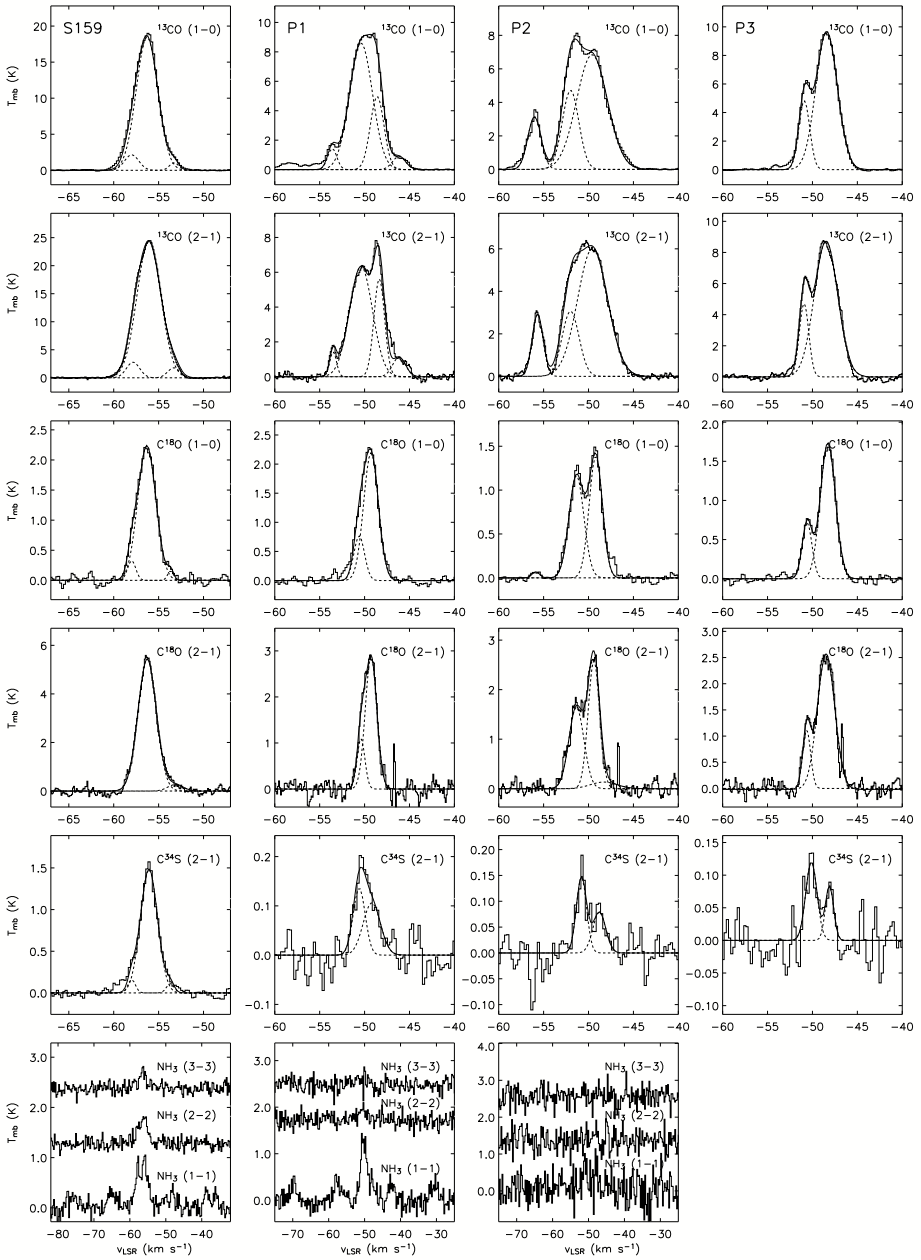

Figure 5.7: Observed spectra (solid lines) and for the IRAM data the Gaussian fits (dashed lines) for the positions listed in Table 5.1. Each column contains the spectra of the position labelled at the top in the following order: ^{13}CO 1-0, ^{13}CO 2-1, C^{18}O 1-0, C^{18}O 2-1, C^{34}S 2-1 and NH_3. Missing panels were not observed.

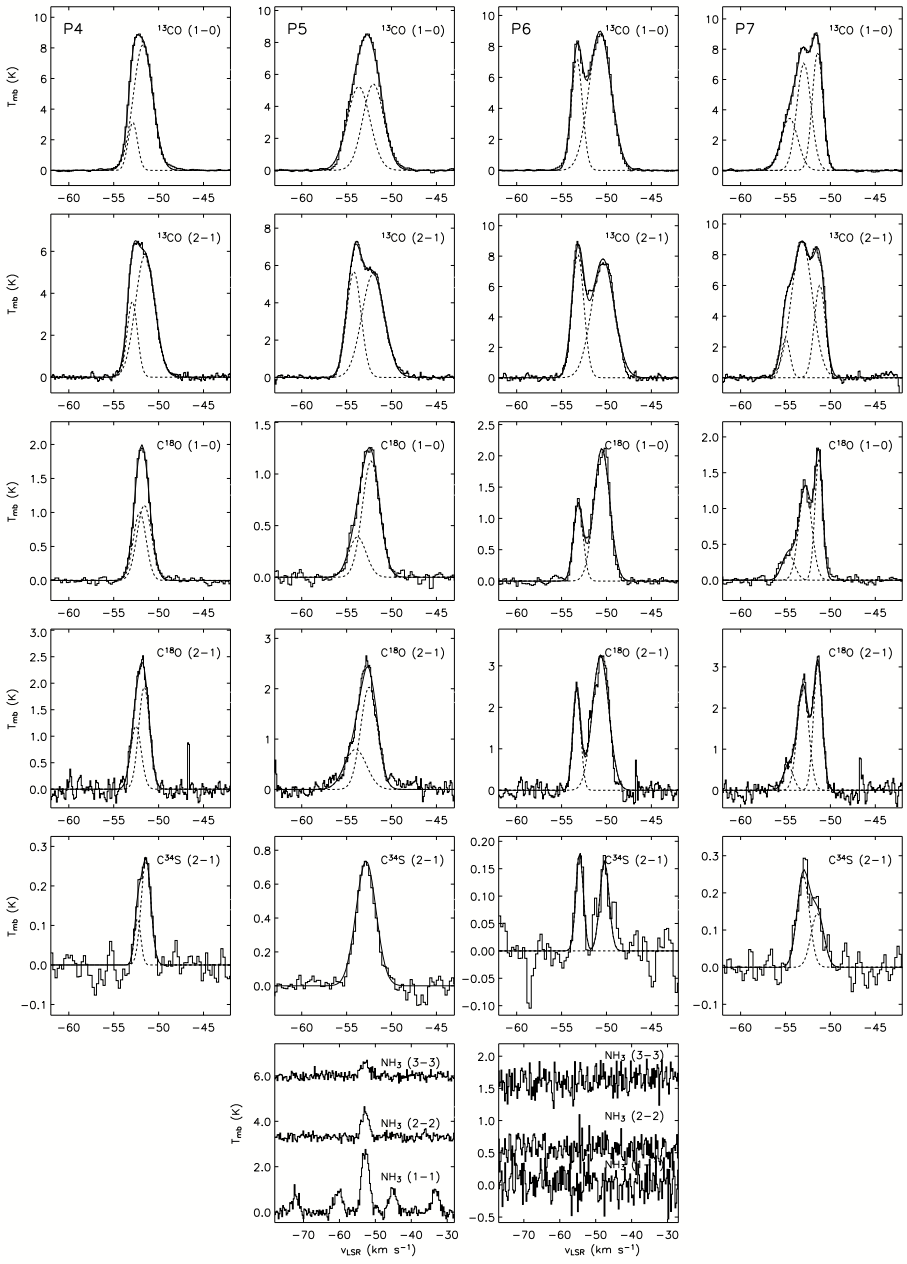

Figure 5.8: Same as Figure 5.7.

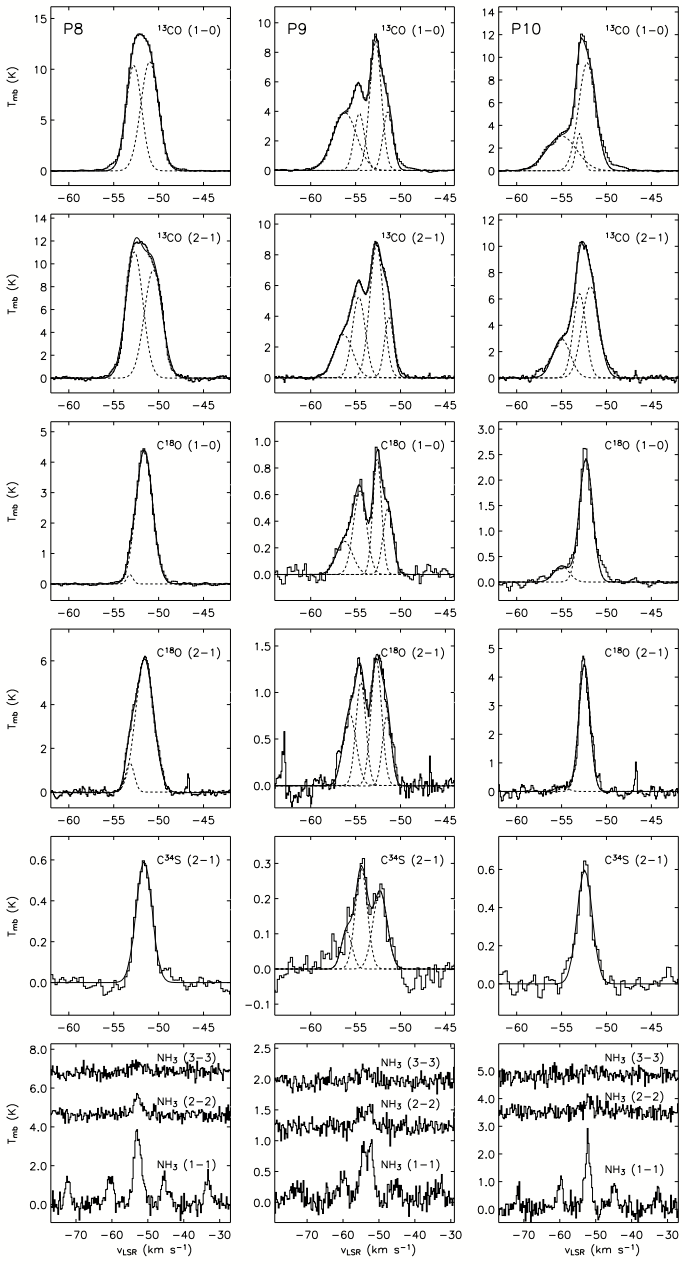

Figure 5.9: Same as Figure 5.7.

Chapter 6

Spitzer's mid-infrared view on an Outer Galaxy Infrared Dark Cloud candidate toward NGC 7538

W. W. F. Frieswijk et al. 2007*

ABSTRACT

INFRARED DARK CLOUDS represent the earliest stages of clustered star formation. The clouds are characterised by large column densities of cold and dense molecular material and are observed in silhouette against bright background infrared emission. Up to now, such dense cores were predominantly known toward the Inner Galaxy where background infrared emission levels are high. This identification may carry with it various selection effects. An investigation on the existence and whereabouts of massive dark clouds in the Outer Galaxy, based on near-infrared star color distributions, is ongoing. The suggestion is that these objects certainly exist. This is implied by the presence of more developed stages of massive star formation, e.g., W3, NGC7538. A recently identified massive molecular core complex, labelled G111.80+0.58, is studied in detail by Frieswijk et al. (2007). The cloud is located in the vicinity of the star forming region NGC7538, but is in a relatively early stage of evolution. With this Letter we present the first results of *Spitzer* observations with the Infrared Camera Array that unambiguously show object G111.80+0.58 to be an infrared dark cloud complex. This means that we have identified a true infrared dark cloud for the first time beyond the Solar circle in the Galaxy, at a Galactocentric distance of ~ 10 kpc. We conclude that objects similar to Inner Galaxy Infrared Dark Clouds are present throughout the Galaxy. However, against low infrared background emission it takes some effort to find them.

*Submitted to The Astrophysical Journal as Frieswijk, W. W. F., Spaans, M., Shipman, R. F., Teyssier, D., Carey, S. & Tielens, A. G. G. M.

6.1 Introduction

Massive stars are believed to form almost exclusively in stellar clusters (Blaauw 1964; de Wit et al. 2005), where supposedly the majority of the stars in the Galaxy form. The precursors to these stellar clusters are cold, dense and, most importantly, massive dark cores in Giant Molecular Clouds (GMCs). A major, unexpected and exciting result from the Midcourse Space Experiment (MSX) and Infrared Space Observatory (ISO) is the discovery of dark clouds seen in silhouette against the bright mid-infrared background toward the Inner Galactic Plane (Egan et al. 1998; Pérault et al. 1996). In comparison to the well-known dark clouds seen in visual extinction against the stellar distribution, these so-called Infrared Dark Clouds (IRDCs) have much higher column densities ($\gtrsim 10^{23}\,\mathrm{cm}^{-2}$), are located at large distances ($\gtrsim 1\,\mathrm{kpc}$) and hence are much more massive. Follow-up studies (e.g. Carey et al. 1998) show that they are cold ($< 20\,\mathrm{K}$), dense ($\sim 10^5\,\mathrm{cm}^{-3}$) and, indeed, among the most massive molecular cores yet found in our Galaxy (100–$10^5\,\mathrm{M}_\odot$). Many IRDCs contain compact (sub-)millimetre cores (e.g., Carey et al. 2000; Garay et al. 2004). While these massive cores were first considered to represent the pre-stellar core phase of clustered star formation, recent studies show that at least some of the IRDCs contain embedded proto-stellar objects (e.g., Redman et al. 2003; Ormel et al. 2005; Rathborne et al. 2005). Nevertheless, though some IRDCs may already have formed protostars, they are likely to represent the earliest stages of clustered star formation (e.g., Menten et al. 2005; Rathborne et al. 2006). Their ambient physical conditions can illuminate the role of IRDCs in the star forming process and can provide insight into the differences between low- and high-mass star formation, the nature of the initial mass function and the impact of environment on star (cluster) formation. Moreover, their initial core forming properties may reveal the important mechanisms involved in forming high-mass stars, e.g., competitive accretion, merging of lower-mass stars or massive disk accretion (e.g., Larson 2007, and references therein).

The identification of IRDCs is by necessity biased toward regions with high background mid-IR emission. Because of this obvious selection effect, IRDCs had been identified only in the inner parts of the Galaxy, mainly toward the inner spiral arms and the molecular ring (Simon et al. 2006b). An unbiased, more complete understanding of massive star formation and its dependence on the environment and other external properties (e.g., interstellar radiation field, metallicity, external pressure, dynamics) requires a study of similar objects in more quiescent regions, such as the Outer Galaxy.

Frieswijk et al. (2008, see Chapters 3 and 4) produced a catalogue of extended red objects in the Outer Galactic Plane derived from the $H - K_S$ colour distribution of stars in the *Two Micron All Sky Survey Point Source Catalog* (2*MASS*, Skrutskie et al. 2006). Based on the abnormally red colours and the kinematic distances of associated CO, they suggest that some of the objects in the catalogue are Outer Galaxy counterparts of Inner Galaxy IRDCs. In another paper by Frieswijk et al. (2007, see Chapter 5) they studied the physical characteristics of the candidate massive dark cloud G111.8+0.58, located in the Perseus spiral arm at a distance of $\sim 3\,\mathrm{kpc}$, by using molecular line observations. They mapped the complex in $C^{18}O$ 2-1, which revealed multiple massive and cold cores along a filamentary cloud structure. Their

main conclusion is that the cloud has global properties indeed very similar to Inner Galaxy IRDCs. The individual core properties, e.g., mass and density, are not all as high as the properties observed for sub-millimetre cores in IRDCs. However, some are, and the highest column densities ($> 10^{23}$ cm^{-2}) could be observed in mid-IR absorption if the background is bright enough.

We subsequently proposed for follow-up Spitzer observations toward this cloud to test the idea that G111.8+0.58 is a true infrared dark cloud. Observations with MSX were not able to resolve this because of its low sensitivity. In contrast, with the sensitivity of the Infrared Camera Array (IRAC) on Spitzer it should be possible to distinguish the molecular core complex from its environment. In this paper, we present the first results of the data. We have beyond doubt a detection of an infrared dark cloud in the Outer Galaxy. The paper is organised as follows: Section 6.2 gives a brief overview of the observations. Section 6.3 presents the results. In Section 6.4 we discuss the observations and give our interpretation of the data presented in this chapter compared with the results published in Chapter 5. We end the section with some future perspectives.

6.2 Observations

The data we present in this paper are part of a larger project that focusses on the star formation characteristics of Outer Galaxy massive dark clouds. The 3.5–8 μm observations were carried out using the IRAC instrument on the *Spitzer Space Telescope*. Additional IRAC data are expected, as well as 24 μm data from the Multiband Imaging Photometer (MIPS) on Spitzer, and these will be used for a full analysis of the proto-stellar content of the region. However, the emphasis of this paper is to present the first identification of an Outer Galaxy IRDC. For that purpose, the present data set is adequate.

In order to cover the full extent of the cloud complex that was observed in $C^{18}O$ 2-1 (Chapter 5), the infrared maps consist of a cycling 7-point dither pattern with medium scale step-size. The data were processed and transformed into mosaic images using the standard data processing pipeline version S16.1.0, as provided by the Spitzer Science Center. Additional calibration of the data is certainly needed when a detailed analysis on band-merged images is performed. However, for this paper the standard pipeline produces data of sufficient quality to examine the contrast at 8 μm between the dark cloud and its surroundings.

6.3 Results

Figure 6.1 shows the 8 μm emission observed with IRAC toward the candidate massive dark cloud G111.8+0.58. The image reveals a dark, filamentary structure against the bright and diffuse mid-IR emission. The diffuse emission resembles the feathery cirrus emission first observed with the *Infrared Astronomical Satellite* (IRAS, e.g., Low et al. 1984). The cirrus observed with IRAS is assumed to be predominantly local, but here at least part of the emission appears to be located behind the dark clouds, at a distance beyond ~ 3 kpc.

The contours show the integrated $C^{18}O$ 2-1 emission from Chapter 5. The dark structure matches the contours of the $C^{18}O$ strikingly well. This implies that we truly

observe a dark cloud, unlike the dark 'hole' appearing at the right side of the image, where we do not see a match with $C^{18}O$. The locations in the figure, indicated by P1 to P10, represent the target positions introduced in Chapter 5. We briefly discuss their properties in Section 6.4.1.

The 8 μm image reveals several clusters of point-like objects along the cloud filaments, most noticeably near P5 and P8. The lower left two panels of Figure 6.1 display false-colour composite close-ups of these positions in the four IRAC bands, i.e., 3.6 μm (blue), 4.5 μm (green), 5.8 μm (yellow) and 8 μm (red). In addition, the lower right panel displays a false-colour close-up of the bright source IRAS23136+6111. The intensities there are scaled in such a way that the dark lane, corresponding to the filament seen in $C^{18}O$, stands out clearly against the bright emission of the IRAS source.

We quantify the correlation between the dark features observed in the Spitzer data and the $C^{18}O$ emission by determining the mean 8 μm emission in increasing $C^{18}O$ emission bins. In order to remove the contribution of bright point sources, we first smooth the 8 μm image with a median filter of 11 pixels wide (1 pixel = 1.2″). We choose a $C^{18}O$ bin-size of 1 K km s^{-1} and use only the region that is actually covered by the $C^{18}O$ observations. The results are given schematically in Figure 6.2. The first bin in the diagram represents an estimate of the background, determined from several positions in the image away from the dark cloud, after filtering as described above. An alternative background estimate is provided by the second bin in the diagram, which represents the 8 μm emission at any position where the $C^{18}O$ emission is less than 1 K km s^{-1}. The last bin of the diagram represents the lowest 8 micron emission toward locations where there is $C^{18}O$ in excess of 1 K km s^{-1}. The dashed boxes for each bin represent the scatter of the 8 μm emission. Note that the scatter is significant in the lower $C^{18}O$ bins (1–4 K km s^{-1}) because the extended, bright 8 μm emission falls within these contours (see Figure 6.1).

If we adopt a background emission of 21 MJy sr^{-1}, and assume that the low emission, i.e., 13 MJy sr^{-1}, is purely due to absorption of the dark cloud we can estimate the extinction. Using standard conversions given in the IRAC data handbook, the decrease in 8 μm emission of 8 MJy sr^{-1} corresponds to 0.5 magnitudes of extinction. This value represents only a lower limit. Both the cloud and the background are contaminated by emission from foreground material and zodiacal light. The contribution of the zodiacal light is 4.2 MJy sr^{-1}, adopted from the Spitzer observation planning tool (SPOT). The foreground is difficult to determine. If we conservatively (remember the cloud is at 3 kpc) assume a foreground of 4 MJy sr^{-1}, then the magnitude of the extinction at 8 μm is unity. For convenience, the mid-IR extinction can be expressed in terms of visual extinction using $A_V \sim 25 \times A_{8\mu m}$, where a standard conversion is adopted from Rieke & Lebofsky (1985). The arrow in Figure 6.2 corresponds to an A_V of 10 magnitudes if a background of 21 MJy sr^{-1} is assumed.

6.4 Conclusions

The molecular cloud complex G111.8+0.58 can be unambiguously identified as an infrared dark cloud. How do the mid-IR properties compare to Inner Galaxy IRDCs?

A typical 8 μm extinction observed toward Inner Galaxy IRDCs, determined from

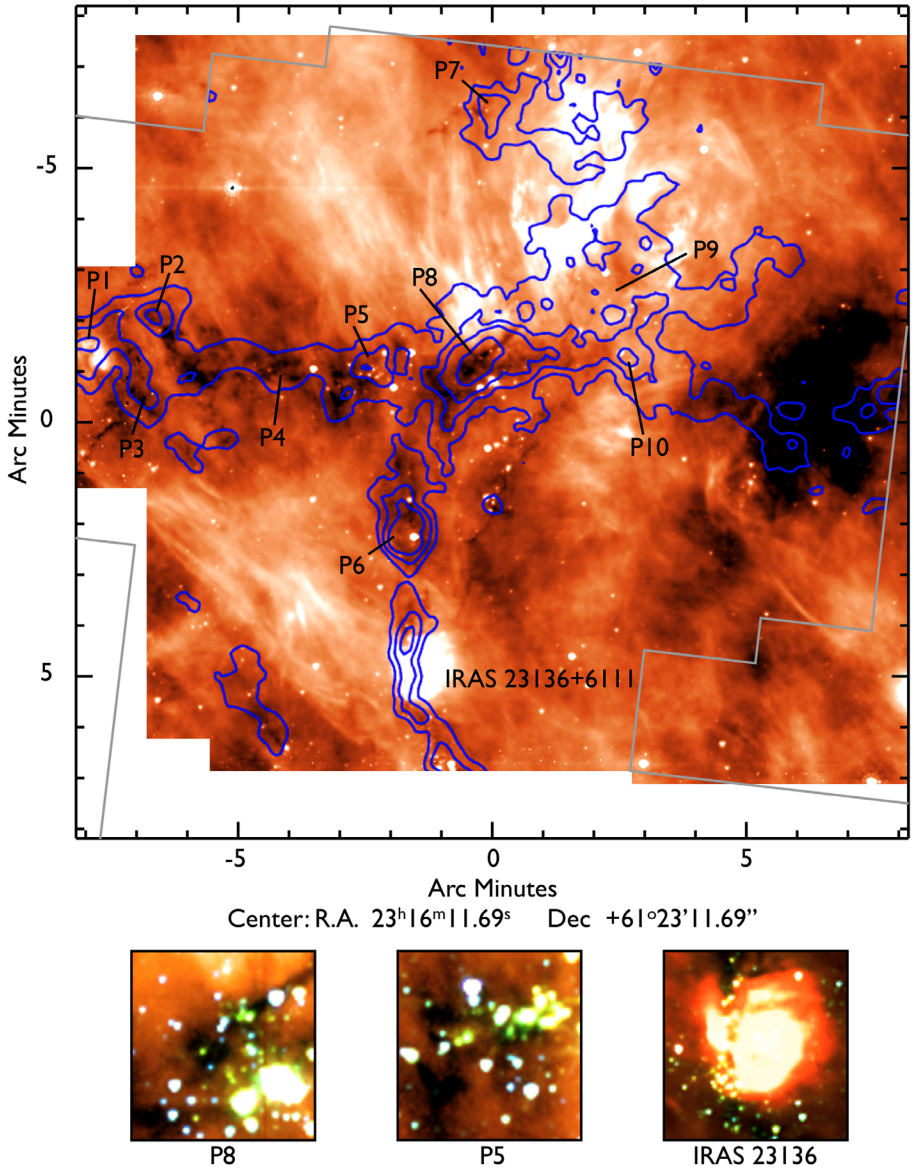

Figure 6.1: This figure shows the IRAC 8 μm emission toward the dark cloud G111.8+0.58. The contours depict the integrated $C^{18}O$ 2-1 emission between -56 and -46 km s^{-1} and correspond, from outside-in, to 2, 3, 4 and 6 K km s^{-1}. The grey line indicates the area covered by the $C^{18}O$ observations. The P-numbers represent the target positions from Chapter 5. The bottom images show a false-colour close-up of positions P8, P5 and IRAS23136+6111. The displayed emission is from the four IRAC channels, i.e., 3.6 μm (blue), 4.5 μm (green), 5.8 μm (yellow) and 8 μm (red)

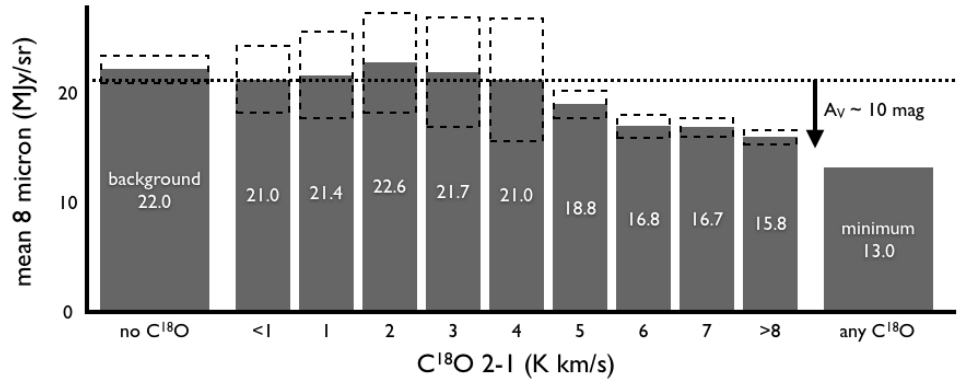

Figure 6.2: Schematic overview of the correlation between the 8 μm diffuse emission, and the $C^{18}O$ 2-1 emission. The dotted line represents a background of 21 MJy sr^{-1}. Even though the scatter, indicated by the dashed boxes, is significant for low $C^{18}O$ emission, the trend is clear. The brighter $C^{18}O$ emission, i.e., higher column densities, corresponds to the lowest mid-IR emission.

the ratio between the on- and off-source emission after foreground and zodiacal light correction, is 1–2 mag (Egan et al. 1998; Carey et al. 2000). Our estimate of the extinction based on the 8 μm emission is, at least toward the darkest regions of the cloud, in agreement with these values. Even more, the extinction measurement from the emission gives only a strict lower limit to the column of material. The dark cloud does not only absorb background emission, but re-radiates some low-level emission as well. For a cold dark cloud ($<$25 K) this will be negligible. However, once embedded objects start heating parts of the cloud this may become important. The contrast between the cloud and the background, and thus the measured extinction, goes down as the cloud emits, but of course the column of material does not.

The molecular column densities of the target positions, determined from $C^{18}O$, are all of the order of 10^{22} cm^{-2} with a peak value of $\approx 7 \times 10^{22}$ cm^{-2} for P8. The latter corresponds to about 2.8 mag extinction at 8 μm (70 mag visual). These estimates demonstrate that parts of this cloud have a mid-IR extinction comparable to values found for Inner Galaxy IRDCs (e.g., Carey et al. 1998; Hennebelle et al. 2001).

Recall in this that IRDCs are identified in MSX by a selection based on high contrast (Simon et al. 2006b). In the Outer Galaxy, a high contrast is not guaranteed because of the low-level background emission. For example, compare the background of the IRDCs toward the edge of W51, i.e., $\sim$60 MJy sr^{-1} (IRAC/MIPS cycle 1 observations, K. Kraemer et al., priv. comm.) with the background that we observe ($\sim$20 MJy sr^{-1}). Note that one bright 8 μm emission feature clearly is in the background of G111.80+0.58, since a dark lane is visible in front of IRAS23136+6111 (see Figure 6.1, lower right blow-up).

The four-colour images show a clustering of objects near the dark filaments. This

suggests that some cores in the complex have started to form stars. This excess in star counts was also mentioned in Chapter 5 for positions P5 and P8, based on the 2MASS data. Note that Inner Galaxy IRDCs are often associated with active star formation as well (e.g., Redman et al. 2003; Ormel et al. 2005; Rathborne et al. 2005). Star forming activity may further reveal itself by the presence of 'green fuzzy emission', i.e., weak extended 4.5 μm features. This emission is usually attributed to shocked gas, e.g., the pure rotational S(11) H_2 line at 4.18 μm, arising from outflow-activity a (e.g., Noriega-Crespo et al. 2004; Marston et al. 2004). Shocked gas features are, besides for nearby star formation, also frequently observed toward Inner Galaxy IRDCs (e.g., Rathborne et al. 2005; Beuther & Steinacker 2007). A first impression of the emission observed with IRAC channel 2 suggests that these features are present along some lines of sight. However, further investigation is required to confirm this.

6.4.1 Notes on individual cores

The following notes on the target positions displayed in Figure 6.1 supplement the information given in Chapter 5.

P1, P2, P3 and P7: Except for P1, which is associated with enhanced emission, all cores correspond to a decrease in 8 μm emission, i.e., extinction. The peak of the extinction appears somewhat offset from the $C^{18}O$ peak for all cores. This may be explained by $C^{18}O$ freeze-out in the densest regions.

P4, P9 and P10: P4 is part of the $C^{18}O$ filament extending to the left. Several extinction peaks at 8 μm are associated with this part. P9 and P10 are associated with enhanced 8 μm emission and show no specific features.

P6: There is some extinction associated, which may be weakened due to the presence of the bright red object near the $C^{18}O$ peak.

P5 and P8: Both positions are associated with high extinction features. Moreover, the four-colour images reveal signs of active star formation in the form of clustering of objects and 4.5 μm 'green fuzzes'.

IRAS23136+6111: This was not a target position in Chapter 5, but the $C^{18}O$ revealed a narrow filament. The four-colour image shows that the filament is associated with a dark lane and thus must be in the foreground of the bright IRAS object. A clustering of point sources can also be discerned along the filament. Further investigation is required to see if the dark lane and the IRAS source are associated, which may indicate a triggered star forming event.

6.4.2 Future prospects

Supplemental IRAC and MIPS 24 micron data from Spitzer are expected. Combining the IRAC bands with, as far as possible, the 2MASS data enable a discrimination between stars and young stellar objects for many of the clustered point sources in the dark cloud vicinity. Adding 24 μm data will allow a proper SED modelling of the

dust emission. The characteristic features of envelopes, disks and photospheres in the SED will enable a determination of the evolutionary state, i.e., Class 0, I, II or III, of the apparent discrete sources (e.g., Robitaille et al. 2007). Star forming activity can be further characterised through an analysis of the spatial distribution and strength of polycyclic aromatic hydrocarbon (PAH) emission (e.g., 3.3, 6.2 and 7.7 μm covered by IRAC channel 1, 3 and 4, respectively) and shock activity, exemplified by the the 4.5 μm features in the blow-up images in Figure 6.1 (e.g., bow shocks; Neufeld et al. 2006; Velusamy et al. 2007). Follow-up high-resolution observations (near-IR to millimetre), both continuum and spectroscopic, are considered essential to improve the spatial information at the distance this cloud is located.

Chapter 7

Summary and future prospects

7.1 Summary

IN THIS THESIS we have described the search for, and discovery of, massive dark clouds in the outer Galactic Plane. We have presented a statistical analysis of the near-IR colours of stars present in the Two Micron All Sky Survey. The result is a reliable list of over 1000 red extended objects. Follow-up investigation provided additional information on the properties of target objects, e.g., the association with known dark clouds, distance estimates and signatures of star forming activity. Furthermore, we have presented a detailed analysis of object G111.80+0.58. This resulted in the first identification of an Infrared Dark Cloud in the outer parts of the Galactic Plane.

Here, I will summarise the main conclusions of this thesis.

- *Chapter 3*
  The Mann-Whitney U-test provides the necessary statistical tool to determine deviations from near-IR colours of stars on a relatively high spatial resolution (arc-minute scale). The benefit of the U-test is, that it can compare very small colour distributions (≥ 5 samples) against large distributions ($\sim 10\,000$ samples). Moreover, the method determines deviations uniformly in every direction in the outer Galactic Plane (covering 1260 square degrees) and is independent of foreground, unreddened stars.
  At a confidence level in excess of 99% we have identified 1320 and 1589 extended red objects at $60''$ and $90''$ resolution, respectively. About one-third of the objects are associated with optically identified dark clouds. About half of the objects have associated infrared point sources, either MSX (8 μm) or IRAS (12, 25, 60 and 100 μm). There are 369 objects at $60''$ resolution and 434 at $90''$resolution that have none of the aforementioned associations.

- *Chapter 4*
  The correlation analysis with CO data reveals that most of the red extended objects are spatially associated with molecular gas emission at discrete velocities ($>90\%$ detection rate of CO). The velocity width of the CO features is of the order of $2-4\,\mathrm{km\,s^{-1}}$. This suggests that the regions are reddened due to foreground molecular clouds. A few hundred objects have associated CO emission at nearby velocities ($\lesssim 3\,\mathrm{kpc}$). More than 80% of these have an optically identified dark cloud associated as well. About 100 objects have CO emission associated at distant velocities ($\gtrsim 3\,\mathrm{kpc}$). We find 65 objects that have only a distant CO counterpart and 37 of these have an optical dark cloud associated. We find a correlation between the presence of mid-IR point sources and an increase in the CO peak intensity, which supports the idea that a mid-IR association indicates the presence of star forming activity.

- *Chapter 5*
  G111.80+0.58 is the first object that is selected as an Outer Galaxy massive dark cloud candidate purely based on the analysis presented in Chapters 3 and 4. The molecular line observations that we present show that the global physical properties, e.g., mass ($>3000\,\mathrm{M_\odot}$), temperature ($<25\,\mathrm{K}$), column density ($\gtrsim 10^{23}\,\mathrm{cm^{-2}}$) and line-width (super-thermal) are very similar to values found for Inner Galaxy IRDCs. The near-IR colours of a number of sources in 2MASS, located toward some of the dense cores, resemble colours of Young Stellar Objects. Given also the presence of warm gas, indicated by the NH_3 lines, we interpret this as evidence for star forming activity.

- *Chapter 6*
  The sensitive mid-IR observations, conducted with the Spitzer Space Telescope, reveal significant absorption at $8\,\mu$m and therefore unambiguously identify G111.80+0.58 as an Infrared Dark Cloud. Moreover, an initial inspection of the Spitzer data shows the presence of star forming activity. We see a clustering of embedded red objects and signatures of shocks toward some parts of the cloud. This is also frequently observed toward Inner Galaxy IRDCs. The Spitzer data confirm the results, and support the suggestions presented in the previous chapters.

The results of Chapters 5 and 6 demonstrate the power of the identification method and exemplify the value of the catalogue of extended red objects. The question raised at the end of Chapter 2, whether we can identify Infrared Dark Clouds in the Outer Galaxy, is resolved. Yes, we can!

7.2 Future prospects

7.2.1 The catalogue of near-IR extended red objects

The catalogue of red objects consists of sources that can be very different in nature. However, they share one main characteristic: the colour distribution of stars toward the objects is different compared to the surroundings. In this thesis we have shown that, besides many well-known objects that are present, previously unidentified massive dark clouds can be extracted from the catalogue. These dark clouds represent the earliest observed stages of clustered star formation in the Outer Galactic Plane. We have made a first step into the investigation of initial conditions in cluster forming clouds toward different environments in the Galaxy. Obviously, a larger sample of objects is desired. Unfortunately, the identification process is time consuming. Additional observations are essential to probe the physical conditions of objects. At the moment, only the best candidates are considered for follow-up investigation.

In the near future the catalogue can provide valuable information on the near-IR properties of objects that will be identified in upcoming surveys, mainly in the far-IR and sub-millimetre range. An important science driver for these surveys, related to this thesis, is to get a complete picture of massive star forming regions throughout the Galaxy, i.e., to investigate their Galactic distribution and individual star forming properties. Also, forthcoming observatories will provide exciting new opportunities to study the details of (clustered) star formation throughout the Galaxy (and beyond). Prospects for the future include the following:

SCUBA2
Two interesting examples for a future comparison with our catalogue are surveys scheduled with the Submillimetre Common-User Bolometer Array instrument (SCUBA2) on the James Clerk Maxwell Telescope[†] (JCMT). These are the JCMT Galactic Plane Survey (GPS, at 450 μm and 850 μm) and the SCUBA2 'All Sky Survey' (SASSY, 850 μm). The high sensitivity that is realised with SCUBA2 allows the detection of embedded phases of high-mass stars to the edge of the Galaxy. Moreover, these sub-millimetre surveys will probe the large column densities of cold dust present in IRDCs. Therefore, they are very efficient in mapping the IRDC population in both the Inner and Outer Galaxy. However, a distance to the sub-millimetre emission cannot be determined without supplemental data. Also, with at most two data-points on the spectral energy distribution it is impossible to distinguish between the earliest, cold stages and the more developed stages of star formation. For many objects that will be identified through sub-millimetre observations, our catalogue may provide the additional information that is required.

Herschel
The Herschel Space Observatory[‡] will enable astronomers to study the life

[†]URL: http://www.jach.hawaii.edu/JCMT/
[‡]URL: http://herschel.esac.esa.int/

cycle of stars in detail throughout the Galaxy. The instruments that Herschel will have onboard are the Photodetector Array Camera and Spectrometer (PACS), the Spectral and Photometric Imaging Receiver (SPIRE) and the Heterodyne Instrument for the Far-Infrared (HIFI).

The fast scanning rate and the large wavelength coverage of PACS and SPIRE ($60-600\,\mu$m) will enable photometric imaging with a proper sampling of the spectral energy distribution of much of the cold dust in the Galaxy.

HIFI will have the ability to observe thousands of molecular, atomic and ionic lines at an unprecedented spectral resolution ($R \sim 10^7$) in the far-IR and sub-millimetre regime ($480-1910\,$GHz), giving a unique opportunity to investigate in great detail the gas kinematics and physical conditions in star forming regions.

ALMA
In a few years time, the Atacama Large Millimeter/sub-millimeter Array[†] (ALMA) will become available. The spatial resolution that will be obtained with this interferometer is unprecedented in this wavelength regime. For the first time, it will be possible to zoom in on distant dark clouds and observe directly the cold embedded stages of massive star formation; something that is now only possible in nearby star forming regions.

7.2.2 G111.80+0.58

The physical conditions that we determine for G111.80+0.58 in Chapter 5 are very similar to the conditions observed in Inner Galaxy IRDCs. At this point, however, we cannot be conclusive on whether the star forming properties in this environment are also similar. Future investigation on both the proto-stellar content and the gas properties on small angular scales is essential to put the cloud in perspective with Inner Galaxy IRDCs.

The Spitzer observations presented in Chapter 6 reveal the presence of active star formation. Supplemental Spitzer data are expected (both IRAC and MIPS 24μm) and only a full analysis of the data will give insight in, e.g., the evolutionary state of many of the discrete sources along the dark filaments and shock activity.

Some of the dense cores along the filament likely fragmented into smaller objects due to gravitational instability (Chapter 5). High spatial resolution observations from the ground, both continuum and spectroscopic, will be essential to acquire information on the gas distribution and kinematics on small angular scales. E.g., with the Extended Sub-Millimetre Array, Plateau du Bure Interferometer or the Australian Telescope Compact Array.

To conclude, dark cloud G111.80+0.58 may just be an average dense molecular cloud, i.e., one of many that are present throughout the Galaxy. Nonetheless, for now it constitutes the prototypical IRDC in the Outer Galaxy.

[†]URL: http://www.alma.cl/

Bibliography

Alves, J. ., Lada, C. J., Lada, E. A., Kenyon, S. J., & Phelps, R. 1998, ApJ, 506, 292

Andre, P. & Montmerle, T. 1994, ApJ, 420, 837

Bachiller, R., Guilloteau, S., & Kahane, C. 1987, A&A, 173, 324

Ballesteros-Paredes, J., Klessen, R. S., Mac Low, M. ., & Vazquez-Semadeni, E. 2006, ArXiv Astrophysics e-prints

Barnard, E. E. 1919, ApJ, 49, 1

Bergin, E. A. & Langer, W. D. 1997, ApJ, 486, 316

Bergin, E. A., Langer, W. D., & Goldsmith, P. F. 1995, ApJ, 441, 222

Bergin, E. A. & Tafalla, M. 2007, ARA&A, 45, 339

Bessell, M. S. & Brett, J. M. 1988, PASP, 100, 1134

Beuther, H. & Steinacker, J. 2007, ApJ, 656, L85

Blaauw, A. 1964, ARA&A, 2, 213

Blitz, L., Fich, M., & Stark, A. A. 1982, ApJ, 49, 183

Bohlin, R. C., Savage, B. D., & Drake, J. F. 1978, ApJ, 224, 132

Bok, B. J. 1948, in Centennial Symposia, 53–+

Bonnell, I. A., Bate, M. R., Clarke, C. J., & Pringle, J. E. 1997, MNRAS, 285, 201

Bonnell, I. A., Bate, M. R., & Zinnecker, H. 1998, MNRAS, 298, 93

Bonnell, I. A., Clarke, C. J., Bate, M. R., & Pringle, J. E. 2001, MNRAS, 324, 573

Bonnell, I. A. & Davies, M. B. 1998, MNRAS, 295, 691

Bourke, T. L., Garay, G., Lehtinen, K. K., et al. 1997, ApJ, 476, 781

Brand, J. & Blitz, L. 1993, A&A, 275, 67

Brand, J. & Wouterloot, J. G. A. 1995, A&A, 303, 851

Brunt, C. M., Kerton, C. R., & Pomerleau, C. 2003, ApJ, 144, 47

Cambrésy, L., Beichman, C. A., Jarrett, T. H., & Cutri, R. M. 2002, AJ, 123, 2559

Carey, S. J., Clark, F. O., Egan, M. P., et al. 1998, ApJ, 508, 721

Carey, S. J., Feldman, P. A., Redman, R. O., et al. 2000, ApJ, 543, L157

Caselli, P. & Myers, P. C. 1995, ApJ, 446, 665

Chini, R. & Wink, J. E. 1984, A&A, 139, L5

Clark, F. O., Laureijs, R. J., & Prusti, T. 1991, ApJ, 371, 602

de Wit, W. J., Testi, L., Palla, F., & Zinnecker, H. 2005, A&A, 437, 247

Dickman, R. L. 1978, ApJ, 37, 407

Dobashi, K., Uehara, H., Kandori, R., et al. 2005, PASJ, 57, 1

Draine, B. T. & Li, A. 2001, ApJ, 551, 807

Draine, B. T. & Li, A. 2007, ApJ, 657, 810

Egan, M. P., Shipman, R. F., Price, S. D., et al. 1998, ApJ, 494, L199

Elmegreen, B. G. 1999, ApJ, 515, 323

Evans, N. J. 1999, ARA&A, 37, 311

Forveille, T., Guilloteau, S., & Lucas, R. 1989, Grenoble: IRAM

Frerking, M. A., Langer, W. D., & Wilson, R. W. 1982, ApJ, 262, 590

Frieswijk, W. W. F. & Shipman, R. F. 2007, To be submitted to A&A

Frieswijk, W. W. F., Spaans, M., Shipman, R. F., Teyssier, D., & Hily-Blant, P. 2007, A&A, 475, 263

Froebrich, D., Ray, T. P., Murphy, G. C., & Scholz, A. 2005, A&A, 432, L67

Garay, G., Faúndez, S., Mardones, D., et al. 2004, ApJ, 610, 313

Goodman, A. A., Barranco, J. A., Wilner, D. J., & Heyer, M. H. 1998, ApJ, 504, 223

Hachisuka, K., Brunthaler, A., Menten, K. M., et al. 2006, ApJ, 645, 337

Hennebelle, P., Pérault, M., Teyssier, D., & Ganesh, S. 2001, A&A, 365, 598

Herschel, W. 1785, Philosophical Transactions Series I, 75, 213

Heyer, M. H., Brunt, C., Snell, R. L., et al. 1998, ApJ, 115, 241

Huchra, J. P. & Geller, M. J. 1982, ApJ, 257, 423

Indebetouw, R., Mathis, J. S., Babler, B. L., et al. 2005, ApJ, 619, 931

Jeans, J. H. 1928, Astronomy and cosmogony (Cambridge [Eng.] The University press, 1928.)

Johnstone, D., Fiege, J. D., Redman, R. O., Feldman, P. A., & Carey, S. J. 2003, ApJ, 588, L37

Kameya, O., Morita, K.-I., Kawabe, R., & Ishiguro, M. 1990, ApJ, 355, 562

Kandori, R., Dobashi, K., Uehara, H., Sato, F., & Yanagisawa, K. 2003, AJ, 126, 1888

Kant, I. 1755, Allgemeine Naturgeschichte und Theorie des Himmels (Zeitz, Bei W. Webel, 1798. Neue aufl.)

Kerton, C. R. & Brunt, C. M. 2003, A&A, 399, 1083

Klessen, R. S., Ballesteros-Paredes, J., Li, Y., & Mac Low, M.-M. 2004, in ASP Conf. Ser. 322: The Formation and Evolution of Massive Young Star Clusters, ed. H. J. G. L. M. Lamers, L. J. Smith, & A. Nota, 299–+

Kroupa, P. 2001, MNRAS, 322, 231

Lada, C. J. 1987, in IAU Symposium, Vol. 115, Star Forming Regions, ed. M. Peimbert & J. Jugaku, 1–17

Lada, C. J. 1999, in NATO ASIC Proc. 540: The Origin of Stars and Planetary Systems, ed. C. J. Lada & N. D. Kylafis, 143–+

Lada, C. J., Alves, J. ., & Lada, E. A. 1999, ApJ, 512, 250

Lada, C. J., Lada, E. A., Clemens, D. P., & Bally, J. 1994, ApJ, 429, 694

Lada, C. J. & Wilking, B. A. 1984, ApJ, 287, 610

Larson, R. B. 1981, MNRASAJ, 194, 809
Larson, R. B. 1985, MNRAS, 214, 379
Larson, R. B. 1998, MNRAS, 301, 569
Larson, R. B. 2007, ArXiv Astrophysics e-prints
Lebrón, M. E., Rodríguez, L. F., & Lizano, S. 2001, ApJ, 560, 806
Lombardi, M., Alves, J., & Lada, C. J. 2006, A&A, 454, 781
Low, F. J., Young, E., Beintema, D. A., et al. 1984, ApJ, 278, L19
Lynds, B. T. 1962, ApJ, 7, 1
Mac Low, M.-M. & Klessen, R. S. 2004, Reviews of Modern Physics, 76, 125
MacLaren, I., Richardson, K. M., & Wolfendale, A. W. 1988, ApJ, 333, 821
Marston, A. P., Reach, W. T., Noriega-Crespo, A., et al. 2004, ApJ, 154, 333
Mathis, J. S. 1990, ARA&A, 28, 37
McCrady, N., Graham, J. R., & Vacca, W. D. 2005, in Astrophysics and Space Science Library, Vol. 329, Starbursts: From 30 Doradus to Lyman Break Galaxies, ed. R. de Grijs & R. M. González Delgado, 75–+
McKee, C. F. & Ostriker, E. C. 2007, ARA&A, 45, 565
McKee, C. F. & Tan, J. C. 2003, ApJ, 585, 850
Menten, K. M., Pillai, T., & Wyrowski, F. 2005, in IAU Symposium, ed. R. Cesaroni, M. Felli, E. Churchwell, & M. Walmsley, 23–34
Miller, G. E. & Scalo, J. M. 1979, ApJ, 41, 513
Myers, P. C. & Fuller, G. A. 1993, ApJ, 402, 635
Neufeld, D. A., Melnick, G. J., Sonnentrucker, P., et al. 2006, ApJ, 649, 816
Noriega-Crespo, A., Morris, P., Marleau, F. R., et al. 2004, ApJ, 154, 352
Ormel, C. W., Shipman, R. F., Ossenkopf, V., & Helmich, F. P. 2005, A&A, 439, 613
Ossenkopf, V. & Henning, T. 1994, A&A, 291, 943
Ott, M., Witzel, A., Quirrenbach, A., et al. 1994, A&A, 284, 331
Pérault, M., Omont, A., Simon, G., et al. 1996, A&A, 315, L165
Poelman, D. R. & Spaans, M. 2005, A&A, 440, 559
Poelman, D. R. & Spaans, M. 2006, A&A, 453, 615
Price, S. D. 1995, Space Science Reviews, 74, 81
Rathborne, J. M., Jackson, J. M., Chambers, E. T., et al. 2005, ApJ, 630, L181
Rathborne, J. M., Jackson, J. M., & Simon, R. 2006, ApJ, 641, 389
Rathborne, J. M., Simon, R., & Jackson, J. M. 2007, ApJ, 662, 1082
Redman, R. O., Feldman, P. A., Wyrowski, F., et al. 2003, ApJ, 586, 1127
Reipurth, B., Jewitt, D., & Keil, K., eds. 2007, Protostars and Planets V
Rieke, G. H. & Lebofsky, M. J. 1985, ApJ, 288, 618
Robitaille, T. P., Whitney, B. A., Indebetouw, R., & Wood, K. 2007, ApJ, 169, 328
Robitaille, T. P., Whitney, B. A., Indebetouw, R., Wood, K., & Denzmore, P. 2006, ApJ, 167, 256
Rudolph, A. L., Fich, M., Bell, G. R., et al. 2006, ApJ, 162, 346

Rybicki, G. B. & Lightman, A. P. 1986, Radiative Processes in Astrophysics (Radiative Processes in Astrophysics, by George B. Rybicki, Alan P. Lightman, pp. 400. ISBN 0-471-82759-2. Wiley-VCH , June 1986.)

Salpeter, E. E. 1955, ApJ, 121, 161

Sandell, G. & Sievers, A. 2004, ApJ, 600, 269

Scalo, J. 1998, in Astronomical Society of the Pacific Conference Series, Vol. 142, The Stellar Initial Mass Function (38th Herstmonceux Conference), ed. G. Gilmore & D. Howell, 201–+

Schuster, K.-F., Boucher, C., Brunswig, W., et al. 2004, A&A, 423, 1171

Shipman, R. F., Frieswijk, W., & Helmich, F. P. 2003, in ASP Conf. Ser. 287: Galactic Star Formation Across the Stellar Mass Spectrum, ed. J. M. De Buizer & N. S. van der Bliek, 252–256

Shu, F. H., Adams, F. C., & Lizano, S. 1987, ARA&A, 25, 23

Simon, R., Jackson, J. M., Rathborne, J. M., & Chambers, E. T. 2006a, ApJ, 639, 227

Simon, R., Rathborne, J. M., Shah, R. Y., Jackson, J. M., & Chambers, E. T. 2006b, ApJ, 653, 1325

Skrutskie, M. F., Cutri, R. M., Stiening, R., et al. 2006, AJ, 131, 1163

Spitzer, L. 1998, Physical Processes in the Interstellar Medium (Physical Processes in the Interstellar Medium, by Lyman Spitzer, pp. 335. ISBN 0-471-29335-0. Wiley-VCH , May 1998.)

Stahler, S. W. & Palla, F. 2005, The Formation of Stars (The Formation of Stars, by Steven W. Stahler, Francesco Palla, pp. 865. ISBN 3-527-40559-3. Wiley-VCH , January 2005.)

Strafella, F., Campeggio, L., Aiello, S., Cecchi-Pestellini, C., & Pezzuto, S. 2001, ApJ, 558, 717

Swedenborg, E. 1734, Opera Philosophica et Mineralia (Principia), Vol. 1

Tafalla, M., Myers, P. C., Caselli, P., & Walmsley, C. M. 2004, A&A, 416, 191

Taylor, A. R., Gibson, S. J., Peracaula, M., et al. 2003, AJ, 125, 3145

Teyssier, D., Hennebelle, P., & Pérault, M. 2002, A&A, 382, 624

Tielens, A. G. G. M. 2005, The Physics and Chemistry of the Interstellar Medium (The Physics and Chemistry of the Interstellar Medium, by A. G. G. M. Tielens, pp. . ISBN 0521826349. Cambridge, UK: Cambridge University Press, 2005.)

Tielens, A. G. G. M., Hony, S., van Kerckhoven, C., & Peeters, E. 1999, in ESA Special Publication, Vol. 427, The Universe as Seen by ISO, ed. P. Cox & M. Kessler, 579–+

van der Tak, F. F. S. & van Dishoeck, E. F. 2000, A&A, 358, L79

van der Tak, F. F. S., van Dishoeck, E. F., Evans, II, N. J., & Blake, G. A. 2000, ApJ, 537, 283

van der Wiel, M. H. D. & Shipman, R. F. 2008, in preperation

van Dishoeck, E. F. & Blake, G. A. 1998, ARA&A, 36, 317

Velusamy, T., Langer, W. D., & Marsh, K. A. 2007, ApJ, 668, L159

Wainscoat, R. J., Cohen, M., Volk, K., Walker, H. J., & Schwartz, D. E. 1992, ApJ, 83, 111

Wall, J. V. & Jenkins, C. R. 2003, Practical Statistics for Astronomers (Princeton Series in Astrophysics)

Wang, Y., Zhang, Q., Pillai, T., Wyrowski, F., & Wu, Y. 2008, ApJ, 672, L33

Ward-Thompson, D., André, P., Crutcher, R., et al. 2007, in Protostars and Planets V, ed. B. Reipurth, D. Jewitt, & K. Keil, 33–46

Weingartner, J. C. & Draine, B. T. 2001, ApJ, 548, 296

Werner, M. W., Becklin, E. E., Gatley, I., et al. 1979, MNRAS, 188, 463

Williams, S. J., Fuller, G. A., & Sridharan, T. K. 2004, VizieR Online Data Catalog, 341, 70115

Wolf, M. 1923, Astronomische Nachrichten, 219, 109

Wouterloot, J. G. A. & Brand, J. 1989, A&A, 80, 149

Nederlandse Samenvatting

De vroege stadia van de vorming van sterclusters - zware donkere wolken in de Melkweg -

Dit proefschrift beschrijft de zoektocht naar zeer jonge stadia van sterclustervorming en de ontdekking van zware donkere wolken in de buitenste delen van de Melkweg. In deze samenvatting beschrijf ik in grote lijnen de resultaten en significantie van dit onderzoek. Ik begin met een inleiding die het ontstaan van sterren beschrijft.

Achtergrondinformatie

WIE OP EEN HELDERE, MAANLOZE NACHT naar de hemel kijkt, ziet een lichtgevende, witte band die zich uitstrekt van horizon tot horizon. Het licht dat we zien is afkomstig van miljoenen sterren die deel uitmaken van de Melkweg, het sterrenstelsel waar ook wij ons in bevinden. De ruimte tussen de sterren in de Melkweg is enorm en alles wat zich in deze ruimte bevindt, wordt de interstellaire materie genoemd. Deze materie bestaat voor het grootste deel uit een zeer ijl gas, voornamelijk opgemaakt uit waterstof en helium, en voor ongeveer 1% (in massa) uit interstellair stof. De gemiddelde dichtheid van de interstellaire materie is ongeveer één atoom per kubieke centimeter (cm^{-3}). Ter vergelijking: de lucht die wij op aarde inademen heeft een dichtheid in de orde van 10 000 000 000 000 000 000 moleculen cm^{-3}. De temperatuur van het gas varieert van zo'n -265° C tot een miljoen graden Celsius. Een klein deel van het gas manifesteert zich in discrete wolken van ongeveer één tot honderden lichtjaren groot (1 lichtjaar is ongeveer 10 biljoen kilometer). Dit gas heeft een zeer lage temperatuur (-265° C) en bestaat voor het grootste deel uit moleculen. Deze zogeheten moleculaire wolken hebben een, wat de interstellaire ruimte betreft, hoge dichtheid (200 moleculen cm^{-3}) en vormen de geboorteplaatsen van sterren in de Melkweg.

Zelfs met het blote oog zijn enkele dichtbij gelegen moleculaire wolken zichtbaar als een donker silhouet tegen de heldere achtergrond van de Melkweg. Deze donkere gebieden aan de hemel werden in 1785 door Sir William Herschel (1738–1822)

beschreven als *gaten* in de hemel. Pas aan het begin van de 20ste eeuw ontdekte Edward E. Barnard (1857–1923) in een serie fotografische opnames dat deze objecten in werkelijkheid het licht van verder weg gelegen sterren tegenhouden. Halverwege de 20ste eeuw realiseerden astronomen zich dat donkere wolken samenhangen met stervormingsgebieden. Bart J. Bok (1906–1983) beweerde naar aanleiding van deze ontdekking dat donkere wolken, later ook wel *Bok globules* genoemd, objecten zijn waaruit sterren ontstaan. Opmerkelijk genoeg werd het idee dat sterren ontstaan uit ineenstortende wolken al in 1734 op filosofische gronden voorgesteld door Emanuel Swedenborg (1688–1772) en vervolgens in 1755 verder uitgewerkt door Immanuel Kant (1724–1804).

De hiërarchische structuur van moleculaire wolken

Het moleculaire stadium van de interstellaire materie bestaat uit een hiërarchische structuur van moleculaire wolken. De grootste wolken zijn de zogeheten *Reuze Moleculaire Wolken* (bijvoorbeeld de Orion moleculaire wolk) met afmetingen tot soms wel enkele honderden lichtjaren. Een aantal van de kleinere moleculaire wolken, hooguit enkele tientallen lichtjaren groot, staat relatief dicht bij de Zon. Deze worden waargenomen als *donkere wolken* tegen de heldere achtergrond van sterren. Een voorbeeld van een donkere wolk is de Ophiuchus moleculaire wolk. Daarnaast kennen we ook nog de *donkere globules*. Dit zijn kleine (~ 1 lichtjaar), geïsoleerde moleculaire wolken, die oorspronkelijk waarschijnlijk deel uitmaakten van grotere wolken.

Op kleinere schaal (van ongeveer één tot enkele tientallen lichtjaren groot) vinden we binnenin moleculaire wolken een substructuur van filamenten waarvan de deeltjesdichtheid tot wel 100 keer groter is. Deze filamenten bestaan op hun beurt weer uit nog kleinere objecten, de zogeheten *proto-stellaire* en *proto-cluster* wolken, waarvan de deeltjesdichtheid nog een factor 10 tot 100 groter is.

Van moleculaire wolk tot ster

Een ster ontstaat wanneer een proto-stellaire wolk ineenstort als gevolg van zijn eigen zwaartekracht. In de sterrenkunde wordt onderscheid gemaakt tussen de vorming van *lage-massa* sterren en *hoge-massa* sterren. Het is gebruikelijk om de massa van sterren uit te drukken in zonsmassa's ($M_\odot$), waarbij $1\,M_\odot$ gelijk is aan 2×10^{30} kg. Sterren met een massa die ongeveer gelijk is aan die van de Zon of minder, worden lage-massa sterren genoemd. Hoge-massa sterren hebben een massa groter dan $8\,M_\odot$. Wanneer een ster een massa heeft tussen de $1\,M_\odot$ en $8\,M_\odot$ behoort zij tot de middenklasse. Voor zover bekend ontstaan hoge-massa sterren vrijwel altijd in groepen: de zogenaamde *sterclusters*. Hierin ontstaan ook veel lage-massa sterren. De vorming van een stercluster in een proto-cluster wolk wordt nog niet goed begrepen, mede omdat er nog onvoldoende astronomische waarnemingen van de vroege stadia van sterclusterformatie zijn gedaan. Dit proefschrift draagt bij aan de ontwikkelingen op dit gebied. Na een korte beschrijving van het geïsoleerde stervormingsproces waarbij een lage-massa ster ontstaat, zal ik verder ingaan op de vorming van sterclusters.

Het ontstaan van geïsoleerde lage-massa sterren

Geïsoleerde lage-massa sterren ontstaan uit een proto-stellaire wolk, waarbij het ontstaansproces op geen enkele manier van buitenaf beïnvloed wordt. In het begin van het ontstaansproces zorgen draaiing, interne bewegingen en magneetvelden in de wolk ervoor dat het gas en stof slechts langzaam door de zwaartekracht naar het centrum worden getrokken. Op een gegeven moment wordt de dichtheid van gas en stof in het centrum echter zo groot, dat de zwaartekracht overwint en de kern ineenstort. In het centrum vormt zich een proto-ster. De draaiing die aanwezig is in de wolk versnelt door de ineenstorting. Daardoor wordt het overgebleven gas en stof niet direct naar het centrum getrokken, maar vormt zich als een schijf om de proto-ster. Langs de polen van de draaias wordt gas en stof weggeblazen door de sterrenwind. De temperatuur in de proto-ster stijgt tot ongeveer 10 miljoen graden. Vanaf dat moment zijn de dichtheid en temperatuur hoog genoeg om waterstofatomen te fuseren tot helium en spreken we van een *main sequence* ster, oftewel een ster. De omliggende wolk van gas en stof is nagenoeg verdwenen en het is mogelijk dat er planeten in de schijf zijn ontstaan.

Het ontstaan van hoge-massa sterren en sterclusters

Hoge-massa sterren ontstaan in sterclusters. Het ontstaansproces van hoge-massa sterren is veel minder goed bestudeerd dan dat van lage-massa sterren. Hiervoor zijn verschillende redenen. Allereerst ontstaan hoge-massa sterren in clusters. Vanzelfsprekend ligt de oorsprong van sterclusters in moleculaire wolken die voldoende gas en stof bevatten om veel sterren te vormen. De aanwezigheid van zoveel gas en stof maakt het zeer moeilijk om de vroege stadia van hoge-massa stervorming te kunnen waarnemen. Het zicht erop is simpelweg geblokkeerd. In de tweede plaats komen hoge-massa sterren veel minder vaak voor dan lage-massa sterren. Doordat ze zo zeldzaam zijn staan de meeste hoge-massa sterren ver van ons verwijderd en zijn dus moeilijk te bestuderen. Een derde reden is, dat het ontstaan van hoge-massa sterren slechts enkele miljoenen jaren duurt. Dit is een factor 10 korter dan de duur van het lage-massa-stervormingsproces.

We weten op dit moment nog niet goed hoe hoge-massa sterren ontstaan. Mogelijk is het proces vergelijkbaar met het ontstaansproces van lage-massa sterren. Een hoge-massa ster vormt zich echter zo snel, dat de sterrenwind al in een vroeg stadium de omliggende wolk van gas en stof van zich af stoot. Berekeningen laten zien dat er op dat moment een ster van hooguit ongeveer $10 M_{\odot}$ kan zijn ontstaan. Hogere massa sterren kunnen dus onmogelijk volgens precies hetzelfde scenario ontstaan.

Al met al is er op dit moment nog geen sluitende theorie over het ontstaan van hoge-massa sterren. Meerdere scenario's zijn voorgesteld, maar geen daarvan is compleet. Een belangrijke stap voorwaarts zal zijn wanneer we in veel verschillende gebieden van de Melkweg de zeer jonge stadia van sterclustervorming in detail kunnen waarnemen.

Infrarode donkere wolken

Halverwege de jaren '90 van de vorige eeuw werd er een belangrijke ontdekking gedaan met behulp van twee satellieten, *MSX* (*Midcourse Space Experiment*) en *ISO* (*Infrared Space Observatory*), die de hemel observeerden in infrarode straling. Tegen een achtergrond van heldere, diffuse infraroodstraling, afkomstig van zeer kleine stofdeeltjes in de Melkweg, detecteerden zij vele duizenden donkere objecten. Gedetailleerde studies hebben aangetoond dat deze objecten ver weg gelegen moleculaire wolken zijn ($\gtrsim 3000$ lichtjaar). In deze wolken is zóveel gas en stof aanwezig, dat zelfs infrarode straling er niet of nauwelijks doorheen schijnt. Ze kregen dan ook de naam *infrarode donkere wolken*. De massa van deze wolken varieert tussen de 500 en 10 000 $M_\odot$, terwijl de deeltjesdichtheid vergelijkbaar is met die van proto-stellaire wolken ($> 10\,000$ deeltjes cm^{-3}). Inmiddels weten we vrijwel zeker dat deze wolken de langgezochte, zeer vroege stadia van sterclustervorming zijn. Vanwege de grote afstand tot de wolken is het tot nu toe nog niet mogelijk om in te zoomen op individuele proto-stellaire wolken.

De buitenste delen van de Melkweg

Infrarode donkere wolken zijn met *MSX* en *ISO* alleen waargenomen in de richting van het centrum van de Melkweg. Het doel van dit proefschrift is om soortgelijke donkere wolken te vinden in de *buitenste* Melkweg. Deze buitenste delen bevinden zich op een afstand van meer dan 28 000 lichtjaar van het centrum van de Melkweg. Met andere woorden, de buitenste Melkweg bevindt zich buiten de baan die de Zon aflegt om het centrum. In deze buitenste delen konden infrarode donkere wolken tot dusver niet worden waargenomen vanwege een te zwakke infrarode achtergrond. Er bevindt zich namelijk veel minder gas en stof in deze gebieden. We vermoeden echter wel, dat de zeer vroege stadia van sterclustervorming aanwezig zijn in dit gebied.

De buitenste gebieden van de Melkweg zijn zeer interessant om stervormingsgebieden in te bestuderen. Dit is namelijk een relatief nabij gelegen gebied ten opzichte van de Zon waar de begincondities voor het ontstaan van sterren toch anders zijn dan die van de binnenste delen van de Melkweg. Denk hierbij bijvoorbeeld aan de hoeveelheid zware elementen in de interstellaire materie of aan de sterkte van het elektromagnetische stralingsveld afkomstig van sterren (waaronder zichtbaar licht en infraroodstraling). Het is van groot belang om de invloed van deze begincondities op het stervormingsproces te begrijpen. Dit zal uiteindelijk leiden tot een beter inzicht in stervorming in onze Melkweg, andere melkwegstelsels en in het vroege Universum.

Dit proefschrift

Drie belangrijke vragen vormen de basis voor dit proefschrift.

1) Bestaan infrarode donkere wolken ook in de buitenste delen van de Melkweg?

2) Kunnen we met bestaande telescoopwaarnemingen die we tot onze beschikking hebben deze vroege stadia van sterclustercvorming lokaliseren?

3) Wat zijn de begincondities in gebieden van sterclustercvorming in de buitenste delen van de Melkweg?

In dit proefschrift presenteren we een statistische methode waarmee we donkere wolken kunnen vinden. De methode maakt gebruik van het feit dat een moleculaire wolk de kleur van achtergrondsterren aanzienlijk roder maakt. Dit komt doordat de aanwezige stofdeeltjes in een wolk meer straling absorberen met een korte golflengte (te vergelijken met blauw licht) dan met een lange golflengte (te vergelijken met rood licht). De sterkleuren die we onderzoeken met de methode zijn afkomstig van de *Two Micron All Sky Survey* (*2MASS*). Dit is een project waarbij de hele hemel is waargenomen in het nabij-infrarood (straling met een golflengte van ongeveer 1 tot 5 micrometer).

Met behulp van deze methode hebben we een catalogus kunnen samenstellen waar meer dan 1000 objecten in staan. Deze objecten hebben een significant rodere verdeling van sterkleuren vergeleken met de directe omgeving. Een vervolganalyse van de objecten verschaft informatie over o.a. de afstand tot deze objecten, de associatie van objecten met reeds bekende donkere wolken en de associatie met mid-infrarode (golflengte van 5 tot 50 micrometer) en ver-infrarode (golflengte van 50 tot 300 micrometer) objecten (waargenomen met *MSX* en *IRAS*, de *Infrared Astronomical Satellite*). Deze mid- en ver-infrarode emissie kan een aanwijzing zijn voor de aanwezigheid van stervorming, omdat zéér jonge sterren sterk stralen in dit golflengtegebied. Op basis van deze analyse hebben we meerdere kandidaten geselecteerd. We presenteren de resultaten van kandidaat G111.80+0.58. Dit object is de eerste geïdentificeerde infrarode donkere wolk in de buitenste delen van de Melkweg. Hieronder geef ik een korte beschrijving van de verschillende hoofdstukken in dit proefschrift, waarbij ik voor de hoofdstukken 3 tot en met 6 met name de belangrijkste conclusies zijn samenvat.

- *Hoofdstuk 1*
  In dit hoofdstuk staat een overzicht van verschillende aspecten gerelateerd aan stervorming. Na een introductie over de interstellaire materie, met name gericht op de moleculaire fase, worden verschillende tijdsschalen besproken die van belang zijn voor het proces van stervorming. Daarna volgt een overzicht van het ontstaansproces van zowel lage-massa sterren als hoge-massa sterren. Aan het eind worden enkele methoden besproken waarmee we de vroegste stadia van stervorming kunnen waarnemen.

- *Hoofdstuk 2*
  Dit hoofdstuk geeft een overzicht van de huidige kennis op het gebied van infrarode donkere wolken. De globale eigenschappen van deze objecten, die uit recent onderzoek naar voren zijn gekomen, worden gepresenteerd. De belangrijkste conclusies van dit onderzoek zijn dat infrarode donkere wolken de vroege stadia van sterclusterformatie representeren en dat veel van deze wolken al een bepaalde mate van stervormingsactiviteit vertonen.

- *Hoofdstuk 3*
  We gebruiken de non-parametrische *Mann-Whitney U-test* om de statistische afwijkingen van sterkleuren te onderzoeken. Het voordeel van deze test is, dat het een kleurverdeling van slechts vijf sterren kan vergelijken met die van tienduizenden sterren. Dit betekent dat we een hoog ruimtelijk oplossingsvermogen kunnen realiseren. Daar komt bij dat we de methode uniform kunnen toepassen in elke willekeurige richting. Met een nauwkeurigheid van meer dan 99% vinden we meer dan 1000 extreem rode objecten in de buitengebieden van de Melkweg. Eenderde van deze objecten is al eerder waargenomen als donkere wolk in visueel licht. Bij de helft van de objecten vinden we één of meerdere mid-infrarode objecten. Ongeveer 400 objecten zijn, uitgaande van de analyse gepresenteerd in dit hoofdstuk, van onbekende origine.

- *Hoofdstuk 4*
  We onderzoeken de aanwezigheid van moleculair gas in de richting van de objecten uit de catalogus met behulp van waarnemingen van koolstofmonoxide (het molecuul CO). Wanneer er CO aanwezig is langs de gezichtslijn, straalt het emissie uit op een golflengte die gerelateerd is aan de afstand die het van ons verwijderd is. Meer dan 90% van de objecten is op deze manier gerelateerd aan straling afkomstig van moleculaire wolken. Enkele honderden objecten komen overeen met CO emissie afkomstig van nabijgelegen moleculaire wolken, waarvan de meerderheid ook is waargenomen in visueel licht. Ongeveer 100 objecten zijn geassocieerd met ver weg gelegen moleculaire wolken. Tweederde van deze objecten is niet geïdentificeerd in visueel licht.
  Voor de objecten die waargenomen zijn in CO emissie vinden we een correlatie tussen de sterkte van de CO straling en de aanwezigheid van mid-infrarode objecten. Een sterkere CO emissie kan betekenen dat er gas aanwezig is met een relatief hogere temperatuur. We zien dat sterke CO emissie vaak samengaat met de aanwezigheid van mid-infrarode objecten. Dit versterkt de suggestie dat er een bepaalde mate van stervormingsactiviteit aanwezig is in deze objecten.

- *Hoofdstuk 5*
  Het eerste object dat we geselecteerd hebben als kandidaat voor een massieve donkere wolk is G111.80+0.58. Met behulp van waarnemingen van verschillende moleculen bepalen we de fysische eigenschappen van dit object. De conclusie is, dat het hier gaat om een moleculaire wolk met eigenschappen als structuur, massa, temperatuur, dichtheid en energie, die sterk overeenkomen met de eigenschappen die worden waargenomen in infrarode donkere wolken in de binnenste delen van de Melkweg. We vinden wederom meerdere aanwijzingen die duiden op de aanwezigheid van zeer jonge stadia van stervorming in deze wolk.

- *Hoofdstuk 6*
  Met zeer gevoelige waarnemingen in het mid-infrarood, afkomstig van de Spitzer ruimtetelescoop, tonen we aan dat object G111.80+0.58 inderdaad een

echte infrarode donkere wolk is. Deze telescoop kan zelfs het zeer zwakke mid-infrarode licht in de buitenste delen van de Melkweg waarnemen, waardoor G111.80+0.58 in absorptie is waar te nemen. Een analyse van de verschillende golflengten waarop is waargenomen toont aan, dat er in sommige delen van de wolk waarschijnlijk hele clusters van sterren vormen. Andere delen van de wolk vertonen geen enkele aanwezigheid van stervormingsactiviteit. Dit bevestigt onze vermoedens dat deze wolk zich inderdaad in een zeer vroeg stadium van stervorming bevindt.

De resultaten in Hoofdstukken 5 en 6 bewijzen dat de identificatiemethode die in Hoofdstukken 3 en 4 beschreven staat, werkt. Twee belangrijke vragen in dit proefschrift zijn dan ook beantwoord. Ja, infrarode donkere wolken bestaan in de buitenste delen van de Melkweg en ja, we kunnen ze vinden!

De toekomst

We hebben in dit proefschrift laten zien dat het met de data die beschikbaar zijn mogelijk is om de zeer jonge stadia van sterclustervorming te vinden in de buitenste delen van de Melkweg. We realiseren ons hierbij wel, dat het identificeren van objecten een tijdrovende zaak is. Voornamelijk als aanvulling op toekomstige waarnemingen zal de catalogus efficiënt gebruikt kunnen worden. Voorbeelden hiervan zijn inmiddels gestarte projecten met het SCUBA2 instrument op de James Clerk Maxwell telescoop op Hawaii. Deze zullen de ruimtelijke verdeling en kolomdichtheid van koud stof in grote delen van de Melkweg in kaart brengen. De verwachting is dat er vele zware donkere wolken zullen worden waargenomen. Deze stofwaarnemingen op zich zijn echter niet voldoende om objecten te classificeren als donkere wolken. De catalogus die we gepresenteerd hebben in dit proefschrift kan hierbij mogelijk gebruikt worden om verschillende objecten van elkaar te onderscheiden.

Een nieuwe generatie telescopen zal in de nabije toekomst waarnemingen in het infrarood- en radio-golflengte gebied kunnen doen die veel gedetailleerder zijn dan tot nu toe mogelijk was. Met name instrumenten aan boord van de Herschel ruimtetelescoop (HIFI, PACS en SPIRE) en de Atacama Large Millimeter/sub-millimeter Array (ALMA) zullen aanzienlijk bijdragen aan de kennis op het gebied van stervorming. HIFI heeft de mogelijkheid om duizenden spectrale lijnen op zeer hoge spectrale resolutie waar te nemen. Dit biedt de unieke mogelijkheid om de gas kinematica en fysische condities in stervormingsgebieden in detail te observeren. ALMA maakt het over een paar jaar mogelijk om hoge-massa stervorming waar te nemen met een ongekend oplossend vermogen in het betreffende golflengtegebied.

Dankwoord

Dit is dan het resultaat van vier jaar werken. Rest mij enkel nog het dankwoord. Dit proefschrift was nooit tot stand gekomen zonder de enthousiaste begeleiding van mijn twee promotoren; Russ en Marco. Ik heb genoten van de bijzondere samenwerking. Zowel de wetenschappelijke als sociale ontmoetingen waren zonder uitzondering een genoegen ... wordt vervolgd!

Verder wil ik een aantal mensen in het bijzonder bedanken.
David, die mij de beginselen van het waarnemen en de vele geneugten eromheen heeft bijgebracht. Het wordt tijd dat we weer eens door de sneeuw naar Effelsberg rijden. Xander, die mij de eerste jaren van de promotie op weg heeft geholpen.
Alle mensen die in de afgelopen 10 jaar op het Kapteyn Instituut hebben rondgezworven. In meer of mindere mate, en vaak zelfs onbewust, hebben ze bijgedragen aan de totstandkoming van dit proefschrift. Ditzelfde geldt voor vele mensen bij SRON. Het was een geweldige tijd. In het bijzonder bedank ik iedereen van het secretariaat en de computergroep, alle mensen van de ISM-groep Groningen en alle kamergenoten die het met mij hebben uitgehouden.
Hait, Sanne en Anne voor de taalkundige ondersteuning.
Christiaan, mijn redder in nood wanneer de Mac en ik niet op één lijn zaten. Jack ... dat spreekt voor zich natuurlijk. Kambiz en Dieter, de 'Zes bier graag!' blijft onovertroffen. Ton, Gerard en Douwe die de afgelopen jaren voor Dieter en mij voor de hoognodige snookerafleiding hebben gezorgd. Plezier! Mijn lieve 'buren' in Zuidhorn. Ruth, Mirjam, Luuk en Anne-Gosse, omdat ze vooral in de laatste maanden een tweede huis boden voor Julian wanneer ik aan het werk was. Natuurlijk ook omdat ze zo hebben bijgedragen aan het feit dat we ons thuis voelen in Zuidhorn.
Hait en ma, die me al 32 jaar steunen. Anne en Martin die daar alweer bijna 5 jaar aan meedoen. Natuurlijk ook alle vrienden, familie en collega's die ik niet bij naam genoemd heb.

En als laatste Sanne, Julian en zijn broertje of zusje, mien grootste laiverds.

Bedankt allemaal!

Wilfred Frieswijk, Zuidhorn, 20 februari 2008

Thus ends the fifth battle

By the treachery of men the field is lost

The night falls and great is the triumph of evil

The league is broken

The last vestige of hope lives in the hidden king

Only he troubles the dark one's mind

Only he could bring ruin to the black foe

Though the land lies down in agony and the curse lives on

A new star shall arise

And a new day shall come, again

Final Chapter (Thus Ends...)

from "*Nightfall in Middle Earth*" by Blind Guardian
Based on "*The Silmarillion*" by J. R. R. Tolkien